IODP INTERNATIONAL OCEAN DISCOVERY PROGRAM

Check for updates

Contents

Site U1540[1]

G. Winckler, F. Lamy, C.A. Alvarez Zarikian, H.W. Arz, C. Basak, A. Brombacher, O.M. Esper, J.R. Farmer, J. Gottschalk, L.C. Herbert, S. Iwasaki, V.J. Lawson, L. Lembke-Jene, L. Lo, E. Malinverno, E. Michel, J.L. Middleton, S. Moretti, C.M. Moy, A.C. Ravelo, C.R. Riesselman, M. Saavedra-Pellitero, I. Seo, R.K. Singh, R.A. Smith, A.L. Souza, J.S. Stoner, I.M. Venancio, S. Wan, X. Zhao, and N. Foucher McColl[2]

Background and objectives

Site U1540 is located in the central South Pacific at 55°08.467′S, 114°50.515′W, ~1600 nmi west of the Strait of Magellan at 3580 m water depth (Figure F1). The site sits at the eastern flank of the southernmost East Pacific Rise (EPR) within the Eltanin Fracture Zone, ~130 nmi from the modern seafloor spreading axis, and is underlain by oceanic crust formed at the EPR ~6–8 My ago (Eagles, 2006). Assuming overall constant seafloor half-spreading rates of ~4.5 cm/y (Pitman and Heirtzler, 1966), the plate tectonic backtrack path of Site U1540 moves the site westward. This translates to an early Pliocene position ~100 nmi closer to the crest of the EPR at a water depth shallower by several hundred meters. At a smaller scale, the site is located at the northeast end of a ridge that parallels the orientation of the EPR. The site is located ~2 nmi northwest of site survey Core PS75/056-1 (Gersonde, 2011).

Site U1540 is crossed by a sediment echo sound (Parasound) profile oriented northwest–southeast (Gersonde, 2011). The profile documents excellent penetration (>150 m) and distinct layering (Figure F2), suggesting a succession of fine-grained soft sediments with varying lithologic composition.

A ~10 m long gravity core (PS75/056-1) covering the past ~250 ky close to Site U1540 contains an alternation of diatom ooze during glacial intervals (~20–40 wt% $CaCO_3$, ~40–55 wt% opal, and ~10–25 wt% siliciclastics) and diatomaceous calcareous ooze during interglacial intervals (~60–80 wt% $CaCO_3$, ~5–15 wt% opal, and ~5–10 wt% siliciclastics). Sedimentation rates vary between 3 and 6 cm/ky throughout the record.

Site U1540 lies in the pathway of the Subantarctic Antarctic Circumpolar Current (ACC), ~170 nmi north of the modern mean position of the Subantarctic Front (SAF) in a zonal transition zone of the ACC. West of the site, the ACC and associated fronts are strongly steered by the topography of seafloor spreading systems (Udintsev and Eltanin-Tharp Fracture Zone systems), whereas to the east, the vast Amundsen Sea Basin does not influence the position of the ACC strongly.

Sea-surface temperatures (SSTs) vary seasonally between ~2.5°C (July–September) and ~7°C (January–March). The area is located west of the main Antarctic Intermediate and Mode Water formation regions in the Southeast Pacific. The water depth of 3570 m places Site U1540 within Lower Circumpolar Deep Water (LCDW) (Figure F3).

Scientific objectives

The main objectives at Site U1540 are to

- Recover a moderate-resolution Subantarctic Pliocene–Quaternary sediment record close to the SAF;
- Investigate the sequencing of siliceous and calcareous oozes, allowing for a wide range of paleoceanographic reconstructions;
- Reconstruct high-amplitude subantarctic SSTs;
- Provide a record of LCDW and glacial Antarctic Bottom Water (AABW);
- Reconstruct productivity (e.g., opal, carbonate, and organic matter), nutrient distribution, and dust-productivity coupling; and
- Recover a potential far-field record of West Antarctic Ice Sheet variability.

Figure F1. Oceanographic and bathymetric setting, Site U1540. A. Marine geological features and oceanic fronts. EPR = East Pacific Rise. FZ = fracture zone, APF = Antarctic Polar Front (after Orsi et al., 1995), SAF = Subantarctic Front. B. Detailed bathymetry with seismic lines and shotpoints.
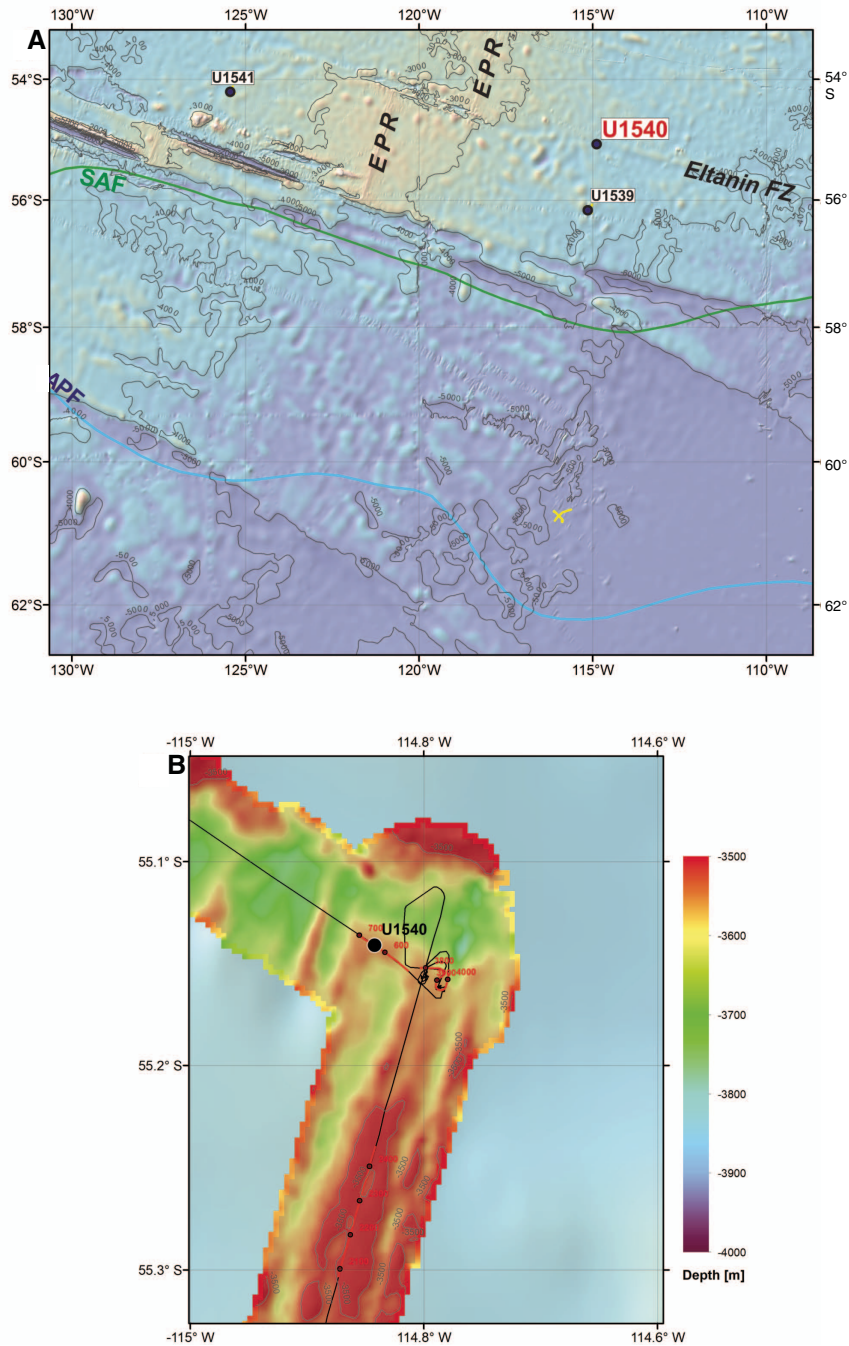
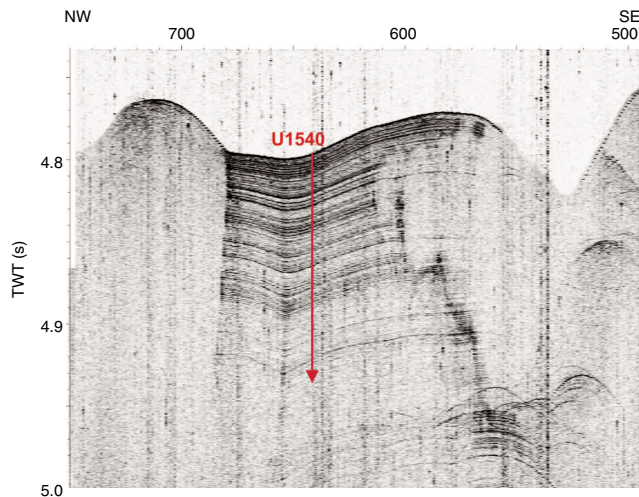Figure F2. Parasound profiles across Site U1540. TWT= two-way traveltime.

Figure F3. Modern salinity (contour lines) and oxygen distribution (colors) in the central South Pacific used to visualize major water masses. NPDW = North Pacific Deep Water, LCDW = Lower Circumpolar Deep Water, AABW = Antarctic Bottom Water. (Continued on next page.)
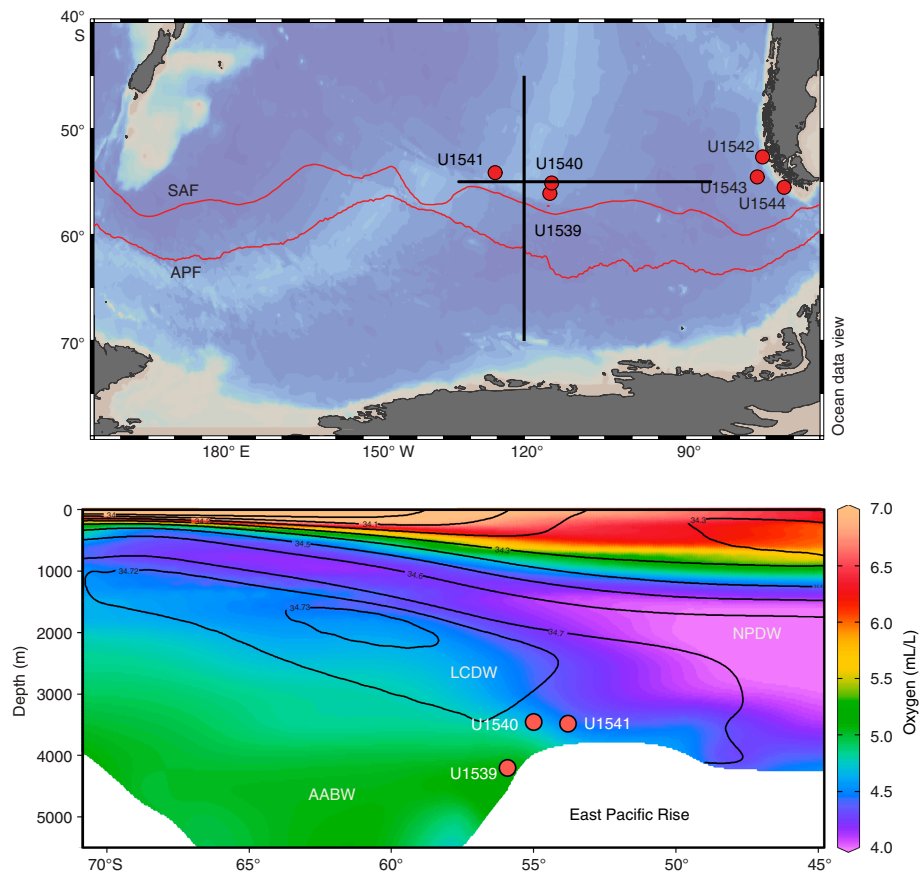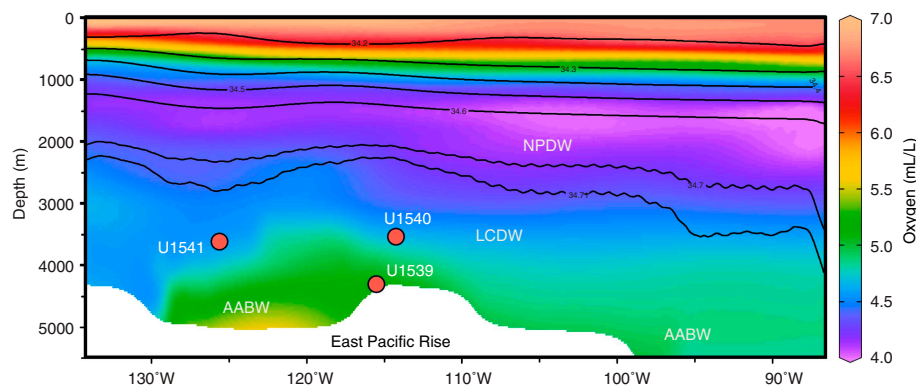
Figure F3 (continued).

Operations

Five holes were cored at Site U1540 using the advanced piston corer (APC) and extended core barrel (XCB) systems. Hole U1540A was cored to 150 m core depth below seafloor, Method A (CSF-A) (155.13 m recovered; 103.4%). Hole U1540B was cored to 150 m CSF-A, including three drilled intervals totaling 10 m (140.78 m recovered; 100.6%). Hole U1540C was cored to only 6.8 m CSF-A because the first core did not recover a good sediment–water interface (6.77 m recovered; 99.6%). Hole U1540D was cored to 211 m CSF-A, including four drilled intervals totaling 58.7 m (151.0 m recovered; 99.2%). Hole U1540E was cored to 213 m CSF-A, including two drilled intervals totaling 137 m (78.87 m recovered; 103.4%).

Transit to Site U1540

After recovering the drill string at Site U1539, the rig floor was secured for transit at 0130 h on 7 June 2019. The thrusters were raised, and the sea voyage to Site U1540 began at 0224 h. After a 61 nmi transit at an average speed of 10 kt, we arrived on site at 0830 h. The thrusters were lowered, and the vessel switched to dynamic positioning mode over the site coordinates at 0929 h on 7 June.

Site U1540

Hole U1540A

The crew made up an APC/XCB bottom-hole assembly, and the bit was lowered to 2171 meters below rig floor (mbrf) by 1645 h on 7 June 2019. The vessel began experiencing heave above 7.0 m with a roll of ~5° at that time, and it was decided to wait for the seas to calm before continuing operations. The seas calmed sufficiently by 0415 h on 8 June, and drill floor operations resumed. With an estimated seafloor depth of 3600.6 mbrf based on the calculation from the precision depth recorder, the bit was lowered to 3595.0 mbrf to spud Hole U1540A. Core 383-U1540A-1H recovered 9.0 m of sediment, and the seafloor was calculated at 3595.5 mbrf (3584.6 meters below sea level [mbsl]). The hole was cored to 150 m CSF-A by 0815 h on 9 June. The top drive was set back, and the bit was pulled to 3561 mbrf, clearing the seafloor at 0900 h on 9 June and ending Hole U1540A. A total of 16 cores were taken with the APC system with a recovery of 155.09 m (103%). Advanced piston corer temperature (APCT-3) tool formation temperature measurements were taken with Cores 4H, 7H, 10H, 13H, and 16H. Orientation measurements were taken on all cores. Misfires were recorded on Cores 1H, 7H, and 16H. A misfire on Core 7H caused a noisy temperature reading.

Hole U1540B

The vessel was offset 20 m east of Hole U1540A, and the bit was lowered to 3575 mbrf for spudding Hole U1540B. Our first attempt to take Core 383-U1540B-1H did not retrieve any sediment. The bit was then lowered 9.5 m to 3584.5 mbrf, and Hole U1540B was started at 1220 h on 9 June 2019. Based on the Core 1H recovery, the seafloor was calculated at 3580.0 mbsl. APC coring continued to 150 m CSF-A with three drilled intervals (totaling 10 m) to help obtain a good overlap with Hole U1540A cores. A total of 16 cores were taken over a 140.8 m interval with 101% recovery. Misfires were recorded on Cores 1H, 6H, 8H, and 11H. The bit was pulled back to the seafloor, ending Hole U1540B at 0958 h on 10 June.

After coring Hole U1540B, permission was requested from the International Ocean Discovery Program (IODP) Environmental Protection and Safety Panel to extend the penetration depth at Site U1540 from 150 to 275 m CSF-A. This request was based on the successful recovery of a complete and continuous Pleistocene sedimentary record in Holes U1540A and U1540B. The increase in penetration depth would allow us to extend this record into the Pliocene, which was expected directly below the already cored maximum depth of 150 m CSF-A. An additional rationale was the prevailing sea conditions on site, which predicted two additional days of reasonably calm seas, thus allowing for further drilling, whereas significantly worse sea conditions were forecast at our two other primary sites in the South Pacific.

Hole U1540C

Hole U1540C was spudded 20 m south of Hole U1540B at 1110 h on 10 June 2019 with the bit positioned at 3587.5 mbrf. Based on the visual inspection of the material recovered in Core 383-U1540C-1H, we determined that the mudline was missed, and the hole was ended at 1200 h.

Hole U1540D

The vessel was offset 20 m west of Hole U1540C, and the bit was spaced out to 3587.5 mbrf to start Hole U1540D. Core 383-U1540D-1H was taken at 1235 h on 10 June 2019 and recovered 8.92 m (100%). This allowed us to determine a water depth of 3577.5 mbsl. Permission to extend the penetration depth at Site U1540 to 275 m CSF-A was received while retrieving Core 11H from 79.2 m CSF-A. We drilled ahead without recovery to 131.0 m CSF-A before coring resumed. The full-length APC system was deployed, and the hole was deepened until we reached APC refusal at 210.5 m CSF-A. Cores 21H and 22H (207.0–210.5 m CSF-A) recov-

ered just 3.9 m of sediment, with numerous rock fragments. The XCB system was deployed for one core in an attempt to recover more of the presumed basement material. After coring for 45 min, the core barrel was pulled to the surface with only 0.5 m of advancement and no recovery, and the decision was made to terminate the hole. The bit cleared the seafloor at 1710 h on 11 June 2019, ending Hole U1540D. A total of 19 cores were taken over a 151.8 m interval with 151 m recovered (99%). Misfires were recorded on Cores 4H and 6H, and partial strokes were recorded on Cores 22H and 23X.

Hole U1540E

The vessel was offset another 20 m west of Hole U1540D, and the bit was spaced out for spudding using the seafloor depth determined in Hole U1540D. Hole U1540E was spudded at 1840 h on 11 June and drilled ahead to 135 m CSF-A. The hole was then cored using the full-length APC system and reached refusal at 213 m CSF-

A. The bit was recovered to the vessel, clearing the rotary table at 1900 h on 12 June. The rig was secured and readied for transit at 1905 h. A total of eight cores were taken from Hole U1540E with the APC system over a 76 m interval with 78.9 m recovered (104%). Core 383-U1540E-10H experienced a partial stroke. Two drilled intervals advanced a total of 137 m.

With the seas too high to raise the thrusters, we waited on weather until the seas calmed sufficiently at 1545 h on 13 June. The thrusters then were raised, and the vessel began the transit to Site U1541.

A total of 60 cores were taken at this site. The full-length APC system was deployed 59 times, and the XCB system was deployed one time. A total of 205.7 m was drilled ahead without recovery. The interval cored with the APC system was 525.1 m. Total core recovered is 532.6 m (101%). Total time spent at Site U1540 was 156 h (5.4 days). Coring summaries for Holes U1540A–U1540E are shown in Table T1.

Table T1. Core summary, Site U1540. DRF = drilling depth below rig floor, DSF = drilling depth below seafloor, CSF = core depth below seafloor. APC = advanced piston corer, HLAPC = half-length APC, XCB = extended core barrel, RCB = rotary core barrel. Core type: H = APC, F = HLAPC, numeric = drilled interval. (Continued on next two pages.) **Download table in CSV format.**

Hole: U1540A
  Latitude: 55°8.4674′S
  Longitude: 114°50.5188′W
  Water depth (m): 3584.6
  Date started (UTC, h): 7 Jun 2019 1215
  Date finished (UTC, h): 9 Jun 2019 1200
  Time on hole (days): 1.99
  Seafloor depth DRF (m): 3595.5
  Seafloor depth est. method: mudline core
  Rig floor to sea level (m): 10.9
  Penetration DSF (m): 150
  Cored interval (m): 150
  Recovered length (m): 155.13
  Recovery (%): 103.42
  Drilled interval (m):
  Drilled interval (*N*): 0
  Total cores (*N*): 16
  APC cores (*N*): 16

Hole: U1540B
  Latitude: 55°8.4656′S
  Longitude: 114°50.4985′W
  Water depth (m): 3579.98
  Date started (UTC, h): 9 Jun 2019 1200
  Date finished (UTC, h): 10 Jun 2019 1300
  Time on hole (days): 1.04
  Seafloor depth DRF (m): 3590.9
  Seafloor depth est. method: mudline core
  Rig floor to sea level (m): 10.92
  Penetration DSF (m): 150
  Cored interval (m): 140
  Recovered length (m): 140.78
  Recovery (%): 100.56
  Drilled interval (m): 10
  Drilled interval (*N*): 3
  Total cores (*N*): 16
  APC cores (*N*): 16

Hole: U1540C
  Latitude: 55°8.4474′S
  Longitude: 114°50.4994′W
  Water depth (m): 3579.26
  Date started (UTC, h): 10 Jun 2019 1300
  Date finished (UTC, h): 10 Jun 2019 1430
  Time on hole (days): 0.06
  Seafloor depth DRF (m): 3590.2
  Seafloor depth est. method: mudline core
  Rig floor to sea level (m): 10.94
  Penetration DSF (m): 6.8
  Cored interval (m): 6.8
  Recovered length (m): 6.77
  Recovery (%): 99.56
  Drilled interval (m):
  Drilled interval (*N*): 0
  Total cores (*N*): 1
  APC cores (*N*): 1

Hole: U1540D
  Latitude: 55°8.4766′S
  Longitude: 114°50.5196′W
  Water depth (m): 3577.16
  Date started (UTC, h): 10 Jun 2019 1430
  Date finished (UTC, h): 11 Jun 2019 2015
  Time on hole (days): 1.24
  Seafloor depth DRF (m): 3588.1
  Seafloor depth est. method: mudline core
  Rig floor to sea level (m): 10.94
  Penetration DSF (m): 211
  Cored interval (m): 152.3
  Recovered length (m): 151.02
  Recovery (%): 99.16
  Drilled interval (m): 58.7
  Drilled interval (*N*): 4
  Total cores (*N*): 19
  APC cores (*N*): 18
  XCB cores (*N*): 1

Table T1 (continued). (Continued on next page.)

Hole: U1540E
Latitude: 55°8.4772′S
Longitude: 114°50.5375′W
Water depth (m): 3577.16
Date started (UTC, h): 11 Jun 2019 2015
Date finished (UTC, h): 12 Jun 2019 2200
Time on hole (days): 1.07
Seafloor depth DRF (m): 3588.1
Seafloor depth est. method: offset
Rig floor to sea level (m): 10.94
Penetration DSF (m): 213
Cored interval (m): 76
Recovered length (m): 78.87
Recovery (%): 103.78
Drilled interval (m): 137
Drilled interval (*N*): 2
Total cores (*N*): 8
APC cores (*N*): 8

Core	Top depth drilled DSF (m)	Bottom depth drilled DSF (m)	Interval advanced (m)	Recovered length (m)	Curated length (m)	Top depth cored CSF-A (m)	Bottom depth recovered CSF-A (m)	Core recovery (%)	Time on deck UTC (h)	Sections (*N*)
383-U1540A-										
1H	0.0	9.0	9.0	8.93	8.93	0.0	8.93	99	8 Jun 2019 1225	7
2H	9.0	18.5	9.5	9.77	9.77	9.0	18.77	103	8 Jun 2019 1420	8
3H	18.5	28.0	9.5	10.11	10.11	18.5	28.61	106	8 Jun 2019 1545	8
4H	28.0	37.5	9.5	9.94	9.94	28.0	37.94	105	8 Jun 2019 1735	8
5H	37.5	47.0	9.5	9.88	9.88	37.5	47.38	104	8 Jun 2019 1855	8
6H	47.0	56.5	9.5	9.49	9.49	47.0	56.49	100	8 Jun 2019 2010	8
7H	56.5	64.8	8.3	8.30	8.30	56.5	64.80	100	8 Jun 2019 2130	7
8H	64.8	74.3	9.5	9.75	9.75	64.8	74.55	103	8 Jun 2019 2300	8
9H	74.3	83.8	9.5	9.69	9.69	74.3	83.99	102	9 Jun 2019 0035	8
10H	83.8	93.3	9.5	10.02	10.02	83.8	93.82	105	9 Jun 2019 0205	8
11H	93.3	102.8	9.5	9.72	9.72	93.3	103.02	102	9 Jun 2019 0325	8
12H	102.8	112.3	9.5	9.74	9.74	102.8	112.54	103	9 Jun 2019 0450	8
13H	112.3	121.8	9.5	9.58	9.58	112.3	121.88	101	9 Jun 2019 0620	8
14H	121.8	131.3	9.5	10.16	10.16	121.8	131.96	107	9 Jun 2019 0740	8
15H	131.3	140.8	9.5	9.83	9.83	131.3	141.13	103	9 Jun 2019 0855	8
16H	140.8	150.0	9.2	10.22	10.22	140.8	151.02	111	9 Jun 2019 1050	8
383-U1540B-										
1H	0.0	3.1	3.1	3.12	3.12	0.0	3.12	101	9 Jun 2019 1550	3
2H	3.1	12.6	9.5	9.88	9.88	3.1	12.98	104	9 Jun 2019 1720	8
3H	12.6	22.1	9.5	9.99	9.99	12.6	22.59	105	9 Jun 2019 1840	8
41	22.1	27.6	5.5			22.1	22.10		9 Jun 2019 1845	0
5H	27.6	37.1	9.5	9.77	9.77	27.6	37.37	103	9 Jun 2019 1950	8
6H	37.1	42.2	5.1	5.11	5.11	37.1	42.21	100	9 Jun 2019 2110	5
71	42.2	45.1	2.9			42.2	42.20		9 Jun 2019 2135	0
8H	45.1	53.4	8.3	8.39	8.39	45.1	53.49	101	9 Jun 2019 2215	7
91	53.4	55.0	1.6			53.4	53.40		9 Jun 2019 2255	0
10H	55.0	64.5	9.5	10.13	10.13	55.0	65.13	107	9 Jun 2019 2345	8
11H	64.5	74.0	9.5	9.67	9.67	64.5	74.17	102	10 Jun 2019 0100	8
12H	74.0	83.5	9.5	10.11	10.11	74.0	84.11	106	10 Jun 2019 0155	8
13H	83.5	93.0	9.5	8.33	8.33	83.5	91.83	88	10 Jun 2019 0305	7
14H	93.0	102.5	9.5	7.55	7.55	93.0	100.55	79	10 Jun 2019 0415	6
15H	102.5	112.0	9.5	9.32	9.32	102.5	111.82	98	10 Jun 2019 0520	7
16H	112.0	121.5	9.5	10.01	10.01	112.0	122.01	105	10 Jun 2019 0625	8
17H	121.5	131.0	9.5	9.83	9.83	121.5	131.33	103	10 Jun 2019 0725	8
18H	131.0	140.5	9.5	9.96	9.96	131.0	140.96	105	10 Jun 2019 0930	9
19H	140.5	150.0	9.5	9.61	9.61	140.5	150.11	101	10 Jun 2019 1035	8
383-U1540C-										
1H	0.0	6.8	6.8	6.77	6.77	0.0	6.77	100	10 Jun 2019 1435	6
383-U1540D-										
1H	0.0	8.9	8.9	8.92	8.92	0.0	8.92	100	10 Jun 2019 1605	7
2H	8.9	18.4	9.5	9.46	9.46	8.9	18.36	100	10 Jun 2019 1730	8
31	18.4	21.7	3.3	0.00	0.00	18.4	18.40		10 Jun 2019 1745	0
4H	21.7	28.1	6.4	6.43	6.43	21.7	28.13	100	10 Jun 2019 1830	6
51	28.1	29.7	1.6	0.00	0.00	28.1	28.10		10 Jun 2019 1850	0
6H	29.7	39.2	9.5	6.84	6.84	29.7	36.54	72	10 Jun 2019 1935	6
7H	39.2	48.7	9.5	9.24	9.24	39.2	48.44	97	10 Jun 2019 2055	8
8H	48.7	58.2	9.5	9.83	9.83	48.7	58.53	103	10 Jun 2019 2215	8
91	58.2	60.2	2.0	0.00	0.00	58.2	58.20		10 Jun 2019 2230	0

Table T1 (continued.)

Core	Top depth drilled DSF (m)	Bottom depth drilled DSF (m)	Interval advanced (m)	Recovered length (m)	Curated length (m)	Top depth cored CSF-A (m)	Bottom depth recovered CSF-A (m)	Core recovery (%)	Time on deck UTC (h)	Sections (N)
10H	60.2	69.7	9.5	9.79	9.79	60.2	69.99	103	10 Jun 2019 2330	8
11H	69.7	79.2	9.5	9.08	9.08	69.7	78.78	96	11 Jun 2019 0050	7
12I	79.2	131.0	51.8	0.00	0.00	79.2	79.20		11 Jun 2019 0355	0
13H	131.0	140.5	9.5	9.99	9.99	131.0	140.99	105	11 Jun 2019 0510	8
14H	140.5	150.0	9.5	9.30	9.30	140.5	149.80	98	11 Jun 2019 0615	8
15H	150.0	159.5	9.5	9.56	9.56	150.0	159.56	101	11 Jun 2019 0725	8
16H	159.5	169.0	9.5	9.74	9.74	159.5	169.24	103	11 Jun 2019 0830	8
17H	169.0	178.5	9.5	9.85	9.85	169.0	178.85	104	11 Jun 2019 0940	8
18H	178.5	188.0	9.5	9.85	9.85	178.5	188.35	104	11 Jun 2019 1045	8
19H	188.0	197.5	9.5	10.04	10.04	188.0	198.04	106	11 Jun 2019 1155	8
20H	197.5	207.0	9.5	9.21	9.21	197.5	206.71	97	11 Jun 2019 1305	8
21H	207.0	210.0	3.0	3.39	3.39	207.0	210.39	113	11 Jun 2019 1410	4
22H	210.0	210.5	0.5	0.50	0.50	210.0	210.50	100	11 Jun 2019 1610	1
23X	210.5	211.0	0.5	0.00	0.00	210.5	211.00	0	11 Jun 2019 1840	0
383-U1540E-										
1I	0.0	135.0	135.0	0.00	0.00	0.0	0.00		12 Jun 2019 0230	0
2H	135.0	144.5	9.5	9.92	9.92	135.0	144.92	104	12 Jun 2019 0335	8
3I	144.5	146.5	2.0	0.00	0.00	144.5	144.50		12 Jun 2019 0420	0
4H	146.5	156.0	9.5	9.89	9.89	146.5	156.39	104	12 Jun 2019 0505	8
5H	156.0	165.5	9.5	10.23	10.23	156.0	166.23	108	12 Jun 2019 0655	8
6H	165.5	175.0	9.5	9.39	9.39	165.5	174.89	99	12 Jun 2019 0805	8
7H	175.0	184.5	9.5	9.62	9.62	175.0	184.62	101	12 Jun 2019 0910	8
8H	184.5	194.0	9.5	9.92	9.92	184.5	194.42	104	12 Jun 2019 1025	8
9H	194.0	203.5	9.5	10.06	10.06	194.0	204.06	106	12 Jun 2019 1130	8
10H	203.5	213.0	9.5	9.84	9.84	203.5	213.34	104	12 Jun 2019 1230	8
		Totals:	730.80	532.57	532.57					439

Sedimentology

Site U1540 is located ~160 nmi north of the SAF at approximately 3580 m water depth and about 60 nmi north of Site U1539. Because of its position in the open-ocean Pacific sector of the Southern Ocean and its estimated basement age of younger than 10 Ma, Site U1540 sediments are well suited to investigate Pliocene–Pleistocene changes in the latitudinal position of Southern Ocean fronts, biological production, ocean circulation dynamics, and the supply of terrigenous material through winds and icebergs.

A composite 227.13 m long sedimentary sequence that spans the Pleistocene and a portion of the Pliocene was developed from Holes U1540A, U1540B, U1540D, and U1540E (see **Stratigraphic correlation**). Weather conditions at Site U1540 were generally favorable and allowed uninterrupted drilling operations (see **Operations**). Occurrences of fall-in (in the uppermost sections) and suck-in (in lower sections of the core) drilling disturbance were identified (see **Sedimentology** in the Expedition 383 methods chapter [Winckler et al., 2021a]) and classified as mixed biogenic oozes in the visual core descriptions (VCDs) and hole summaries (Figure **F4**) to avoid inclusion in the splice.

The Site U1540 sedimentary sequence is divided into two lithostratigraphic units based on the relative proportion of calcareous oozes, biosiliceous oozes, and clay as well as the frequency and overall distribution with which these lithologies occur (Figure **F4**). Site U1540 sediments form a compositional continuum between diatomaceous and calcareous oozes and include Lithofacies 1, 3, and 4, identified at Site U1539, and an additional clay component from two different sources (Figure **F5**) (see **X-ray diffraction clay mineralogy**). The clay component appears in the lower part of the sedimentary sequence and is a key characteristic that defines Lithofacies 6 and 7, which are distinct from Lithofacies 1–5 in their lithology, sedimentary structure, color, and composition.

Lithofacies description

Five lithofacies were identified at Site U1540 (Table **T2**). The numbering of the facies is based on all facies documented during Expedition 383 (see Table **T2** in the Expedition 383 summary chapter [Winckler et al., 2021b]), but only lithofacies documented at Site U1540 are described and discussed here. Two new lithofacies (6 and 7) were introduced at this site. All lithofacies defined at Site U1540 can be represented in a ternary diagram with diatom ooze, nannofossil ooze, and clay as end-members (Figure **F5**). Site U1540 sediments mainly differ in their relative proportions of calcareous and biosiliceous components, which vary between Lithofacies 2 (carbonate-bearing/rich diatom ooze; 55% of the recovered sequence), Lithofacies 3 (diatom-bearing/rich nannofossil/calcareous ooze; 22%), Lithofacies 4 (calcareous/nannofossil ooze; 11%), and Lithofacies 6 (clay-bearing/rich biogenic ooze; 12%). Lithofacies 7 occurs exclusively in the lower part of the sedimentary sequence in Holes U1540D and U1540E and consists of yellowish brown to dark reddish brown colored carbonate- and/or biosilica-bearing clay rich in Fe (hydr)oxides.

Lithofacies 2

Lithofacies 2 is light greenish gray (10Y 7/1) to gray (2.5Y 5/1) carbonate-bearing to carbonate-rich diatom ooze that exhibits moderate to heavy bioturbation (see **Bioturbation**) and may show wavy and/or discontinuous centimeter-scale bedding. The minor component (10%–49%) consists of nannofossils, foraminifers, and calcareous debris of mostly foraminiferal tests. Accessory components (<10%) include radiolarians, silicoflagellates, and sponge spicules. Dropstones >0.5 cm, which were identified through macroscopic visual inspection and X-ray images, are relatively frequent in this lithofacies. Sporadic diatom mats are also part of this lithofacies. Distinct color mottling in transitions to Lithofacies 3

Figure F4. Hole summaries, Site U1540. The placement of Pliocene and early Pleistocene stage boundaries in Holes U1540D and U1540E are estimated using the preliminary Site U1540 shipboard age model. GRA = gamma ray attenuation, MSP = point magnetic susceptibility, RGB = red, green, blue, NGR = natural gamma radiation, cps = counts per second. (Continued on next four pages.)
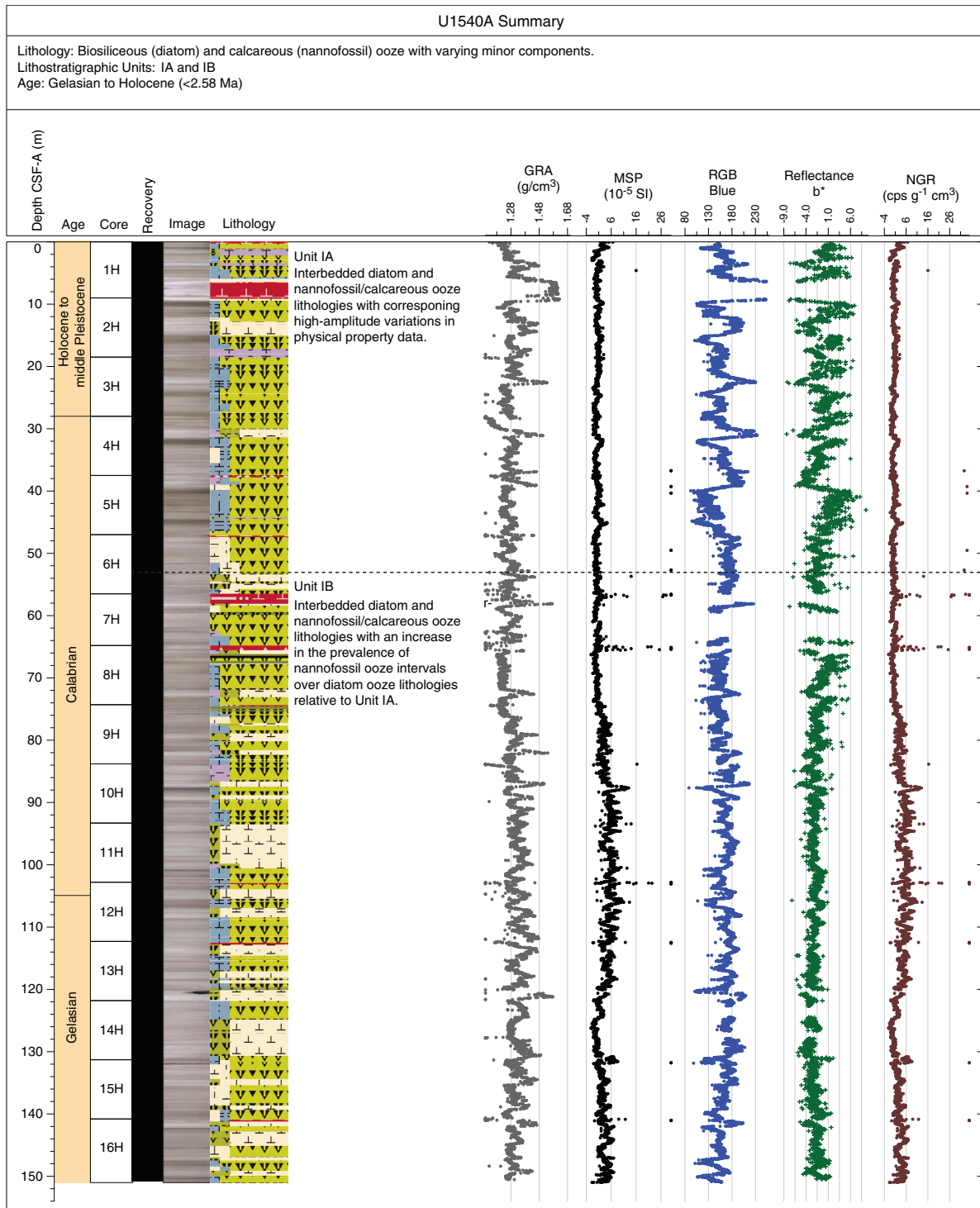
and 4 and associated density patterns in X-ray images reveal thin and elongated centimeter-scale burrows in this lithofacies. Lithofacies 2 is observed as extensive, regularly occurring beds of 0.2 to 1.5 m thickness throughout the sedimentary sequence at Site U1540. Examples of this lithofacies are found in Sections 383-U1540A-5H-7, 383-U1540B-17H-1, and 383-U1540D-16H-6.

Lithofacies 3

Lithofacies 3 is diatom-bearing to diatom-rich nannofossil or calcareous ooze. This lithofacies is characterized by white (N 9/), light gray (N 8/), or greenish gray (5Y 7/1) nannofossil and/or calcareous ooze, which often has a massive appearance and can show weak wavy centimeter-scale bedding. It is sometimes mottled with

Figure F4 (continued). (Continued on next page.)
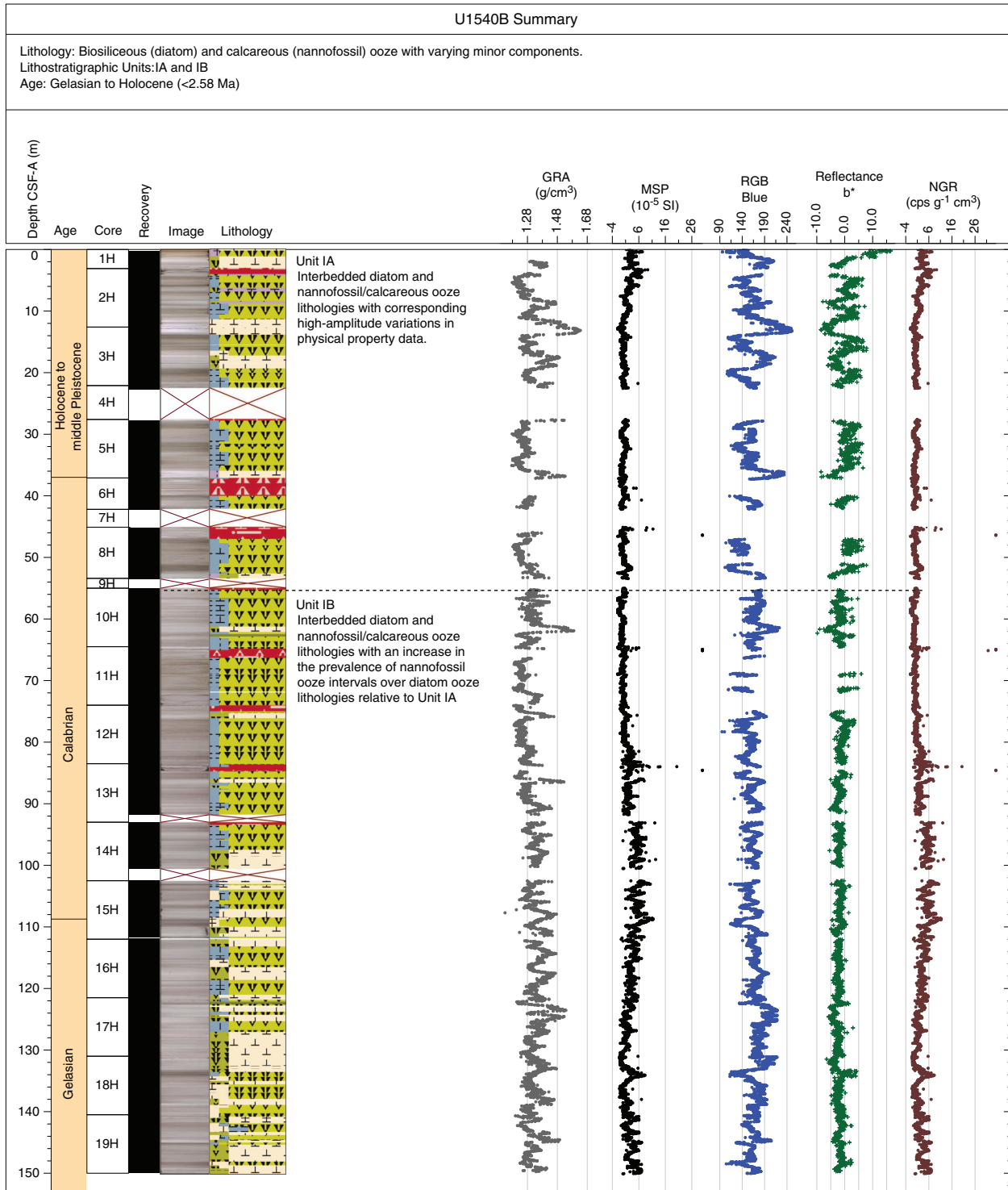
darker grayish greenish colors due to diagenetic iron sulfide over-prints. Lithofacies 3 is moderately to heavily bioturbated (see **Bioturbation**). Examination of smear slides indicates a varying degree of minor and major modifiers, mainly comprised of diatoms. X-ray images of this lithofacies reveal only minor abundances of dropstones, as well as some indications of thin and elongated centimeter-scale burrows, which are sometimes filled with iron sulfides. Along with foraminifers, radiolarians, and silicoflagellates, Lithofacies 3 also includes undifferentiated calcareous debris as an accessory component (<10%), most likely fragmented foraminiferal tests. Nannofossil and calcareous oozes are a subordinate lithology in the upper ~60 m and are more dominant between ~60 and 200 m CSF-A. Lithofacies 3 occurs as beds of 0.1 to 1.7 m thickness. Examples of this lithofacies are found in Sections 383-U1540A-10H-2, 383-U1540B-16H-4, and 383-U1540D-2H-4 and 16H-5.

Figure F4 (continued). (Continued on next page.)

U1540C Summary

Lithology: Biosiliceous (diatom) and calcareous (nannofossil) ooze with varying minor components
Lithostratigraphic Units: IA
Age: middle Pleistocene to Holocene (<0.98 Ma)

Unit IA
Interbedded diatom and nannofossil/calcareous ooze lithologies with corresponding high-amplitude variations in physical property data.
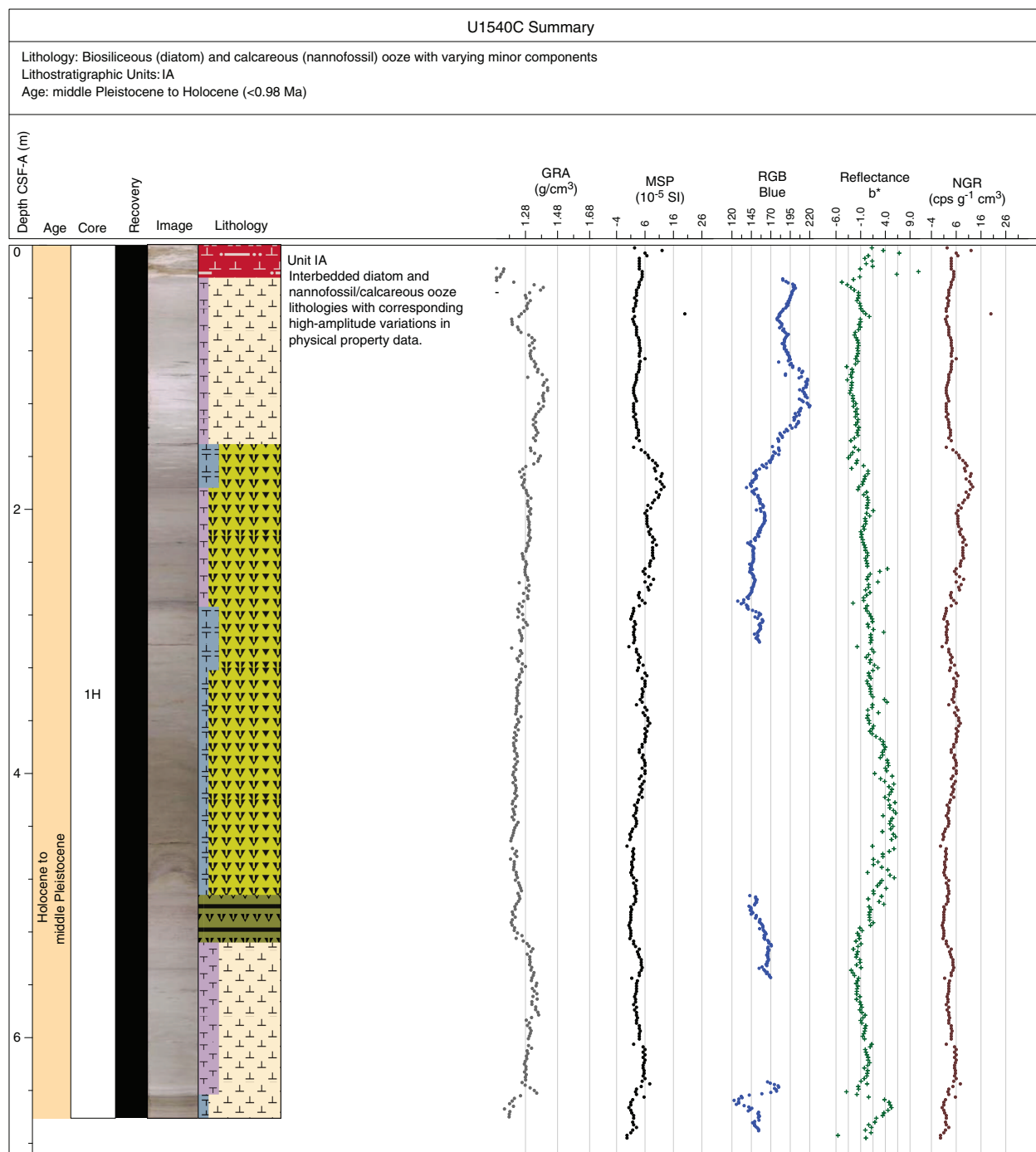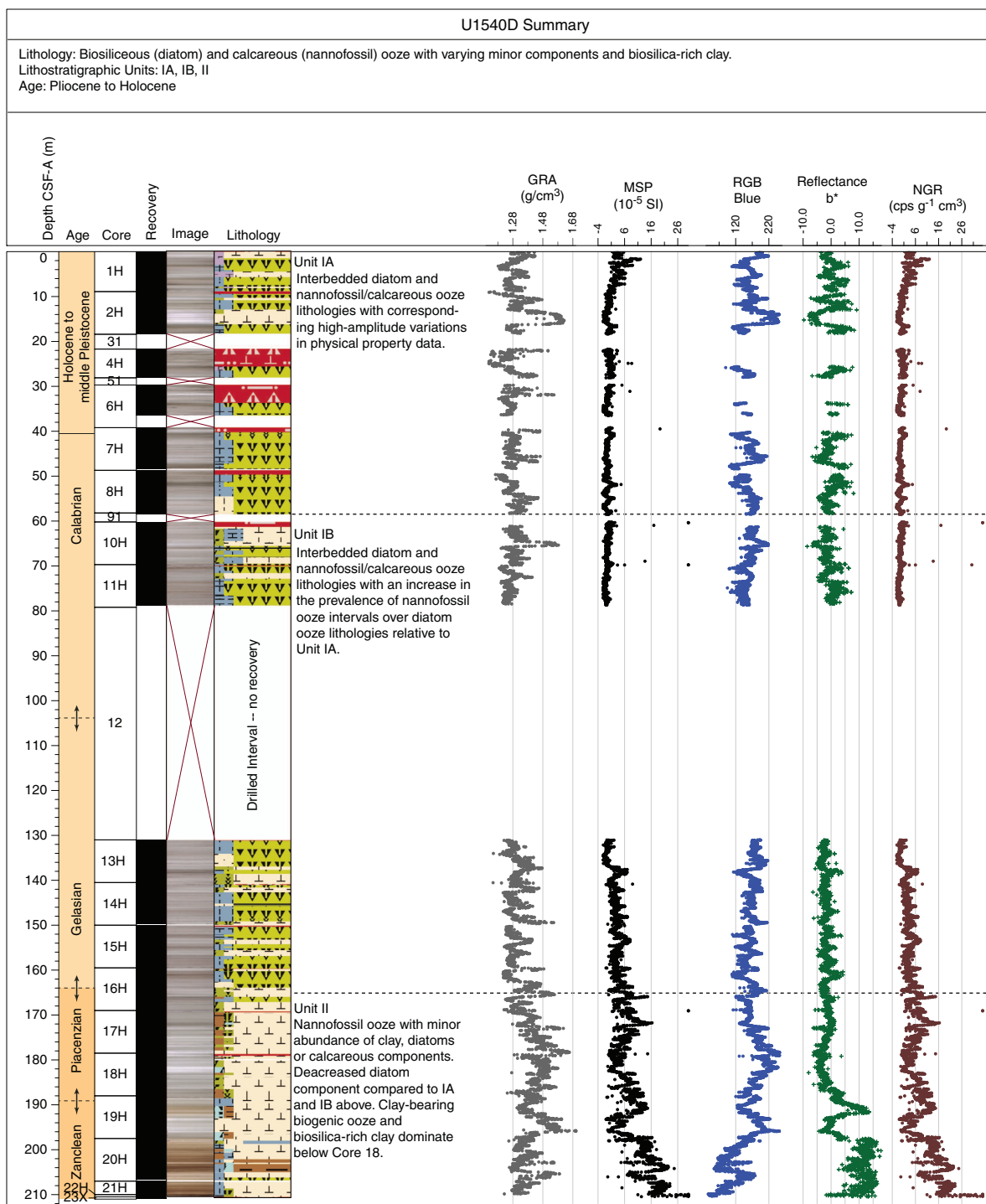
Lithofacies 4

Lithofacies 4 is nannofossil ooze that is heavily bioturbated and often has a massive appearance (see **Bioturbation**). Its color may range from white (N 9/) to very light gray (N 7/). It is characterized by only rare occurrences of carbonate (foraminifers) and various biosiliceous components. Mottled patches of darker grayish colors (10Y 5/1) due to diagenetic iron sulfide overprints are found in this lithofacies. Dropstones are absent. The bed thickness of Lithofacies 4 varies from 0.2 to 3 m. Examples of this lithofacies occur in Sections 383-U1540B-2H-7, 383-U1540D-2H-5, and 383-U1540E-7H-3.

Lithofacies 6

Lithofacies 6 is clay-bearing to clayey biogenic ooze characterized by a greenish gray (10Y 5/1) to gray (5Y 7/1) color and varying degrees of bioturbation (light to heavy; see **Bioturbation**). It contains more than 10% clay-sized lithogenic particles (Figure **F6**). X-ray diffraction (XRD) analyses suggest a variable contribution of clay minerals and quartz to the clay-sized lithogenic fraction (see **X-ray diffraction clay mineralogy**). Lithofacies 6 occurs frequently in the lower sedimentary sequence between ~166 and 202 m CSF-A

Figure F4 (continued). (Continued on next page.)

with a bed thickness of 0.4 to 2 m. Examples of this lithofacies occur in Sections 383-U1540D-18H, 19H, and 383-U1540E-9H-3.

Lithofacies 7

Lithofacies 7 is composed of carbonate- and/or biosilica-bearing clay. It is pale yellowish brown (10YR 8/2) to dark reddish brown (10YR 5/3) and strongly bioturbated, and it contains fragmented biogenic (both calcareous and biosiliceous) components (Figure **F7**). In addition, Fe (hydr)oxides are frequently observed in smear slides obtained from this lithofacies. XRD analysis of decarbonized samples shows a distinct mineralogical composition with decreased abundance of illite and kaolinite in Lithofacies 7 compared to the other lithofacies (see **Bioturbation**). Lithofacies 7 occurs exclusively in the lower part of the sedimentary sequence in Holes U1540D and U1540E with a bed thicknesses of 0.7 to 3.3 m. Representative examples occur in Sections 383-U1540D-20H-4 and 383-U1540E-10H-6.

Figure F4 (continued).
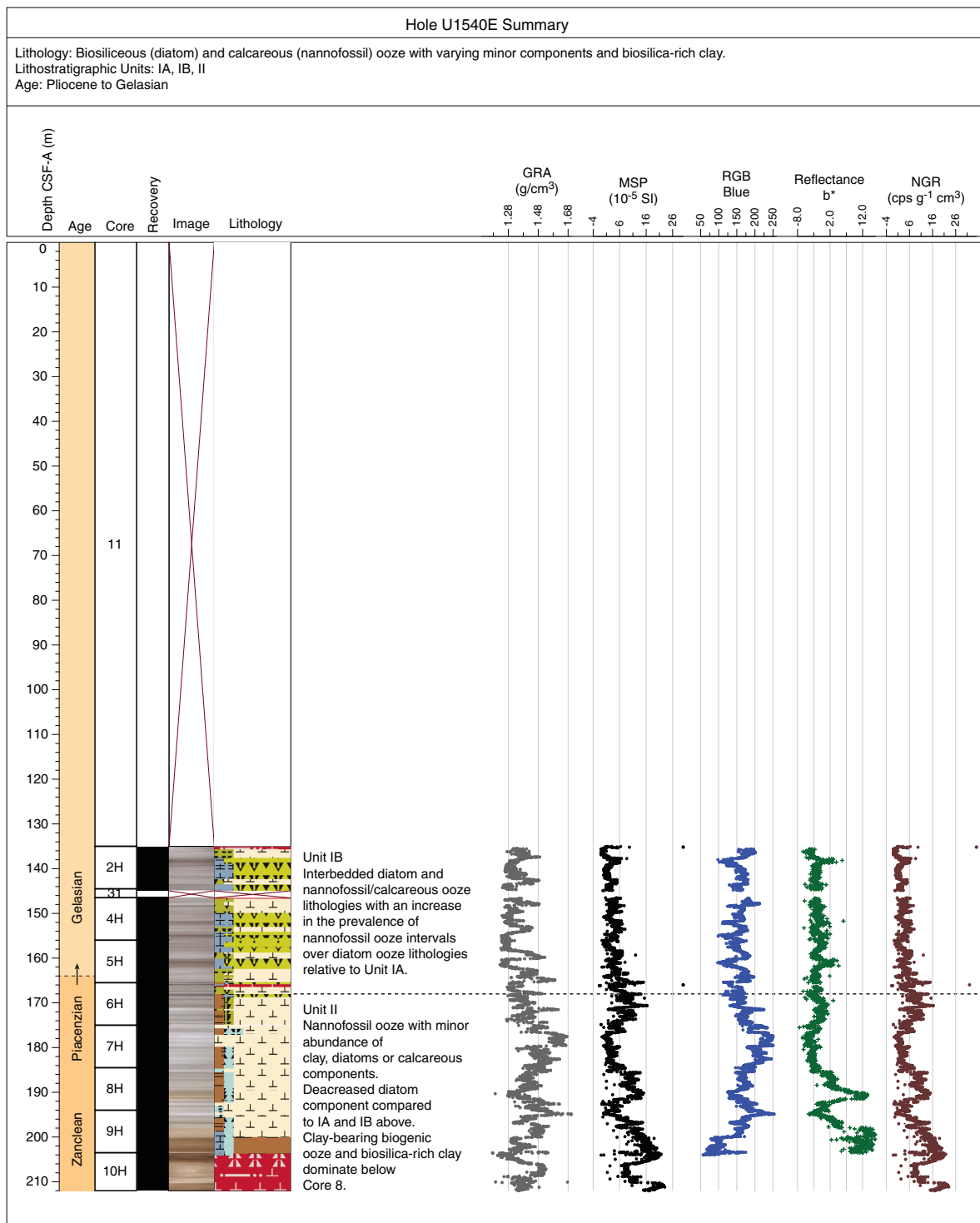
Lithostratigraphic units

Based on the frequency and occurrence of the five lithofacies observed at Site U1540, the sedimentary sequence is divided into two main stratigraphic units, and the youngest unit (Unit I) is di-

vided into two subunits (IA and IB). The criteria used to define unit boundaries are discussed below and highlighted in Figure **F8**. Key unit characteristics, including depths within the overall U1540 sedimentary sequence and corresponding ages derived from the preliminary shipboard age model, are also discussed below.

Figure F5. Primary lithologies used to define sedimentary lithofacies, Site U1540. Pie charts show the lithofacies' relative contribution to Lithostratigraphic Subunits IA and IB and Unit II. The ternary diagram includes a significant clay component at Site U1540 and the creation of Lithofacies 6 and 7.
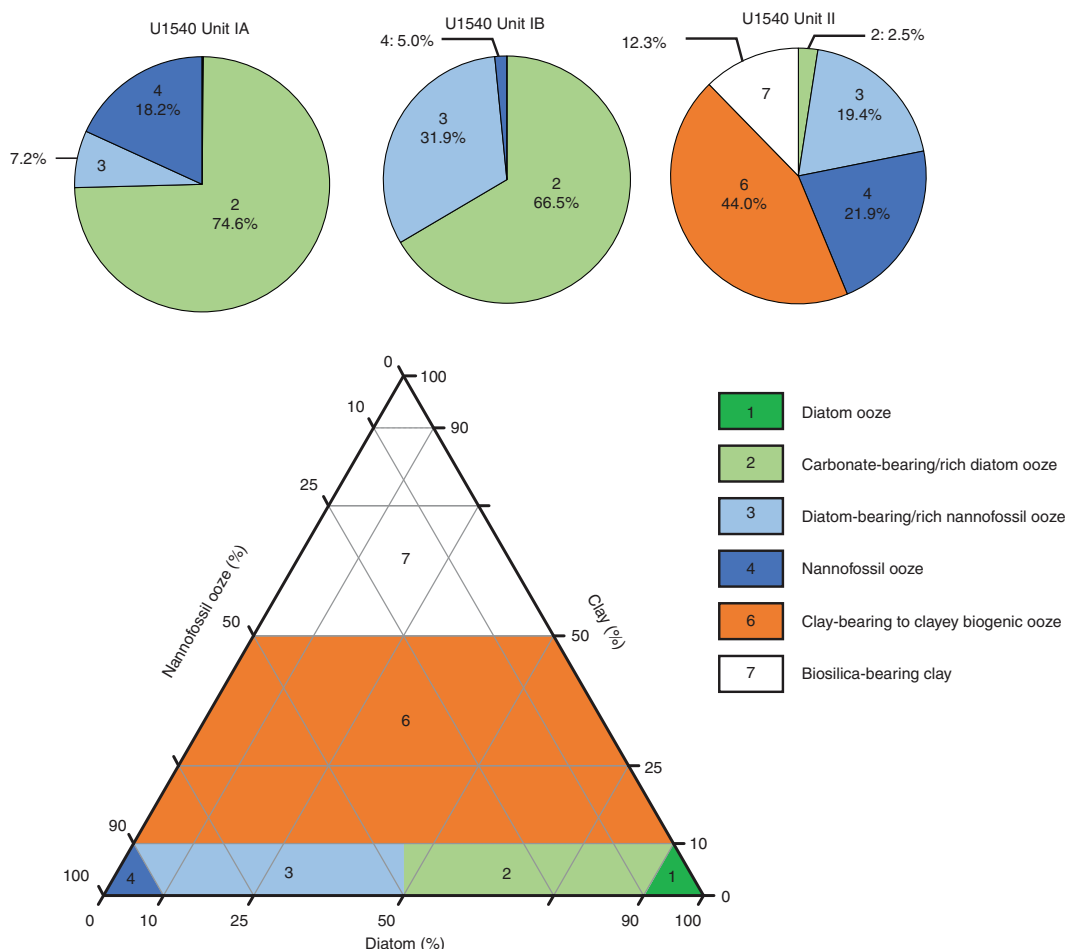

Table T2. Description of lithofacies, Site U1540. **Download table in CSV format.**

Type	Lithofacies	Description	Thickness (m)	Degree of bioturbation	Color	Proportion in lith. units/subunits (%)	Depositional environment
Carbonate-bearing to carbonate-rich diatom ooze	2	Carbonate-bearing to -rich diatom ooze with sporadic diatom mats; minor components (10%–49%): nannofossils and calcareous debris of mostly foraminiferal shells; accessory components (<10%): radiolarians, silicoflagellates, sponge spicules; sporadic dropstones >0.5 cm; frequent mottling associated with thin, elongated, centimeter-scale burrows	0.2–1.5	Moderate–heavy	Light greenish gray (10GY 7/1) to gray (N 6/)	IA: 74.6 IB: 66.5 II: 2.5	Pelagic
Diatom-bearing to diatom-rich nannofossil/ calcareous ooze	3	Diatom-bearing or -rich nannofossil (and/or calcareous) ooze; massive or weak wavy centimeter-scale bedding; minor components mainly diatoms; common mottling due to diagenetic overprinting; low abundance of dropstones	0.1–1.7	Moderate–heavy	White (N9/); light greenish gray (5GY 7/1 and 5GY 8/1); greenish gray (10Y 6/1)	IA: 7.2 IB: 31.9 II: 19.4	Pelagic
Nannofossil ooze	4	Nannofossil/calcareous ooze often with massive appearance; rare foraminifers and biosiliceous components; mottling, diagentic overprinting frequent; absence of dropstones	0.2–3.0	Heavy	White (N 9/); very light gray (N 7/)	IA: 18.2 IB: 1.6 II: 21.9	Pelagic, hydrothermal overprint
Clay-bearing to clayey biogenic ooze	6	Clay-bearing biogenic ooze with >10% clay-sized lithogenics; major lithology dominated by either diatoms or nannofossils; variable contribution of clay minerals and quartz to clay-sized lithogenic fraction; mottling and color banding common	0.4–2.0	Moderate–heavy	Greenish gray (10GY 5/1); gray (N 6/)	II: 44.0	Pelagic
Carbonate and/or biosilica-bearing clay	7	Carbonate and/or biosilica-bearing clay; fragmented biogenic (both calcareous and biosiliceous) components; frequent Fe (hydr)oxides and Fe carbonates; decreased abundance of illite and kaolinite; homogeneous, often mottled	0.7–3.3	Heavy	Pale yellowish brown (10YR 8/2) to dark reddish brown (10YR 5/3)	II: 12.3	Hydrothermal overprint

Figure F6. Representative (A) core and (B) X-ray and photomicrograph images of mineral properties of Lithofacies 6 (clay-bearing biogenic ooze to biosilica-rich clay) in (C) plane-polarized light (PPL) and (D) cross-polarized light (XPL), Hole U1540D.
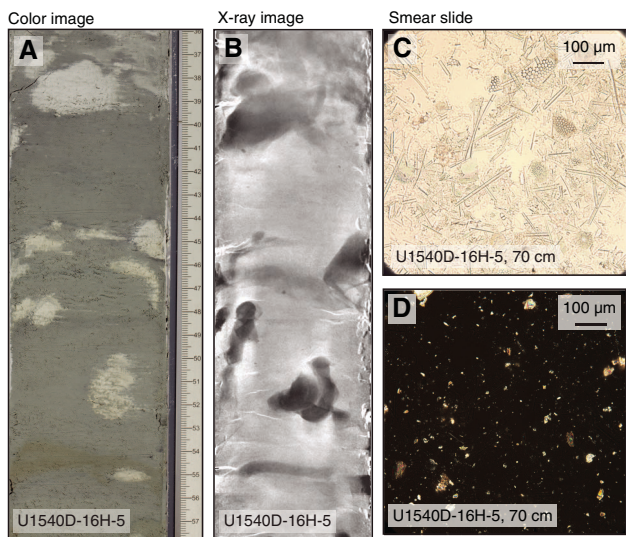
Figure F7. Representative (A) core and (B) X-ray and photomicrograph images of mineral properties of Lithofacies 7 (carbonate- and biosilica-bearing clay) in (C) PPL and (D) XPL, Hole U1540D.
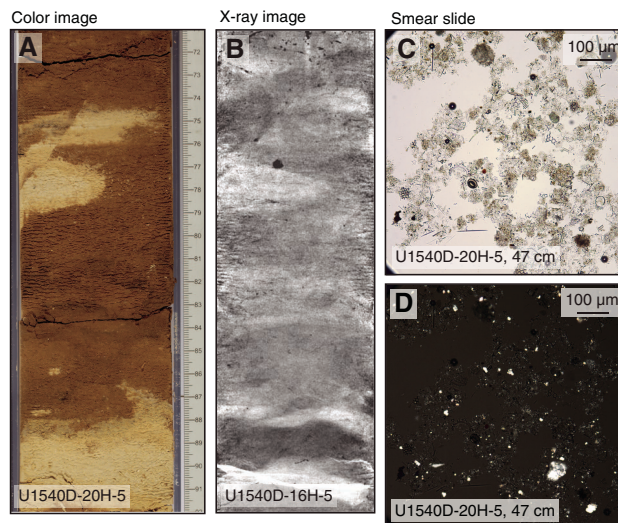
Figure F8. Primary lithostratigraphic variations, Site U1540. Lithostratigraphic units were defined based on the distribution, occurrence, and composition of major lithofacies. Relative ages of units are based on the preliminary Site U1540 shipboard age model (see Stratigraphic correlation).

Unit I
Subunit IA

Intervals: 383-U1540A-1H-1, 0 cm, to 6H-5, 37 cm; 383-U1540B-1H-1, 0 cm, to 10H-2, 28 cm; 383-U1540C-1H-1, 0 cm, to 1H-CC, 15 cm; 383-U1540D-1H-1, 0 cm, to 8H-CC, 21 cm

Depths: Hole U1540A = 0–53.38 m CSF-A, Hole U1540B = 0–56.78 m CSF-A, Hole U1540C = 0–6.77 m CSF-A, Hole U1540D = 0–58.53 m CSF-A, Site U1540 composite section = 0–62.3 m CCSF-A
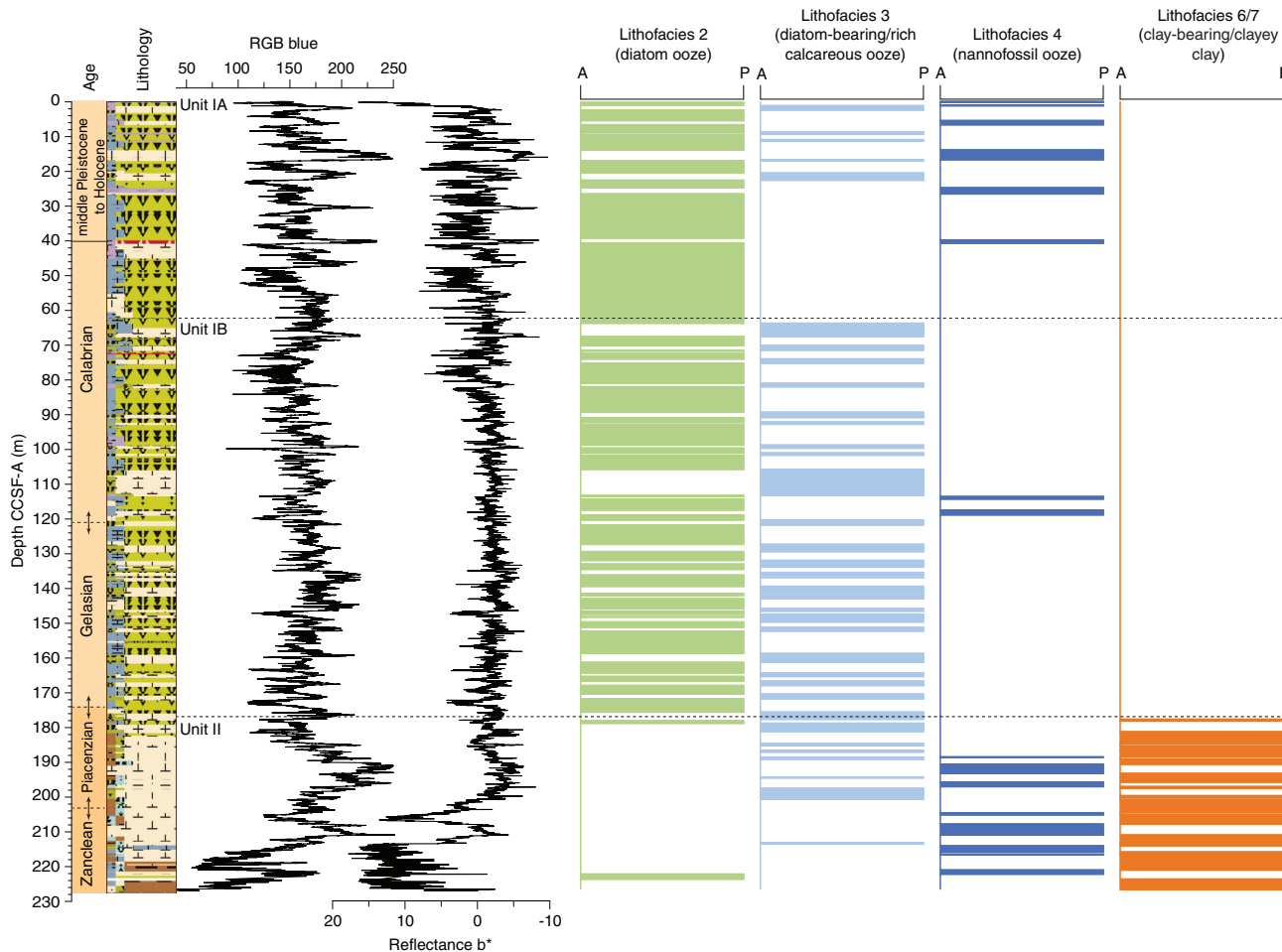
Thickness: 62.3 m

Age: Calabrian and middle Pleistocene to Holocene (younger than 0.98 Ma)

Lithology: biosiliceous (diatom) and calcareous (nannofossil) ooze with varying minor components

Lithostratigraphic Subunit IA consists primarily of Lithofacies 2 (74.6% of the subunit's thickness) and thin intercalated beds of calcareous/nannofossil ooze (Lithofacies 4; 18.2%) or diatom-bearing/rich calcareous ooze (Lithofacies 3; 7.2%). Sediments are moderately to heavily bioturbated, and lithologic transitions are gradual. Subunit IA physical properties are characterized by lower gamma ray attenuation (GRA) bulk density, L*, and red-green-blue (RGB) blue intensity in diatom-dominated lithofacies and correspondingly higher GRA bulk density, L*, and RGB blue intensity in nannofossil/calcareous-dominated lithofacies (see **Integrating physical property measurements with lithofacies observations**).

Subunit IB

Intervals: 383-U1540A-6H-5, 37 cm, to 16H-CC, 47 cm; 383-U1540B-10H-2, 28 cm, to 19H-CC, 36 cm; 383-U1540D-10H-2, 28 cm, to 16H-5, 35 cm; 383-U1540E-2H-1, 0 cm, to 5H-7, 34 cm

Depths: Hole U1540A = 53.38–151.02 m CSF-A, Hole U1540B = 56.78–150.11 m CSF-A, Hole U1540D = 60.20–165.83 m CSF-A, Hole U1540E = 135.00–165.33 m CSF-A; Site U1540 composite section = 62.3–177.8 m CCSF-A

Thickness: 115.5 m

Age: Galesian and Calabrian

Lithology: biosiliceous (diatom) and calcareous (nannofossil) ooze with varying minor components

Lithostratigraphic Subunit IB shows an increased occurrence of diatom-bearing/rich calcareous ooze (Lithofacies 3; 31.9% of the unit) and a reduced occurrence of carbonate-bearing/rich diatom ooze (Lithofacies 2; 66.5%) and calcareous/nannofossil ooze (Lithofacies 4; 1.6%) compared with Subunit IA. Physical properties in Subunit IB include high GRA bulk density and L* values and more prevalent RGB blue–dominated colors indicative of more dominant nannofossil ooze intervals (see **Integrating physical property measurements with lithofacies observations**).

Unit II

Intervals: 383-U1540D-16H-5, 35 cm, to 22H-1, 50 cm; 383-U1540E-5H-7, 34 cm, to 10H-CC, 58 cm

Depths: Hole U1540D = 165.83–210.50 m CSF-A, Hole U1540E = 165.33–213.3 m CSF-A, Site U1540 composite section = 177.8–227.13 m CCSF-A

Thickness: 49.33 m

Age: Zanclean and Piacenzian (Pliocene)

Lithology: nannofossil ooze and clay with varying minor components

Lithostratigraphic Unit II is distinguished from Subunit IB by more dominant calcareous/nannofossil oozes (Lithofacies 3, 19.4% of the unit's thickness; Lithofacies 4, 21.9%) with only a small contribution of carbonate-bearing/rich diatom oozes (Lithofacies 2; 2.5%). Additionally, clay-bearing biogenic oozes in Lithofacies 6 become abundant in the lowermost 20–30 m of Unit II and contribute 44.0% of Unit II's thickness. The bottom 8 m of Unit II are composed exclusively of biogenic-bearing clay (Lithofacies 7), which contributes 12.3% of Unit II thickness (Figure **F5**). Physical properties from Unit II show high GRA bulk densities, L* values, and RGB blue intensity; low natural gamma radiation (NGR) and magnetic susceptibility (MS) in nannofossil ooze intervals; lower GRA bulk density, L*, and RGB blue intensity; and higher NGR, MS, and b* in clay-rich intervals (Figures **F4**, **F8**).

Complementary analyses

Petrology

Drilling operations in Holes U1540D and U1540E were terminated because of the occurrence of impenetrable hard rocks at ~213 m CSF-A. Core catcher samples from Core 383-U1540D-22H revealed fragments of sheet-like, black volcanic glass of various sizes and irregular shape (Figure **F9**). They also contain gravel-sized sedimentary, metamorphic, and granitoid lithic fragments that were likely washed down the borehole from the overlying sediment sequence. Photomicrographs of the volcanic glass reveal phenocrysts of olivine, pyroxene, and tabular elongate plagioclase in a vitric matrix, indicating a basaltic origin (Figure **F10**). Most volcanic glass fragments exhibit conchoidal fracture patterns and palagonitization. The latter is evident as gray and brown mineral coating along fractures and around the rim that possibly consists of iron (hydr)oxides and clays (Expedition 324 Scientists, 2010). The reddish brown color of Lithofacies 7 likely results from weathering products of this volcanogenic material, a hypothesis further supported by the lower abundance of kaolinite and illite in samples from Lithofacies 7 (see **X-ray diffraction clay mineralogy**) and an increase in iron and manganese in X-ray fluorescence (XRF) profiles obtained onboard (see **X-ray fluorescence section-half scanning**).

X-ray diffraction clay mineralogy

XRD analyses were performed on 27 powdered samples obtained from Holes U1540A, U1540B, and U1540D to identify the mineralogy and composition of the lithogenic fraction of sediments at this site. Similar to observations at Site U1539, a wide peak between 18° and 30°2θ occurs in the diffractograms of most samples obtained from Lithofacies 2, which is associated with amorphous biogenic silica from diatoms, radiolarians, and silicoflagellates. Characteristic calcite peaks resulting from incomplete dissolution of carbonate during sample preparation are found in six samples that were obtained from calcareous oozes (i.e., Lithofacies 3 and 4).

To determine the composition of the nonbiogenic sedimentary component, we analyzed diffraction patterns of ten representative samples (Figure **F11**). Detrital minerals such as quartz, feldspar (plagioclase), and phyllosilicates including illite, chlorite, and kaolinite are identified in sediments from Lithofacies 2 and 3. The significant decrease of kaolinite-chlorite peaks at 7.1 Å (12.7°2θ) and 3.54–3.58 Å (24.9°2θ) occurs in most samples after heating to 550°C, indicating the dominance of kaolinite over chlorite. The peak at 10 Å (9°2θ) in untreated samples indicates the presence of illite in most samples, whereas its increase in intensity after heating may result from dehydration of expandable clay minerals. The presence of expandable clay minerals is also supported by the shift of the 14.2 Å peak (6.5°2θ) to the 17 Å peak (5.1°2θ) (Figure **F11**).

Figure F9. Rock fragments found in Core 383-U1540D-22H. A–E. Volcanic glass of various sizes and irregular shapes. F, I. Sedimentary rocks. G. Schist. H. Felsic magmatic rocks. J. Burrow fillings.
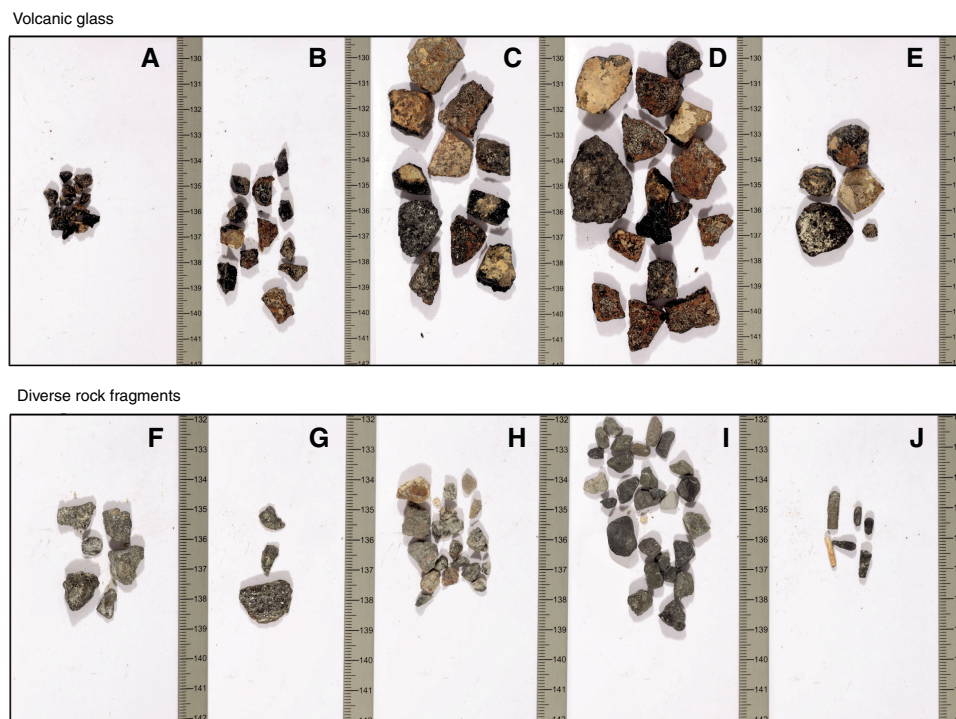
The mineral components of the samples from Lithofacies 6 and 7 differ from those from Lithofacies 2–4. The wide peak between 18° and 30°2θ found in the diffractograms of Lithofacies 2–4 samples is absent, which is indicative of relatively less biogenic silica in Lithofacies 6 and 7. Similarly, the "clay composite" peak at 4.48 Å (19.8°2θ) is most prominent in Lithofacies 7. In this lithofacies, however, peak heights of illite and kaolinite, the common product of alteration and weathering of continental material (Fagel, 2007), are similar to or even lower than those in Lithofacies 2–4, despite the increased proportion of clay components.

The altered glass shards taken from Section 383-U1540D-22H-CC give insights into the possible origin of the clay fraction observed in Lithofacies 6 and 7. Consistent with photomicroscopic observations of the volcanic glass shards (Figure **F10**), the X-ray diffractogram reveals characteristic peaks of plagioclase and possibly pyroxene at 28°2θ. The alteration and weathering of these mafic volcanic materials, seen as palagonitized rims of the volcanic glass, supplies poorly ordered clay minerals and amorphous iron (hydr)oxides to the clay fraction, which are hence difficult to detect in the X-ray diffractogram. Although such disordered features make it difficult to determine the contribution of altered volcanics to the lithogenic fraction, especially to Lithofacies 6, the reddish brown clay component in Lithofacies 7 can likely be attributed to alteration of these volcanic materials.

X-ray fluorescence section-half scanning

To further constrain the elemental composition and mineralogy of Lithofacies 6 and 7 at Site U1540, we performed hand-held XRF analyses on section halves from Cores 383-U1540D-18H through 21H and 383-U1540E-8H through 10H (Figure **F12**). Approximately 45 intervals (covering a 9 mm × 9 mm surface area) were analyzed. The results from Holes U1540D and U1540E are in close agreement. Si and Ca vary in concentration from 2% to 12% and from 0.6% to 18%, respectively, in the lower part of the analyzed interval, and are anticorrelated (Figure **F12F**). The abundances of Si and Ca follow changes in de-

scribed lithology and clay content. Fe percentages gradually increase from 0 to 3% in the analyzed core intervals, a trend opposite to that observed in the Ca record. However, the concentration of Mn increases abruptly at ~215 m CCSF-A below the initial increase in Fe. This increase coincides with a transition to reddish-brown colored sediment and shows no relationship with Ca percentages. Log-ratios of Fe/Ca and Mn/Ca emphasize the gradual increase of Fe toward the bottom of the sedimentary sequence and the abrupt increase in sedimentary Mn with the appearance of clay-containing Lithofacies 7.

Bioturbation

Marked overprints from sediment mixing due to burrowing organisms are observed macroscopically at sedimentary transitions, particularly transitions from biosiliceous to calcareous oozes. Core images of Sections 383-U1540A-10H-3 and 383-U1540D-16H-1 and 16H-5 show a clear downward displacement of overlying younger material (i.e., calcareous ooze) into underlying biosilica-dominated strata (Figure **F13**). These observations are supported by various millimeter- to centimeter-scale burrows seen in most of the X-radiographs, which were systematically taken of each core section. These observations reveal a full spectrum of magnitude of sediment bioturbation (Figure **F14**) from slightly bioturbated to fully homogenized sediments through sediment stirring by benthic organisms (Wetzel and Uchman, 2012).

Integrating physical property measurements with lithofacies observations

The distribution of Site U1540 lithologies was compared to downcore physical property measurements including b*, L*, RGB color, GRA bulk density, NGR, and MS (see **Physical properties** in the Expedition 383 methods chapter [Winckler et al., 2021a]) to identify relationships between lithology and measured downcore data. Four intervals display the diversity of sediment types at Site U1540 (Figure **F15**):

- Subunit IA, Cores 383-U1540A-2H through 4H (10–37 m CSF-A);
- Subunit IB, Cores 383-U1540A-11H through 13H (95–120 m CSF-A);
- Unit II, Cores 383-U1540D-17H and 18H (170–188 m CSF-A); and
- Unit II, Cores 383-U1540D-20H through 22H (202–210.5 m CSF-A).

Downcore physical property and spectrophotometry measurements capture alternations between lithofacies and characteristics of principal lithostratigraphic units at Site U1540. Biosiliceous oozes (Lithofacies 2) are characterized by lower GRA bulk density, lower color reflectance (L*), and less intense colors, particularly in the blue channel obtained by the Section Half Imaging Logger (SHIL) (i.e., lower RGB blue intensity). In contrast, calcareous oozes (Lithofacies 3 and 4) generally exhibit opposite physical property patterns: higher GRA bulk density, higher color reflectance, and stronger response in the blue channel (i.e., higher RGB blue intensity). A principal control of sediment lithology on the main physical sediment properties of the sediment is emphasized by good correlations ($r^2 > 0.65$) between L*, RGB blue intensity, and shipboard mea-

Figure F10. Weathered glass shards taken from sediment (383-U1540D-22H-CC). A. Early stage of palagonite development along the fractures of vitric volcanic glass, magnified under (B) plane light and (C) polarized light. D. Altered, devitrinized rim being replaced by Fe (hydr)oxides and clay under (E) plane light and (F) polarized light. Red boxes in A and D = areas shown in B, C and E, F, respectively. G = glass matrix, O = olivine, Pa = palagonite, Pl = plagioclase, Px = pyroxene.

surements of weight percent calcium carbonate ($CaCO_3$) in bulk sediments (Figure F16). However, MS and NGR counts do not appear closely correlated with alternations between Lithofacies 2, 3, and 4. Clay-dominated sediments from Lithofacies 6 and 7 generally exhibit lower GRA bulk density, L*, and RGB blue intensity and higher NGR, MS, and b* compared to biosilica- and carbonate-dominated lithologies.

Physical property measurements co-vary with the distribution of observed lithofacies in each stratigraphic unit. As illustrated by cores from Subunits IA and IB, the distribution of nannofossil ooze is well captured by increases in GRA bulk density, RGB blue intensity, and L* and an overall decrease in MS (Figure F15). Unit II shows dominant nannofossil ooze (Lithofacies 3 and 4) and is again characterized by high GRA bulk density, L*, and RGB blue intensity and low NGR and MS, except for clay-bearing intervals. The lowermost part of Unit II displays dark brownish clay (Lithofacies 7) with evidently lower GRA bulk density, L*, and RGB blue intensity and higher NGR, MS, and b* compared with intervals of dominantly biogenic sediments.

Summary and preliminary site interpretation

Recurrent alternations between biosiliceous and calcareous sediments in Subunits IA and IB at Site U1540 may broadly reflect glacial–interglacial changes in the export production of opal and carbonate and the corrosiveness of bottom waters at this site, with biosiliceous lithologies dominating glacial intervals and calcareous sediments occurring primarily during interglacial climates (Figure F8). Because mean sedimentation rates are comparable across Subunits IA and IB (see **Stratigraphic correlation**), the change in the frequency and thickness of opal-dominated versus carbonate-dominated sediments therefore suggests a transition in the pacing and duration of glacial versus interglacial periods at the Subunit IA/IB boundary at approximately 1 Ma based on the Site U1540 preliminary shipboard age model.

Generally, the calcareous fraction is more common at Site U1540 than Site U1539. Thin millimeter- to centimeter-scale bands of darker greenish-blackish colors occur throughout most of the cores and might represent past redox fronts in the sediment column associated with redox reactions of iron and manganese at lithologic boundaries (Burdige, 1993). The most recent redox front at ~123 cm in Section 383-U1540B-1H-1 is associated with the lithologic transition presumably from the last glacial maximum to the Holocene (i.e., Termination I).

Lower sedimentation rates and the dominance of nannofossil oozes interbedded with clay-bearing calcareous oozes in Unit II suggest a more stable long-term depositional environment and warmer interglacial conditions prior to the emergence of distinct glacial–interglacial climate variability in the central South Pacific (Figure F8). The Subunit IB/Unit II boundary coincides with the Pliocene–Pleistocene transition at approximately 2.5 Ma (see **Stratigraphic correlation**). Bioturbation is moderate to strong throughout Units I and II and may affect proxy reconstructions at submillennial to millennial timescales. The lowermost part of Unit II shows hydrothermal overprints of the sediments, with increased abundances of Fe and Mn, as well as lithogenic clay components that are likely derived from a local source of highly altered volcanic glass (Figure F10). The presence of such altered volcanic materials in this lowermost part of the core, the encountered hard rock layer, and the estimated age of the oceanic crust (Eagles, 2006) suggest that the site was proximal to a mid-ocean-ridge volcanic source of the EPR during the deposition of the lowermost part of the sediment sequence.

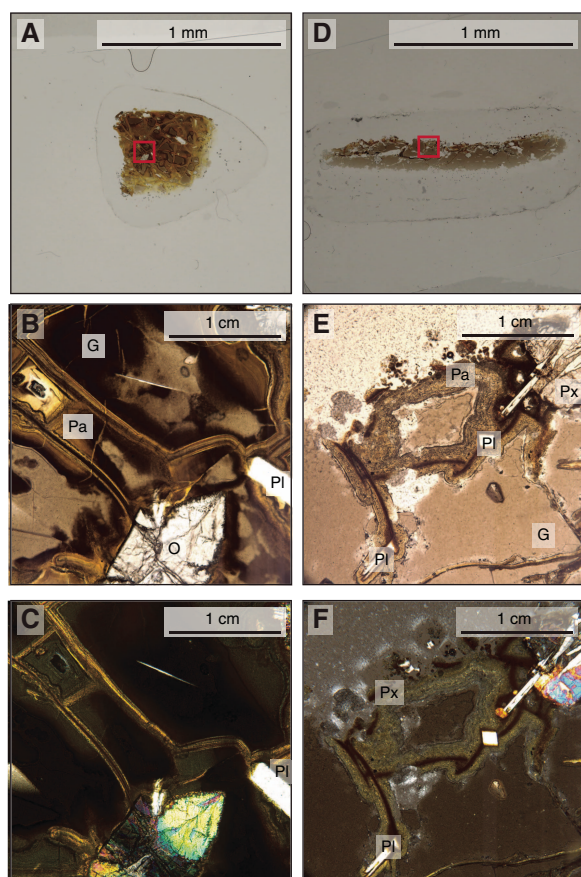Figure F11. X-ray diffractograms of representative samples of each lithofacies in Holes (A) U1540A and (B) U1540D including a glass shard taken from the bottom of Hole U1540D (bottom right). Minerals occurring in the samples include quartz (Qtz), plagioclase (Pl), calcite (C), and pyroxene (Px) and phyllosilicates including illite (Il), chlorite (Chl), kaolinite (K), and their composite ("Clay").

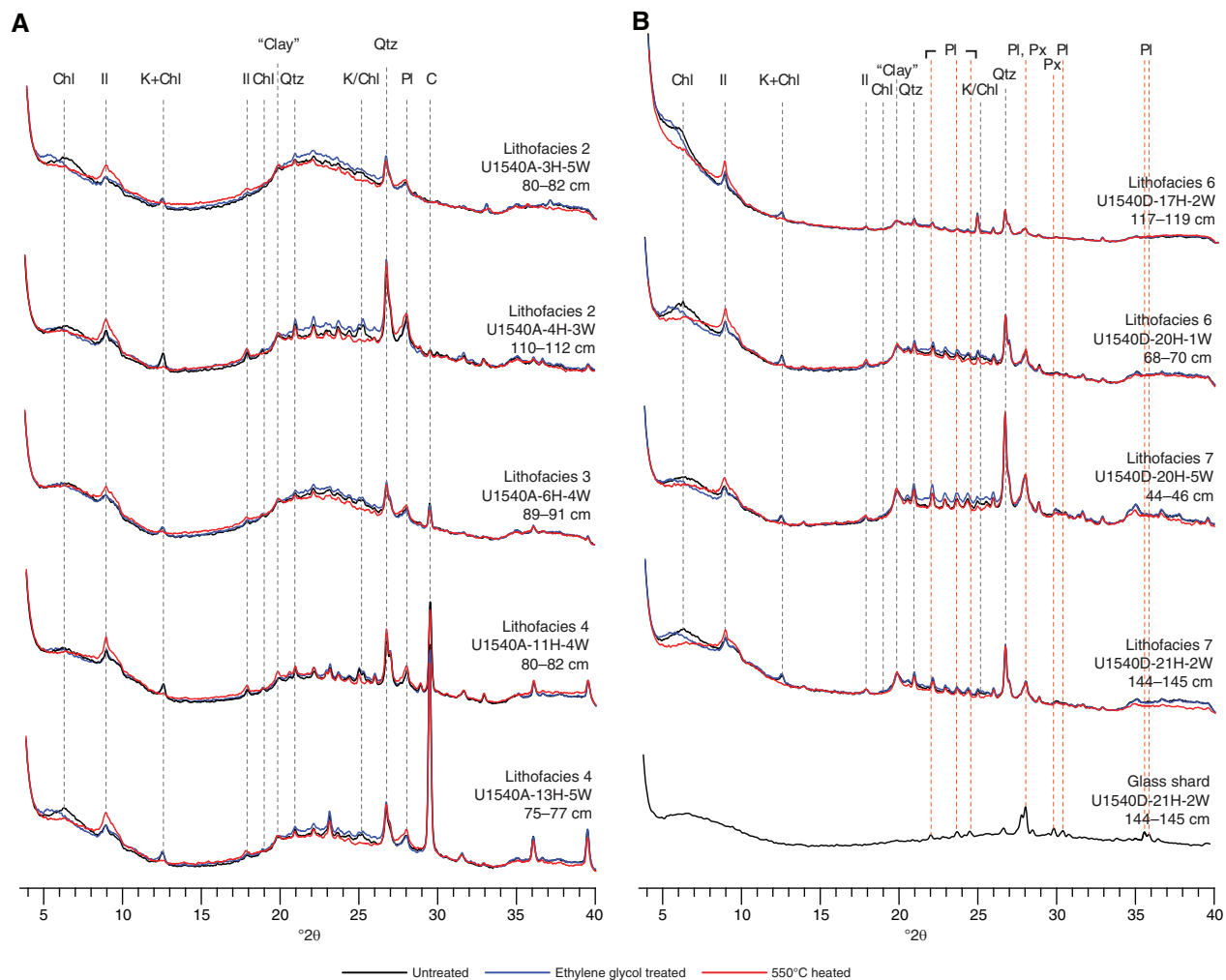Figure F12. Hand-held XRF analyses, Holes U1540D and U1540E. A, C, E, H. Elemental abundances. B, D. Log ratios. F, G, I. Elemental relationships. Nannofossil ooze and clay are major lithologies in the measured cores.
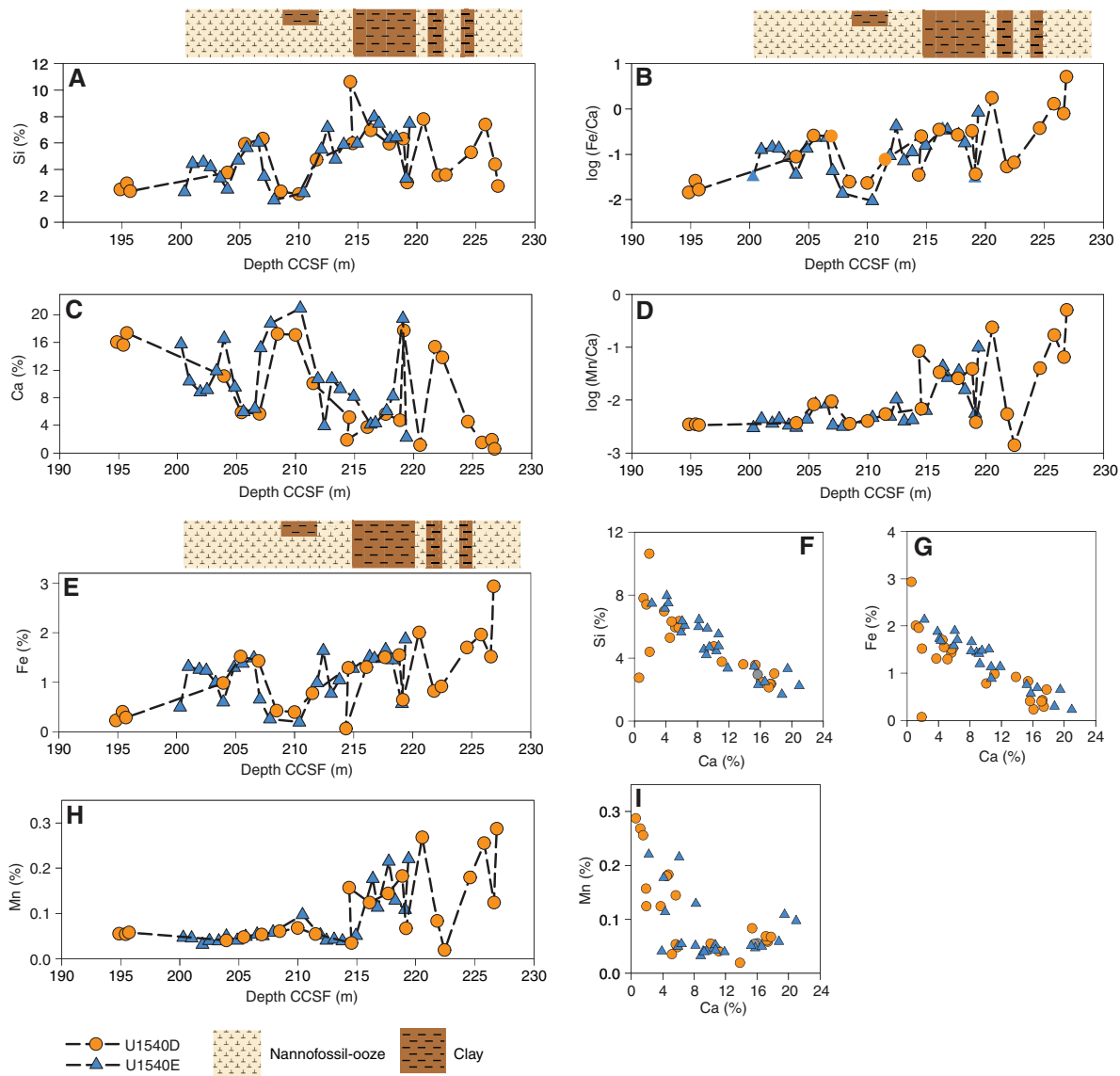
Figure F13. Bioturbation at lithologic transitions from diatomaceous to calcareous ooze, Holes U1540A and U1540D.
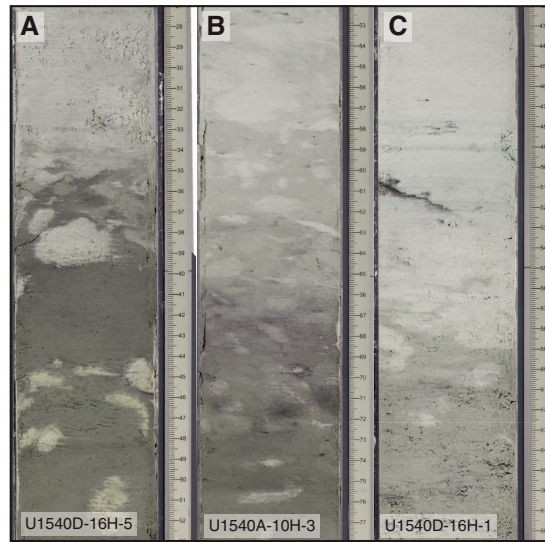
Figure F14. A–E. Various degrees of bioturbation observed in X-radiographs, Holes U1540A and U1540D.
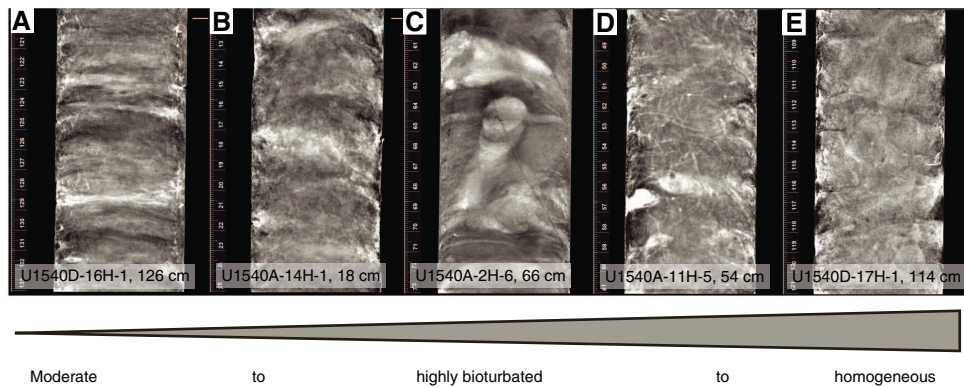
Figure F15. A–D. Characteristic variations in major lithology and physical properties, Holes U1540A and U1540D. Lithologies were determined by visual core description, smear slide analyses, and x-ray imaging. Gray horizontal bars in (A) and (B) denote nannofossil oozes (Lithofacies 3 and 4); white bars denote diatom oozes (Lithofacies 2). Light brown horizontal bars in (C) denote clay-bearing to clayey intervals (Lithofacies 6); white bars denote nannofossil oozes (Lithofacies 4). Brown horizontal bars in (D) denote clays (Lithofacies 7).

Figure F16. Relationships between bulk sedimentary carbonate content and (A) RGB blue and (B) color reflectance L*, Holes U1540A, U1540B, and U1540D. Data points from the Holocene in Hole U1540B were excluded from the Subunit IA regression analysis.

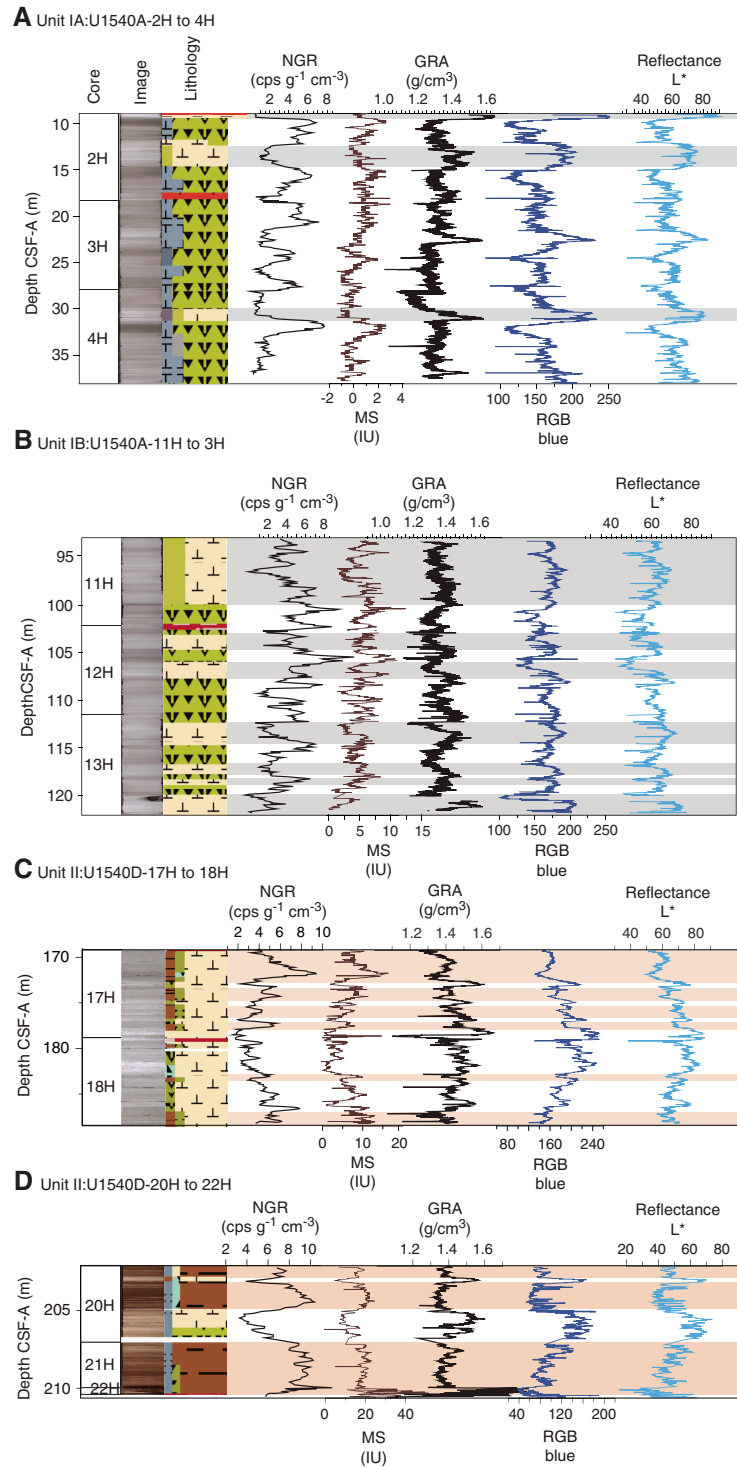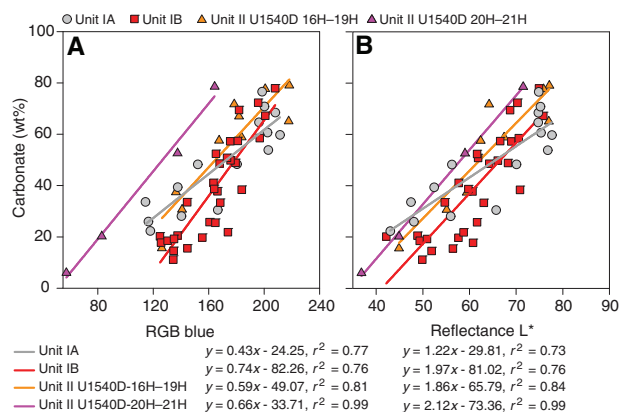|	
—— Unit IA	$y = 0.43x - 24.25$, $r^2 = 0.77$	$y = 1.22x - 29.81$, $r^2 = 0.73$
—— Unit IB	$y = 0.74x - 82.26$, $r^2 = 0.76$	$y = 1.97x - 81.02$, $r^2 = 0.76$
—— Unit II U1540D-16H–19H	$y = 0.59x - 49.07$, $r^2 = 0.81$	$y = 1.86x - 65.79$, $r^2 = 0.84$
—— Unit II U1540D-20H–21H	$y = 0.66x - 33.71$, $r^2 = 0.99$	$y = 2.12x - 73.36$, $r^2 = 0.99$

Biostratigraphy

A ~210 m thick sediment succession of early Pliocene to recent age was recovered at Site U1540. Core catcher samples from Site U1540 were analyzed for siliceous (diatoms, radiolarians, and silico-flagellates) and calcareous (nannofossils, foraminifers, and ostracods) microfossils. Calcareous nannofossils, planktonic and benthic foraminifers, diatoms, and silicoflagellates were also analyzed in the mudline sample. The abundance of the different microfossil groups varies throughout the sequence. The preservation of siliceous microfossils is generally good in most samples. Diatoms are common to abundant and assemblages are diverse in all core catcher samples and in the majority of split-core samples. Radiolarians are abundant in the upper ~178.80 m and common downcore, although some intervals are barren. Silicoflagellate assemblages at Site U1540 consist of 10 species that range from rare to common in most samples. Calcareous nannofossils show variable preservation and abundance from rare to abundant, becoming dominant in discrete nannofossil ooze intervals. Whole coccospheres were observed in the intervals with best nannofossil preservation, usually in oozes. Planktonic and benthic foraminifer preservation is good to moderate in the upper part of the sequence and moderate to poor downcore. Planktonic foraminifer assemblages are primarily characterized by high-latitude and some temperate taxa. The benthic foraminifer *Nuttallides umbonifera*, abundant below ~170 m CSF-A, indicates the presence of warm, corrosive bottom waters. Ostracods occur in very low numbers with good to very good preservation.

The biostratigraphy at Site U1540 is based mainly on Holes U1540A and U1540D, with additional split-core samples taken from Hole U1540E to refine the stratigraphy of the lowermost portion of Site U1540. A ~150 m thick sediment succession ranging in age from late to early Pleistocene was recovered in Hole U1540A. In total, 74 biostratigraphic constraints were recognized with some events occurring in multiple holes, indicating a maximum age of ~4.64 Ma at the bottom of Hole U1540D (~211 m CSF-A). In Samples 383-U1540D-22H-1, 45–50 cm (210.45-210.50 m CSF-A), and 383-U1540E-10H-CC, (213.29-213.34 m CSF-A), a few reworked taxa from the Miocene were observed. Microfossil datums recognized at this site are summarized in Table **T3**; integrated diatom, radiolarian, calcareous nannofossil, and planktonic foraminifer biozonations are shown in Figure **F17**; and an age-depth plot in-

cluding all the biostratigraphic datums and the estimated sedimentation rate is presented in Figure **F18**. No major hiatuses were identified at this site, suggesting a continuous sequence from early Pliocene to Holocene, although the sedimentation rate is very low below ~170 m CSF-A in Hole U1540D. Abundances of the different microfossil groups from Holes U1540A and U1540D are shown in Figures **F19** and **F20**, respectively.

Diatoms

General diatom abundance and distribution

Diatom biostratigraphy at Site U1540 is based on the analysis of 56 smear slides from 2 mudline samples, 29 core catcher samples, and 25 working- and archive-half toothpick samples taken from Holes U1540A, U1540B, U1540D, and U1540E. Diatoms are common to abundant and assemblages are diverse in all core catcher samples and in the great majority of working-half samples examined (Figures **F19**, **F20**; Table **T4**). Five samples have few diatoms: Sample 368-U1540A-1H-5, 66 cm, which is dominated by nannofossils and interpreted to be from Marine Isotope Stage (MIS) 11, and Samples 383-U1540D-21H-CC; 383-U1540D-22H-1, 45–50 cm; 383-U1540E-9H-CC; and 383-U1540E-10H-CC from close to the bottom of Holes U1540D and U1540E, which are sandy and interpreted to represent mixed biogenic ooze with high suck-in drilling disturbances right above the basement (see **Sedimentology**). In addition to a diverse lower Pliocene assemblage, Samples 383-U1540D-21H-CC; 383-U1540D-22H-1, 45–50 cm; 383-U1540E-9H-CC; and 383-U1540E-10H-CC contain few to common reworked specimens of upper to middle Miocene age, mostly *Denticulopsis* species. Preservation is good overall, and most samples exhibit low to moderate fragmentation and dissolution. Two samples near the bottom of Holes U1540D and U1540E, Samples 383-U1540D-21H-CC, 1–6 cm, and 383-U1540E-10H-CC, 53–58 cm, are exceptions and exhibit moderate to high dissolution and fragmentation.

Diatom zonations

Samples from Holes U1540A, U1540B, U1540D, and U1540E preserve an undisturbed sequence of diatom events from the Holocene to about 4.5 Ma. As at Site U1539, the sequence of diatom events, mainly first occurrences (FOs) and last occurrences (LOs), allows the identification of nine diatom zones and six subzones that are consistent with the Northern ACC Diatom Zonation scheme of Zielinski and Gersonde (2002).

Thalassiosira lentiginosa Partial Range Zone

Top: present
Base: last abundant occurrence (LAO) of *Actinocyclus ingens*
Age: 0.64–0 Ma

The *Thalassiosira lentiginosa* Zone is characterized by the mainly dominant occurrence of *Fragilariopsis kerguelensis* and common to few *T. lentiginosa* and *Thalassiothrix antarctica*. The *T. lentiginosa* zone is divided into three subzones by the occurrence of *Hemidiscus karstenii* during the Pleistocene. Uppermost Subzone C is characterized by the absence of *H. karstenii* in mudline Samples 383-U1540B-1H-1, 0 cm (0 m CSF-A), through 2H-CC (12.93–12.98 m CSF-A). Subzone C is bounded from Subzone B by the LAO of *H. karstenii* at the end of MIS 7 at 0.19 Ma; the presence of this species at 0 cm in Core 383-U1540A-1H indicates that the first core of Hole U1540A overpenetrated the seafloor and did not collect the sediment–water interface. The LO of *H. karstenii* was found in Sample 383-U1540B-2H-CC (12.93–12.98 m CSF-A). Zielinski and Ger-

Table T3. Biostratigraphic event datums, Site U1540. Event type: D = diatom datum, R = radiolarian datum, N = calcareous nannofossil datum, F = planktonic foraminifer datum. FO = first occurrence, FCO = first common occurrence, LO = last occurrence, LCO = last common occurrence, LAO = last abundant occurrence. * = datums applied with lower confidence based on preservation, age, or depth uncertainty. References: AO = Anthonissen and Ogg (2012), B = Bohaty et al. (1998), C = Cody et al. (2008) average range model, G = Gersonde (1989), HM = Harwood and Maruyama (1992), L = Lazarus (1992), O = Ogg (2012), S07 = Scott et al. (2007), S = Sjunneskog et al. (2012), T = Tauxe et al. (2012), W = Winter et al., 2012, W94 = Wei (1994), ZG = Zielinski and Gersonde (2002), 181 = ODP Leg 181 Initial Reports (2000), 374 = IODP Expedition 374 diatom and radiolarian biostratigraphic frameworks (David Harwood and Giuseppe Cortese, pers. comm.), 383 = regional datum age revised for IODP Expedition 383. (Continued on next page.) **Download table in CSV format.**

Constraint number	Type	Bioevent	Age (Ma)	Top core, section, interval (cm)	Top depth CSF-A (m)	Bottom core, section, interval (cm)	Bottom depth CSF-A (m)	Reference
				383-U1540A-		383-U1540A-		
1	D	LO *Fragilariopsis fossilis*	0.3	1H-1, 140	1.40	1H-3, 60	3.62	383
2	N	FO *Emiliania huxleyi**	0.29	1H-4, 133	5.85	1H-5, 66	6.68	AO
3	D	FCO *Hemidiscus karstenii*	0.42	1H-5, 66	6.68	1H-CC, 11–16	8.88–8.93	ZG
4	D	LO *Actinocyclus ingens*	0.42	1H-5, 66	6.68	1H-CC, 11–16	8.88–8.93	ZG
5	D	LO *Rouxia constricta*	0.43–0.5	1H-CC, 11–16	8.88–8.93	2H-CC, 9–14	18.72–18.77	ZG, C08
6	R	LO *Stylatractus universus*	0.43	1H-CC, 11–16	8.88–8.93	2H-CC, 9–14	18.72–18.77	L, 374
7	N	LO *Pseudoemiliania lacunosa*	0.44	2H-1, 50	9.50	2H-2, 117	11.67	AO
8	D	LCO *Actinocyclus ingens*	0.64	2H-CC, 9–14	18.72–18.77	3H-CC, 16–21	28.56–28.61	ZG
9	F	LO *Globoconella puncticulata puncticuloides**	0.7	2H-CC, 9–14	18.72–18.77	3H-CC, 16–21	28.56–28.61	S07, 181
10	N	LO *Reticulofenestra asanoi*	0.91	3H-CC, 16–21	28.56–28.61	4H-2, 85	30.35	AO
11	R	LO *Antarctissa cylindrica*	0.64	3H-CC, 16–21	28.56–28.61	4H-CC, 35–40	37.89–37.94	L, 374
12	N	LO *Gephyrocapsa omega**	0.61–1.4	4H-4, 10	32.63	5H-CC, 15–20	47.33–47.38	AO
13	F	FO *Truncorotalia crassaformis hessi*	0.75	4H-CC, 35–40	37.89–37.94	5H-CC, 15–20	47.33–47.38	AO
14	D	FO *Rouxia constricta**	0.91–1.23	5H-CC, 15–20	47.33–47.38	6H-CC, 5–10	56.44–56.49	C, ZG
15	D	LO *Thalassiosira elliptipora*	0.82	5H-CC, 15–20	47.33–47.38	6H-CC, 5–10	56.44–56.49	ZG
16	D	LO *Thalassiosira fasciculata*	0.87–0.89	5H-CC, 15–20	47.33–47.38	6H-CC, 5–10	56.44–56.49	C, ZG
17	R	LO *Pterocanium charybdeum trilobum*	0.86	6H-CC, 5–10	56.44–56.49	7H-CC, 5–10	64.75–64.8	L, 374
18	N	FCO *Reticulofenestra asanoi**	1.14	7H-CC, 5–10	64.75–64.80	8H-1, 90	65.70	AO
19	D	FCO *Thalassiosira elliptipora*	1.01–1.13	7H-CC, 5–10	64.75–64.80	8H-CC, 15–20	74.50–74.55	ZG
20	N	LO *Large Gephyrocapsa* (>5.5 µm)	1.24	8H-3, 40	68.20	8H-4, 142	70.72	AO
21	N	LO *Helicosphaera sellii*	1.26–1.34	8H-6, 30	72.60	8H-CC, 15–20	74.50–74.55	AO
22	D	LO *Shionodiscus tetraoestrupii* var. *reimeri*	1.31–1.34	9H-4, 140	80.19	9H-6, 130	83.07	C, ZG
23	D	LO *Fragilariopsis barronii*	1.19–1.48	9C-CC, 19–24	83.90–83.95	10H-2, 90	86.2	C, ZG
24	N	FCO *Large Gephyrocapsa* (>5.5 µm)	1.46	9H-CC, 19–24	83.90–83.95	10H-2, 90	86.200	AO
25	D	LO *Rouxia antarctica*	1.35–1.61	10H-6, 45	91.76	10H-CC, 29–34	93.77–93.82	ZG
26	D	LO *Proboscia barboi*	1.6–1.82	10H-CC, 29–34	93.77–93.82	11H-CC, 8–13	102.97–103.02	C, ZG
27	D	FO *Fragilariopsis separanda*	1.37–1.45	11H-CC, 8–13	102.97–103.02	12H-CC, 23–28	112.49–112.54	C
28	N	LO *Calcidiscus macintyrei*	1.6	11H-CC, 8–13	102.97–103.02	12H-2, 70	105.00	AO
29	R	LO *Cycladophora pliocenica*	1.81	11H-CC, 8–13	102.97–103.02	12H-CC, 23–28	112.49–112.54	L, 374
30	R	FO *Triceraspyris antarctica*	1.88	11H-CC, 8–13	102.97–103.02	12H-CC, 23–28	112.49–112.54	L, 374
31	D	FO *Fragilariopsis kerguelensis*	1.95–2.2	12H-CC, 23–28	112.49–112.54	13H-CC, 16–21	121.83–121.88	C, ZG
32	D	LO *Thalassiosira kolbei*	1.98–2.08	12H-CC, 23–28	112.49–112.54	13H-CC, 16–21	121.83–121.88	C, ZG
33	D	LO *Fragilariopsis matuyamae*	2–2.12	12H-CC, 23–28	112.49–112.54	13H-CC, 16–21	121.83–121.88	C, ZG, 374
34	R	LO *Eucyrtidium calvertense*	1.92	12H-CC, 23–28	112.49–112.54	13H-CC, 16–21	121.83–121.88	L, 374
35	D	LO *Fragilariopsis matuyamae* var. *heteropola*	2.08–2.11	13H-CC, 16–21	121.83–121.88	14H-CC, 31–36	131.91–131.96	C
36	R	LO *Helotholus vema*	2.4	14H-CC, 31–36	131.91–131.96	15H-CC, 24–29	141.08–141.13	L, 374
37	R	LO *Desmospyris spongiosa*	2.48	15H-CC, 24–29	141.08–141.13	16H-CC, 42–47	150.97–151.02	L, 374
				383-U1540B-		383-U1540B-		
38	D	LO *Hemidiscus karstenii*	0.19	1H-CC, 10–15	3.08–3.12	2H-CC, 9–14	12.93–12.98	HM, ZG
39	D	Presence *Thalassiosira vulnifica**	>2.2–2.56	Minimum age at base of hole	—	19H-CC, 31–36	150.06–150.11	HM, ZG, 374
				383-U1540D-		383-U1540D-		
40	D	LO *Actinocyclus karstenii*	2.13–2.16	13H-CC, 18–23	140.94–140.99	14H-CC, 5–10	149.75–149.80	C
41	D	LO *Thalassiosira vulnifica*	2.2–2.56	14H-CC, 5–10	149.75–149.80	15H-CC, 22–27	159.51–159.56	HM, ZG, 374
42	D	LO *Thalassiosira insigna*	2.45–2.6	14H-CC, 5–10	149.75–149.80	15H-CC, 22–27	159.51–159.56	C, 374
43	R	LO *Helotholus vema*	2.4	14H-CC, 5–10	149.75–149.80	15H-CC, 22–27	159.51–159.56	L, 374
44	D	FO *Fragilariopsis matuyamae* var. *heteropola**	2.2–2.29	15H-CC, 22–27	159.51–159.56	16H-2, 140	162.40	C
45	D	FO *Fragilariopsis matuyamae*	2.36–2.4	15H-CC, 22–27	159.51–159.56	16H-2, 140	162.40	C, ZG
46	D	LO *Fragilariopsis interfrigidaria*	2.4–2.96	15H-CC, 22–27	159.51–159.56	16H-2, 140	162.40	C, HM, ZG
47	D	LO *Fragilariopsis weaveri*	2.54–2.66	16H-2, 140	162.40	16H-4, 140	165.39	ZG
48	D	LCO *Thalassiosira inura*	2.53–2.65	16H-6, 140	168.38	16H-CC, 11–16	169.19–169.24	C, ZG
49	D	FO *Shionodiscus tetraoestrupii* var. *reimeri*	2.3–2.66	16H-CC, 11–16	169.19–169.24	17H-CC, 25–30	178.80–178.85	C, ZG, 374
50	D	FO *Thalassiosira vulnifica*	3.14–3.18	16H-CC, 11–16	169.19–169.24	17H-CC, 25–30	178.80–178.85	C
51	D	LO *Thalassiosira striata*	2.89–2.96	16H-CC, 11–16	169.19–169.24	17H-CC, 25–30	178.80–178.85	C
52	R	LO *Desmospyris spongiosa*	2.48	16H-CC, 11–16	169.19–169.24	17H-CC, 25–30	178.80–178.85	L, 374
53	R	FO *Cycladophora davisiana*	2.61	16H-CC, 11–16	169.19–169.24	17H-CC, 25–30	178.80–178.85	L, 374
54	D	FO *Thalassiosira kolbei**	3.8–4.02	17H-CC, 25–30	178.80–178.85	18H-CC, 19–24	188.30–188.35	C,
55	N	LO *Reticulofenestra pseudoumbilicus*	3.7	19H-1, 20	188.20	19H-2, 131	190.82	AO
56	D	LO *Thalassiosira complicata*	3.36–3.44	18H-CC, 19–24	188.30–188.35	19H-1, 140	189.40	C
57	F	LO *Globoconella puncticulata**	1.88–2.39	18H-CC, 19–24	188.30–188.35	19H-1, 51–52	188.51–188.52	W94

Table T3 (continued).

Constraint number	Type	Bioevent	Age (Ma)	Top core, section, interval (cm)	Top depth CSF-A (m)	Bottom core, section, interval (cm)	Bottom depth CSF-A (m)	Reference
58	R	LO *Larcopyle polyacantha titan*	3.48	18H-CC, 19–24	188.30–188.35	19H-CC, 18–23	197.99–198.04	L, 374
59	D	FO *Thalassiosira insigna*	3.14–3.42	19H-1, 140	189.4	19H-2, 140	190.91	C, ZG
60	D	FO *Thalassiosira fasciculata**	4.25–4.42	19H-1, 140	189.4	19H-2, 140	190.91	C
61	D	FO *Fragilariopsis weaveri*	3.51–3.55	19H-2, 140	190.91	19H-3, 140	192.44	C, ZG
62	F	LO *Hirsutella margaritae**	3.85	19H-3, 130–131	192.34–192.35	19H-CC, 18–23	197.99–198.04	AO
63	D	LO *Fragilariopsis arcula*	3.84–4.09	19H-3, 140	192.44	19H-4, 140	193.95	C, ZG
64	D	LO *Fragilariopsis aurica**	4.2–4.35	19H-4, 140	193.95	19H-5, 140	195.47	C, HM, 374
65	D	LO *Fragilariopsis praecurta*	4.19–4.28	19H-4, 140	193.95	19H-5, 140	195.47	C, 374
66	D	LO *Fragilariopsis clementia**	4.51–4.6	19H-4, 140	193.95	19H-5, 140	195.47	C, 374
67	D	FO *Fragilariopsis interfrigidaria*	3.9–4.19	19H-5, 140	195.47	19H-6, 140	196.98	C, 374
68	D	FO *Fragilariopsis barronii*	4.28–4.45	19H-CC, 18–23	197.99–198.04	20H-CC, 0–6	206.65–206.71	C, 374
69	D	FO *Thalassiosira striata*	4.3–4.64	19H-CC, 18–23	197.99–198.04	20H-CC, 0–6	206.65–206.71	C, HM
70	R	FO *Helotholus vema*	<4.59	20H-CC, 0–6	206.65–206.71	21H-CC, 1–6	210.35–210.40	L,374
71	N	LO *Amaurolithus primus*	4.5	20H-1, 55	198.05	20H-1, 90	198.40	AO
72	D	Presence *Thalassiosira inura**	<4.71–4.77	22H-1, 45–50	210.45–210.50	Maximum age at base of hole	—	C
73	D	Presence *Thalassiosira complicata**	<4.64–4.71	22H-1, 45–50	210.45–210.50	Maximum age at base of hole	—	C
				383-U1540E-		383-U1540E-		
74	N	LO *Amaurolithus primus*	4.5	9H-5, 64	200.68	9H-7, 38	203.45	AO
75	D	Presence *Thalassiosira inura**	<4.71–4.77	9H-CC, 21–26	204.01–204.06	Maximum age near base of hole	—	C

sonde (2002) defined the boundary between Subzones B and A as the first common occurrence (FCO) of *H. karstenii* at the beginning of MIS 11 at 0.42 Ma, which is present in Sample 383-U1540A-1H-5, 66 cm (6.68–6.73 m CSF-A), and absent from Sample 1H-CC (8.88–8.93 m CSF-A). This event occurs across the same interval as the LO of *A. ingens*, which is present in Sample 1H-CC (8.88–8.93 m CSF-A) but absent from Sample 1H-5, 66 cm (6.68–6.73 m CSF-A) and which marks the transition from MIS 12 to MIS 11 at 0.42 Ma (Zielinski and Gersonde, 2002). We therefore elect to use the two events interchangeably to define the Subzone B/A boundary at all Expedition 383 sites. Similar to Site U1539, *Fragilariopsis fossilis* was noted in rare abundance in Subzones B and C. The last appearance of *Rouxia constricta* was found in Subzone B in Sample 2H-CC (18.72–18.77). The bottom of the *T. lentiginosa* Zone is characterized by the LAO of *A. ingens* in Sample 3H-CC (28.56–28.61 m CSF-A).

Actinocyclus ingens Partial Range Zone

Top: LAO of *A. ingens*
Base: LO of *Proboscia barboi*
Age: 1.8–0.64 Ma

The diatom assemblage of the *A. ingens* Zone is characterized by dominant to common *Thalassiothrix antarctica*, common *F. kerguelensis*, and common to few *T. lentiginosa*. *A. ingens* is common across the entire zone and constrains the top of the zone by a significant drop in abundance to rare. The *A. ingens* Zone is divided into three subzones. The transition from Subzone C to Subzone B is marked by the FCO of *Thalassiosira elliptipora* between 1.04 and 1.1 Ma in Sample 383-U1540A-7H-CC (64.75–64.80 m CSF-A). The boundary between Subzones A and B is defined by the LO of *Fragilariopsis barronii* at about 1.3 Ma in Sample 10H-2, 90 cm (86.20 m CSF-A). Other important events in the *A. ingens* Zone are the LO of *Thalassiosira fasciculata* at 0.87–0.89 My before present (BP) in Sample 6H-CC (56.44–56.49 m CSF-A), the LO of *Shionodiscus tetraoestrupii* var. *reimeri* between 1.35 and 1.42 My BP in Sample 9H-6, 130 cm (83.07 m CSF-A), and the LO of *Rouxia antarctica* between 1.35 and 1.56 Ma in Sample 10H-CC (93.77–93.82

m CSF-A). The base of the *A. ingens* Zone is defined by the LO of *P. barboi*, which occurs below Sample 383-U1540D-10H-CC (93.77–93.82 m CSF-A).

Proboscia barboi Partial Range Zone

Top: LO of *P. barboi*
Base: LO of *Thalassiosira kolbei*
Age: 2.0–1.8 Ma

The top of the *P. barboi* zone is defined by the LO of *P. barboi* in Sample 383-U1540A-11H-CC (102.97–103.02 m CSF-A). The diatom assemblage of this zone is characterized by common *F. kerguelensis* and *Fragilariopsis ingens*; few *F. barronii*, *T. lentiginosa*, and *Thalassiothrix antarctica*; and rare *S. tetraoestrupii* var. *reimeri*. Remarkable is the common appearance of long, slender varieties of *Thalassionema nitzschioides* and the FO of *F. kerguelensis* in Sample 12H-CC (112.49–112.54 m CSF-A). The base of the *P. barboi* Zone is defined by the LO of *T. kolbei*, which occurs below Sample 383-U1540D-12H-CC (112.49–113.54 m CSF-A).

Thalassiosira kolbei/Fragilariopsis matuyamae Concurrent Range Zone

Top: LO of *T. kolbei*
Base: LO of *Thalassiosira vulnifica*
Age: 2.5–2.0 Ma

The top of the *T. kolbei/Fragilariopsis matuyamae* zone is defined by the LO of *T. kolbei* in Sample 383-U1540A-13H-CC (121.83–121.88 m CSF-A). Further constraint of the top of the zone is provided by the LO of *F. matuyamae* in Sample 13H-CC (121.83–121.88 m CSF-A). The FO of *F. matuyamae* occurs in Sample 383-U1540D-15H-CC (159.51–159.56 m CSF-A), and the appearance of *F. matuyamae* var. *heteropolara* (Gersonde and Bárcena, 1998) was noted in Samples 383-U1540A-14H-CC (131.91–131.96 m CSF-A) and 383-U1540D-15H-CC (159.51–159.56 m CSF-A). The diatom assemblage of this zone is characterized by common *F. ingens* and *F. barronii* and few *P. barboi*, *T. lentiginosa*, *Thalassiothrix antarctica*,

Figure F17. Diatom, radiolarian, calcareous nannofossil, and planktonic foraminifer zonations and biostratigraphic events, Site U1540.
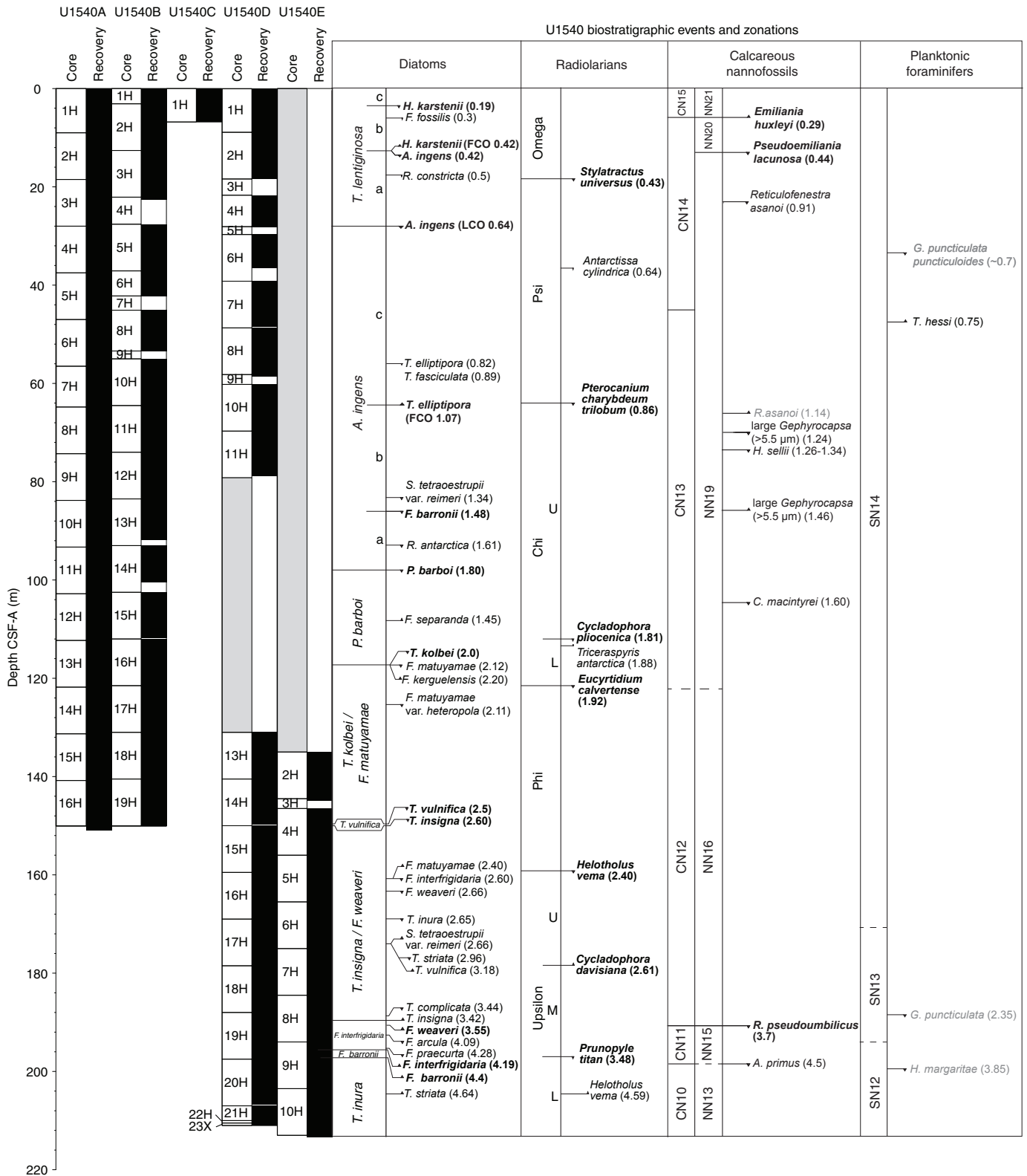
Figure F18. Age-depth plot, Holes U1540A and U1540D. FO = first occurrence, LO = last occurrence, A = Hole U1540A, D = Hole U1540D.
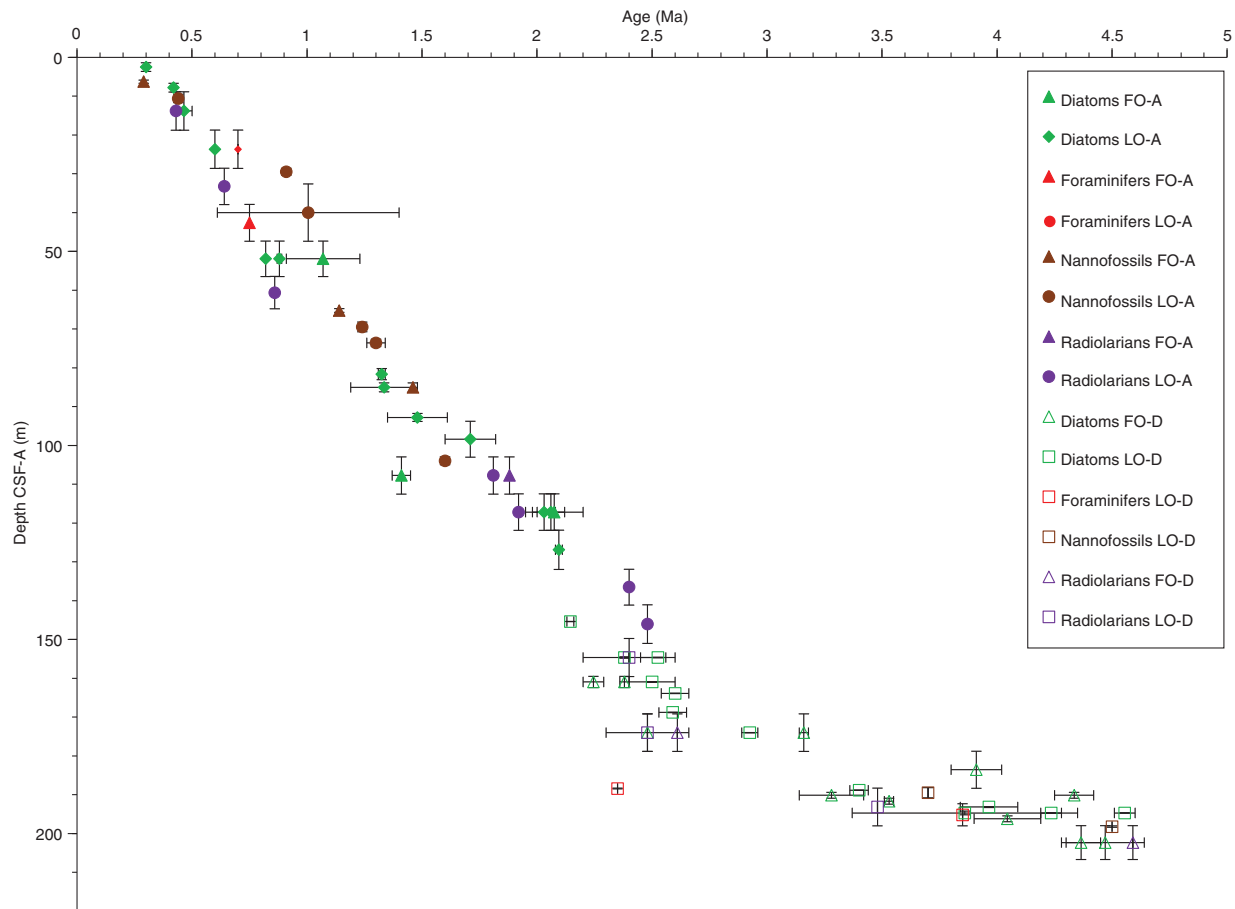

Figure F19. Distribution of siliceous and calcareous microfossils, Hole U1540A. B = barren, R = rare, F = few, C = common, A = abundant, D = dominant.
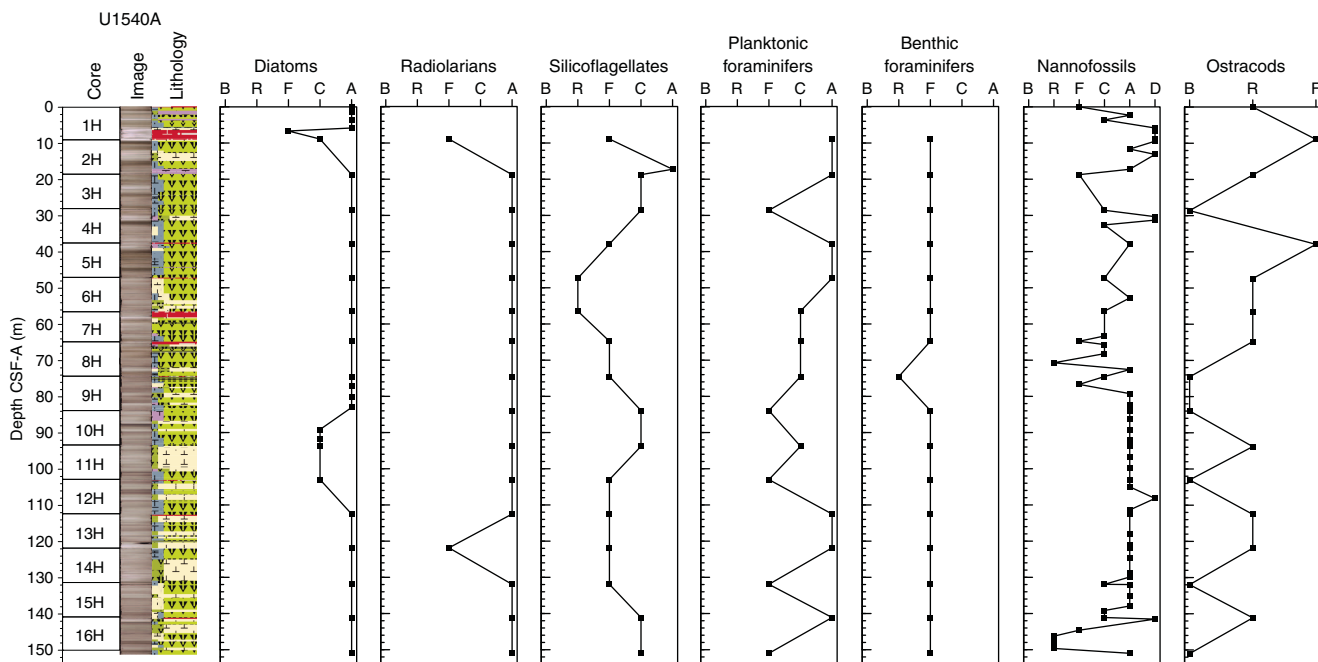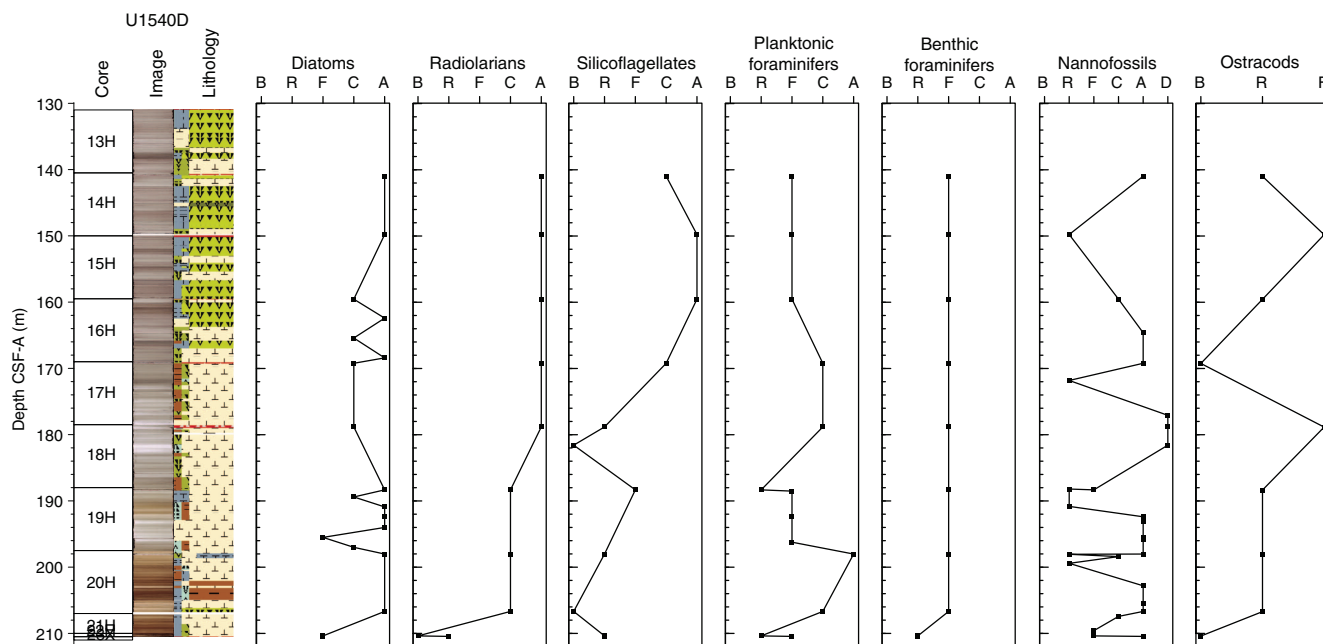
Figure F20. Distribution of siliceous and calcareous microfossils, Hole U1540D. B = barren, R = rare, F = few, C = common, A = abundant, D = dominant.

Table T4. Distribution chart of diatoms, Holes U1540A, U1540B, U1540D, and U1540E. **Download table in CSV format.**

and *S. tetraoestrupii* var. *reimeri*. Notably, long, slender varieties of *T. nitzschioides* occur at common to few abundance across the zone. The LO of *Actinocyclus karstenii* occurs in Sample 383-U1540D-14H-CC (149.75–149.80 m CSF-A), and the base of the *T. kolbei/F. matuyamae* Zone is defined by the LO of *T. vulnifica*, which occurs below Sample 383-U1540D-14H-CC (149.75–149.80 m CSF-A).

Thalassiosira vulnifica Partial Range Zone

Top: LO of *T. vulnifica*
Base: LO of *Thalassiosira insigna*
Age: 2.6–2.5 Ma

The top of the *T. vulnifica* Zone is defined by the LO of *T. vulnifica* between Samples 383-U1540D-14H-CC (149.75–149.80 m CSF-A) and 15H-CC (159.51–159.56 m CSF-A). The species is also present in Sample 383-U1540B-19H-CC (150.06–150.11 m CSF-A), further constraining the top of the zone at Site U1540. The diatom assemblage of this zone is characterized by common to few *F. barronii*, common to few *Thalassiothrix antarctica*, and few to rare *F. ingens, H. karstenii, T. lentiginosa, T. kolbei*, and *S. tetraoestrupii* var. *reimeri*. The base of the zone is defined by the LO of *T. insigna*, which also occurs between Samples 383-U1540D-14H-CC (149.75–149.80 m CSF-A) and 15H-CC (159.51–159.56 m CSF-A). Post-cruise refinement of the low-resolution shipboard biostratigraphy will therefore be necessary to resolve the true thickness of the *T. vulnifica* Zone at Site U1540.

Thalassiosira insigna/Fragilariopsis weaveri Concurrent Range Zone

Top: LO of *T. insigna*
Base: FO of *Fragilariopsis weaveri*
Age: 3.5–2.6 Ma

The top of the *T. insigna/F. weaveri* Zone is defined by the LO of *T. insigna* in Sample 383-U1540D-15H-CC (159.51–159.56 m CSF-

A). Within the zone, the LOs of *F. weaveri* and *Thalassiosira inura* were noted in Samples 16H-4, 140 cm (165.39 m CSF-A) and 16H-CC (169.19–169.24 m CSF-A), respectively. After Zielinski and Gersonde (2002), the latter species is reported to occur close to the top of the *T. insigna/F. weaveri* Zone, exhibiting a discrepancy with the LO of *T. insigna* observed in Sample 15H-CC (159.51–159.56 m CSF-A). Thus, more detailed postcruise examination of diatom abundances in this zone is needed to determine the true upper zonation boundary. Furthermore, the FO of *S. tetraoestrupii* was identified in Sample 16H-CC (169.19–169.24 m CSF-A), the LO of *Thalassiosira striata* was noted in Sample 17H-CC (178.80–178.85 m CSF-A), and the LO of *Thalassiosira complicata* was encountered in Sample 19H-1, 140 cm (189.40 m CSF-A). The base of this zone is defined by the FO of *F. weaveri* in Sample 19H-2, 140 cm (190.91 m CSF-A).

Fragilariopsis interfrigidaria Partial Range Zone

Top: FO of *F. weaveri*
Base: FO of *Fragilariopsis interfrigidaria*
Age: 4.0–3.5 Ma

The top of the *F. interfrigidaria* Zone is defined by the FO of *F. weaveri* in Sample 383-U1540D-19H-2, 140 cm (190.91 m CSF-A). A variety of common to rare *Hemidiscus* species, few to rare *T. inura*, few *Thalassiothrix antarctica*, rare *T. complicata*, and rare *T. striata* were observed in this zone. Furthermore, the LO of *Fragilariopsis arcula* was noted in Sample 19H-4, 140 cm (193.95 m CSF-A). The base of the *F. interfrigidaria* Zone is defined by the FO of *F. interfrigidaria* in Sample 19H-5, 140 cm (195.47 m CSF-A). In the same sample, the LOs of *Fragilariopsis clementia, Fragilariopsis aurica*, and *Fragilariopsis praecurta* were observed.

Fragilariopsis barronii Partial Range Zone

Top: FO of *F. interfrigidaria*
Base: LO of *F. barronii*
Age: 4.5–4.0 Ma

The top of this zone is defined by the FO of *F. interfrigidaria* in Sample 383-U1540D-19H-5, 140 cm (195.47 m CSF-A). Common *F. arcula*, few *H. cuneiformis* and *F. praecurta*, and rare *F. aurica* and *T. complicata* were found in this zone. The FO of *T. striata* was noted in Sample 19H-CC (197.99–198.04 m CSF-A). The base of the zone is defined by the FO of *F. barronii* in Sample 19H-CC (197.99–198.04 m CSF-A).

Thalassiosira inura Partial Range Zone

Top: FO of *F. barronii*
Base: FO of *T. inura*
Age: 4.9–4.5 Ma

The diatom assemblage in the *T. inura* Zone is dominated by early Pliocene species but also includes reworked Miocene taxa, mainly of the genus *Denticulopsis*. The top of the zone is defined by the FO of *F. barronii* in Sample 383-U1540D-19H-CC (197.99–198.04 m CSF-A). The diverse Pliocene assemblage within the zone consists of common to rare *F. arcula*, *F. aurica*, *F. clementia*, *F. fossilis*, *F. praecurta*, *T. complicata*, *T. inura*, *Fragilariopsis reinholdii*, *Proboscia* spp., and several subspecies of *T. nitzschioides*. Sample 383-U1540E-10H-CC contains common occurrences of *T. nitzschioides* var. *parva*; this high abundance points to the warmest SSTs of all diatom assemblages inspected for Site U1540 (Esper and Gersonde, 2014) based on the a modern temperature range of 12°–18°C for *T. nitzschioides* var. *parva* in the northern ACC region.

Radiolarians

Samples from Cores 383-U1540A-1H through 16H and 383-U1540D-13H through 22H were processed and analyzed for radiolarian abundance and preservation. Two additional samples from Hole U1540E (383-U1540E-9H-CC and 10H-CC) were analyzed to better refine the stratigraphy of the lower portion of the site. Sample 383-U1540A-1H-CC (8.88–8.93 m CSF-A) contains few radiolarians with moderate preservation. Radiolarians are moderately to well preserved and abundant in the upper ~178.80 m at Site U1540 (Samples 383-U1540A-2H-CC through 16H-CC [18.72–151.02 m CSF-A]), except for Sample 13H-CC (121.83–121.88 m CSF-A), where they are few and moderately to poorly preserved, and Samples 383-U1540D-13H-CC through 17H-CC (140.94–178.85 m CSF-A). In Core 18H through Section 22H-1 (188.30–210.50 m CSF-A) and Samples 383-U1540E-9H-CC through 10H-CC (204.01–213.34 m CSF-A), radiolarian abundance and preservation decrease significantly. Radiolarians are common to barren, and preservation varies between moderate and poor in this interval (Figures **F19**, **F20**; Table **T5**). Recognized radiolarian biostratigraphic events are shown alongside diatom, calcareous nannofossils, and planktonic foraminifers in Table **T3**. A plate illustrating some of the taxa identified at this site is shown in Figure **F21**.

In Hole U1540A, eight radiolarian events were recognized and used for dating the drilled sequence. The boundary of the Omega and Psi Zones was recognized in Sample 383-U1540A-2H-CC (18.72–18.77 m CSF-A) by the LO of *Stylatractus universus*, indicating an age younger than 0.43 Ma. The last appearance of *Antarctissa cylindrica* (0.64 Ma), which falls within the Psi Zone, occurs in Sample 4H-CC (37.89–37.94 m CSF-A). Several well-preserved radiolarians occur in this interval, and the presence of phaeodarians suggests very favorable conditions for radiolarian preservation because this group is easily dissolved in marine sediments (Takahashi and Anderson, 2002). The boundary of the Psi and Chi Zones (0.86 Ma) was recognized in Sample 7H-CC (64.75–64.80 m CSF-A) by the presence of *Pterocanium charybdeum trilobum*.

Table T5. Distribution chart of radiolarians, Holes U1540A, U1540D, and U1540E. **Download table in CSV format.**

Two events were observed in Sample 383-U1540A-12H-CC (112.49–112.54 m CSF-A): the top of *Cycladophora pliocenica* (1.81 Ma), which divides the Chi Zone into two subzones, and the bottom of *Triceraspyris antarctica* (1.88 Ma). The base of the Chi Zone was placed in Sample 13H-CC (121.83–121.88 m CSF-A) by the presence of *Eucyrtidium calvertense* (1.92 Ma). The boundary of the Phi and Upsilon Zones was recognized by the LO of *Helotholus vema* (2.40 Ma) in Sample 15H-CC (141.08–141.13 m CSF-A). The last appearance datum (LAD) of *H. vema* usually slightly predates the LAD of *Desmospyris spongiosa* (2.48 Ma), which occurs in Sample 16H-CC (150.97–151.02 m CSF-A).

In Hole U1540D, the LAD of *H. vema* (2.40 Ma) was recognized in Sample 383-U1540D-15H-CC (159.51–159.56 m CSF-A), marking the top of the Upsilon Zone. The co-occurrence of *H. vema*, *D. spongiosa*, and *Cycladophora davisiana* in Sample 17H-CC (178.80–178.85 m CSF-A) suggests an age of 2.48–2.61 Ma, placing this sample in the upper Upsilon Zone. The lower part of the Upsilon Zone (3.48–4.59 Ma) was placed in Sample 19H-CC (197.99–198.04 m CSF-A) based on the co-occurrence of *Prunopyle titan* and *H. vema*. The base of the Upsilon Zone was recognized in Sample 20H-CC (206.65–206.71 m CSF-A) by the absence of *H. vema*. Sample 21H-CC (210.35–210.40 m CSF-A) contains only traces of radiolarians. Sections 383-U1540D-22H-1 (210.45–210.50 m CSF-A) and 383-U1540E-9H-CC and 10H-CC (204.01–213.34 m CSF-A) contain few to rare poorly preserved radiolarians. No further biostratigraphical analyses were performed in this interval due to the scarcity of radiolarians. Reworked Miocene radiolarian species (*Cyrtocapsella* spp. and *Ommatartus antepenultimus*) were also observed in this interval.

Silicoflagellates

Silicoflagellates were analyzed from 16 core catcher samples and 1 split-core sample from Hole U1540A; 1 mudline, 2 core catcher, and 2 split-core samples from Hole U1540B; 10 core catcher samples from Hole U1540D; and 1 core catcher sample from Hole U1540E. Silicoflagellates are present throughout the entire succession except in two samples that are barren (Table **T6**). They range from rare to common in most samples, and are abundant in a few samples (Figures **F19**, **F20**).

The silicoflagellate assemblage at Site U1540 consists of 10 species (Figure **F22**). *Bachmannocena diodon*, *Dictyocha stapedia*, *Dictyocha aculeata*, *Dictyocha perlaevis*, *Dictyocha brevispina*, *Dictyocha aspera*, *Stephanocha speculum*, *Stephanocha boliviensis*, *Octactis pulchra* and *Octactis* sp. are present in samples from the mudline and the upper few meters (e.g., Sample 383-U1540A-1H-CC).

S. speculum is present in all the studied samples and has high morphological variability, including specimens with long and short corner spines, specimens with variable apical ring features (*S. speculum* var. *monospicata*, *S. speculum* var. *bispicata*, *S. speculum* var. *coronata*, *S. speculum* var. *binocula*, and *S. speculum* var. *pseudofibula*), and specimens with different numbers of basal ring sides (*S. speculum* var. *pentagona*, *S. speculum* var. *septenaria*, *S. speculum* var. *octonaria*, *S. speculum* var. *nonarius*, and a large [≥30 μm] variety similar to the *S. speculum* Group B described by Tsutsui et al. [2009] from water samples). Rare larger specimens (>40 μm) in the lower portions of the core (Samples 383-U1540D-17H-CC and 383-U1540E-9H-CC) are assigned to *S. boliviensis*.

Figure F21. Radiolarians, Holes U1540A and U1540D. Scale bars = 100 µm. 1–4, 7, 15. 383-U1540A-5H-CC. (1–4) Phaeodarians. 5, 10–14, 16. 383-U1540A-2H-CC. (5) *Spongoplegma antarcticum*. 6, 9. 383-U1540A-3H-CC. (6) *Stylatractus universus*. (7) *Spongotrochus glacialis*. 8. *Saturnalis circularis* (383-U1540A-7H-CC). (9) *Phorticium clevei*. (10–12) *Cycladophora davisiana*. (13) *Botryostrobus auritus*. (14) *Antarctissa denticulata*. (15) *Antarctissa cylindrica*. (16) *Antarctissa strelkovi*. 17. *Helotholus vema* (383-U1540D-16H-CC). 18. *Cycladophora pliocenica* (383-U1540A-13H-CC). 19, 20. *Eucyrtidium calvertense* (383-U1540A-14H-CC).
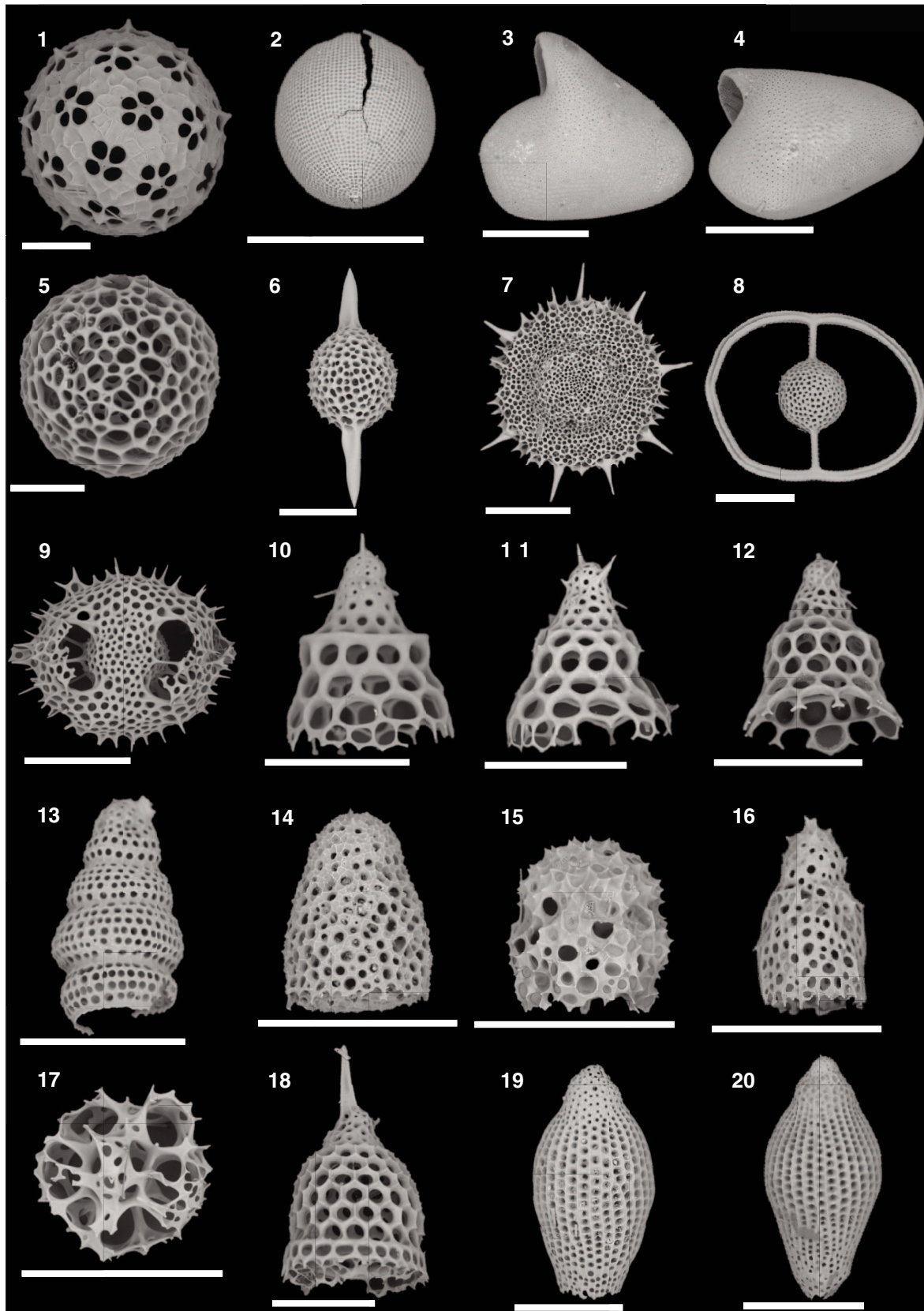
Table T6. Distribution chart of silicoflagellates, Holes U1540A, U1540B, U1540D, and U1540E. **Download table in CSV format.**

Figure F22. Silicoflagellates, Site U1540. Focus on basal ring (upper images) and apical ring (lower images). Light microscope. (1) *Stephanocha speculum* var. *speculum* small form. (2) *S. speculum* var. *monospicata*. (3) *S. speculum* var. *coronata*. (4) *S. speculum* var. *pentagona*. (5) *S. speculum* var. *monospicata*, large variety. (6) *S. speculum* var. *octonaria*. (7) *S. speculum* var. *binocula*. (8) *Stephanocha boliviensis*. (9) *Octactis* sp. (new species). (10) *Octactis pulchra* (10-sided form). (11) *O. pulchra*. (12) *Dictyocha aspera* var. *pygmaea*. (13) *Dictyocha stapedia*. (14) *Dictyocha aculeata*. (15) *Dictyocha brevispina*. (16) *Dictyocha perlaevis*. (17) *D. perlaevis* pinched form. (18) *Bachmannocena diodon* var. *nodosa*.
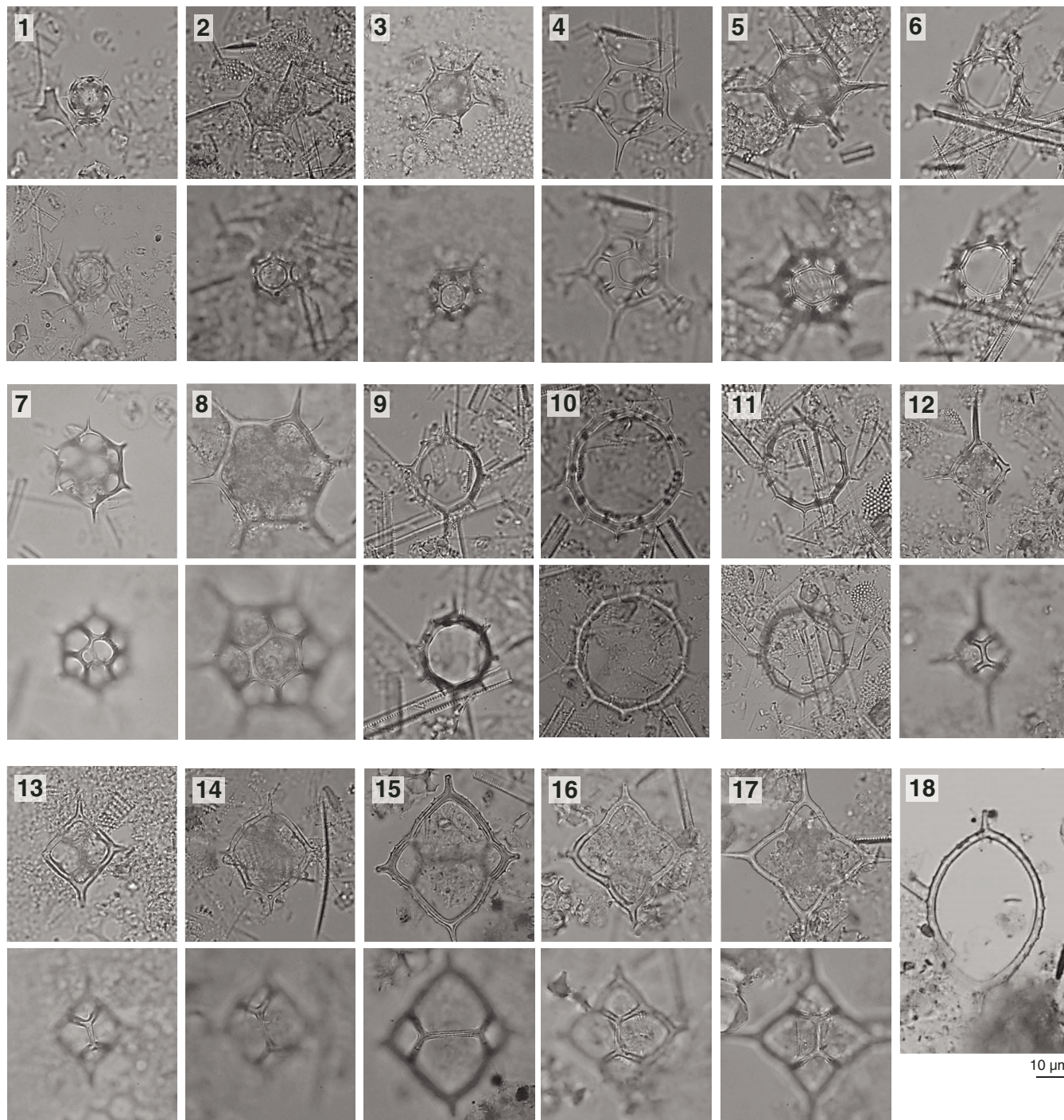
O. pulchra is present at an abundance of rare to few in most samples between Samples 383-U1540A-7H-CC and 11H-CC (64.75–103.02 m CSF-A). An undescribed species of *Octactis* characterized by an eight-sided basal ring lacking pikes and a thick, wide apical ring is common in Sample 13H-CC (121.83–121.88 m CSF-A).

S. speculum occurs with both long- and short-spined forms throughout the core, so it was not possible to separate *S. speculum* Zones A and B, as developed for the Southern Ocean (Ciesielski, 1975) and tied to diatom biozones and paleomagnetic stratigraphy (Ciesielski and Weaver, 1983) spanning the entire Pleistocene. Changes in abundance of the different *S. speculum* varieties testify to different climatic cycles; complex morphologies with multiple sides and complex apical structures increase in cold periods. The presence of *Dictyocha* species and *O. pulchra* in some intervals is conversely indicative of warmer SSTs.

The occurrence of *S. boliviensis* in Sample 383-U1540D-17H-CC indicates the *S. boliviensis* Zone (Ciesielski, 1975), even though the species is rare. A warm-water assemblage constituted by *D. aspera* var. *aspera*, *D. aspera* var. *pygmaea*, and *D. perlaevis* typically characterizes the lowermost samples at this site (383-U1540D-20H-CC and 383-U1540E-9H-CC). *D. brevispina* and *M. diodon*, typical upper Miocene–lower Pliocene species, also occur in the lowermost samples.

Calcareous nannofossils

Calcareous nannofossil biostratigraphy is based on the analysis of 111 samples: 1 mudline, 16 core catcher, and 42 split-core samples from Hole U1540A; 1 mudline, 2 core catcher, and 5 split-core samples from Hole U1540B; 1 mudline, 9 core catcher, and 18 split-core samples from Hole U1540D (149.94–201.45 m CSF-A); and 2 core catcher and 15 split-core samples from Hole U1540E (196.77–213 m CSF-A).

In general, nannofossils are rare to abundant throughout the sequence. They become dominant in discrete intervals and form nannofossil oozes, as in Samples 383-U1540A-1H-2, 83 cm (2.34 m CSF-A); 1H-CC (8.88–8.93 m CSF-A); 2H-3, 114 cm (13.15 m CSF-A); 4H-2, 85 cm (30.35 m CSF-A); 10H-CC (93.77–93.82 m CSF-A); 12H-4, 63 cm (108.2 m CSF-A); and 16H-1, 75 cm (122.25 m CSF-A) and Samples 383-U1540D-17H-6, 63 cm (177.07 m CSF-A); 17H-CC (178.8–178.85 m CSF-A); and 18H-3, 15 cm (181.58 m CSF-A). These oozes are almost monospecific, but the dominant taxa vary along the sequence (*Gephyrocapsa* spp., *Reticulofenestra* spp., or *Coccolithus pelagicus*) (Figure **F23**). The preservation of calcareous nannofossils varies widely (from poor to good), which makes the recognition of some of the species markers (e.g., *Emiliania huxleyi*) difficult (Figure **F24**). In contrast, well-preserved whole coccospheres were found in ooze-bearing sediments.

The nannofossil assemblage at Site U1540 consists of 29 groups/taxa, including *E. huxleyi*, *Gephyrocapsa margerelii*/*muellerae*, *Gephyrocapsa caribbeanica*, *Gephyrocapsa oceanica*, *Gephyrocapsa* spp. (<4 μm, closed >4 μm, medium, and large), *Gephyrocapsa omega*, *Pseudoemiliania lacunosa*, *Reticulofenestra* (<3, 3–5, 5–7, and >7 μm), *Reticulofenestra asanoi*, *Reticulofenestra pseudoumbilicus*, *Dictyoccocites* spp., *C. pelagicus*, *Calcidiscus leptoporus*, *Calcidiscus macintyrei*, *Oolithotus* spp., *Helicosphaera carteri*, *Helicosphaera sellii*, *Pontosphaera multipora*, *Scyphosphaera* spp. (including *Scyphosphaera ventriosa*), *Discoaster* spp., *Discoaster brouweri*, *Discoaster variabilis*, and *Amaurolithus primus*. Rare reworked specimens were found throughout the cores, especially in Samples from Core 383-U1540D-20H (Table **T7**); these include *Dictyoccocites* spp., *Discoaster* spp., and *A. primus*.

In total, 10 biostratigraphic events were observed at Site U1540. Nannofossil Zones CN15/NN21 to CN11b/NN15 were recognized (Figure **F17**) based on the FO of *E. huxleyi* (Sample 383-U1540A-1H-4, 133 cm; 5.85 m CSF-A), the LO of *P. lacunosa* (Sample 2H-2, 177 cm; 11.67 m CSF-A), the LO of *R. asanoi* (Sample 4H-2, 85 cm; 30.35 m CSF-A), the FCO of *R. asanoi* (Sample 7H-CC; 64.75–64.8 m CSF-A), the LO of *Gephyrocapsa* spp. large (>5.5 μm) (Sample 8H-3, 142 cm; 70.72 m CSF-A), the LO of *H. sellii* (Sample 8H-CC; 74.50–74.55 m CSF-A), the FO of *Gephyrocapsa* spp. large (>5.5 μm) (Sample 9H-CC; 83.90–83.95 m CSF-A), the LO of *C. macintyrei* (Sample 12H-2, 70 cm; 105 m CSF-A), the LO of *R. pseudoumbilicus* (Sample 383-U1540D-19H-2, 131 cm; 190.82 m CSF-A), and the LO of *A. primus* (Samples 383-U1540D-20H-1, 90 cm [198.4 m CSF-A], and 383-U1540E-9H-7, 38 cm [203.45 m CSF-A]). Additionally, the rare occurrences of *G. omega* in Sample 383-U1540A-4H-CC (37.89–37.94 m CSF-A) and *S. ventriosa* in Sample 19H-6, 29 cm (195.87 m CSF-A), provide additional good age control for the Pliocene–Pleistocene sequence.

Foraminifers

Planktonic foraminifers

At Site U1540, core catcher samples from all 16 cores of Hole U1540A, Cores 383-U1540B-1H and 19H, and Cores 383-U1540E-13H through 22H were analyzed for planktonic foraminifers (Table **T8**). Abundance of foraminifers relative to the total >150 μm sieved and dried sediment fraction varies throughout Holes U1540A, U1540B, and U1540D, with foraminifers making up 5%–30% of the total coarse fraction residue (Figures **F19**, **F20**). Abundance is particularly high in Samples 383-U1540A-1H-CC, 2H-CC, 4H-CC, 5H-CC, 12H-CC, 13H-CC, and 15H-CC; 383-U1540B-1H-CC; and 383-U1540D-19H-CC.

Assemblages are mainly characterized by high-latitude and some temperate species. *Neogloboquadrina pachyderma* (sinistral) dominates the assemblage in the majority of samples, and *Globigerina bulloides*, *Truncorotalia crassaformis*, and *Globoconella inflata* frequently occur in lower abundance. *Globoconella puncticulata puncticuloides*, a subspecies of *Globoconella puncticulata* that persisted in the western South Pacific long after the global extinction of *G. puncticulata* (Hornibrook, 1981; Hornibrook and Jenkins, 1994; Scott et al., 2007), occurs regularly in Samples 383-U1540A-3H-CC through 16H-CC and Sample 383-U1540D-13H-CC through Section 22H-1. Occasionally, species such as *G. puncticulata*, *Globigerina falconensis*, *Orbulina universa*, *Neogloboquadrina incompta*, *Truncorotalia truncatulinoides*, *Globoturborotalita woodi*, *Truncorotalia imbricata*, *Truncorotalia crassula*, *Truncorotalia ronda*, *Truncorotalia hessi*, *Hirsutella margaritae*, *Globigerinita glutinata*, and *Hirsutella scitula* were found. Examples of major foraminiferal taxa found at Site U1540 are shown in Figure **F25**.

Nine biomarker species are present in Site U1540 planktonic foraminiferal assemblages: *G. inflata*, *T. imbricata*, *T. ronda*, *T. hessi*, *T. truncatulinoides*, *G. woodi*, *G. puncticulata*, *G. puncticulata puncticuloides* and *H. margaritae*. The uppermost part of Hole U1540A is late Pleistocene in age based on the presence of *T. imbricata* (0.6 Ma; Bylinskaya, 2004) and *T. hessi* (~0.75 Ma; Gradstein et al., 2012) in Samples 383-U1540A-1H-CC through 4H-CC (8.88–37.94 m CSF-A). *G. inflata* was found throughout the sequence in Hole U1540A, and *G. puncticulata puncticuloides* is abundant in Samples 3H-CC through 16H-CC (28.56–151.02 m CSF-A), dating this interval to between 0.7 and 2.39–3.13 Ma (Wei, 1994). *T. truncatulinoides* was found in Sample 383-U1540B-1H-CC (3.07–3.12 m CSF-A), which indicates Zone SN14 of Jenkins (1993). Sections 383-U1540D-13H-

Figure F23. Scanning electron microscope images of (1–5) extant coccolithophores (plankton samples retrieved at 55°8.46′S, 114°50.45′W) and recent calcareous nannofossils from (6–15) mudline samples and (15–24) sediment samples, Holes U1540B and U1540D. Scale bars = 5 µm. 1. Coccosphere of *Calcidiscus leptoporus*. 2. Detached coccolith of *Coccolithus pelagicus*. 3, 4. Coccospheres of *Emiliania huxleyi* type O. 5. *Syracosphaera dilatata*. 6. *C. leptoporus* (Hole U1540B). 7. *Helicosphaera carteri*. 8. *C. pelagicus* (Hole U1540D). 9–11. *E. huxleyi* type O (Hole U1540B). 12. *E. huxleyi* type A (Hole U1540D). 13. *Gephyrocapsa* small (<4 µm). 14, 15. *Gephyrocapsa oceanica* (14) Hole U1540D, (15) Hole U1540B. 16. *C. leptoporus* (383-U1540D-17H-CC). 17–19. 383-U1540B-1H-2, 133 cm. (17) *C. pelagicus*. (18) *E. huxleyi*. (19) Two placoliths of *Gephyrocapsa muellerae*. 20. *Reticulofenestra* 3–5 µm/*Reticulofenestra producta* (top: 383-U1540D-17H-CC; bottom: 383-U1540B-20H-4, 86 cm). 21–23. 383-U1540B-20H-4, 86 cm. (21) *Reticulofenestra* 5–7 µm. (22) *Reticulofenestra pseudoumbilicus*. (23) *Dictyococcites* spp./*Reticulofenestra* 5–7 µm with closed central area. 24. Small-sized *Dictyococcites* spp.
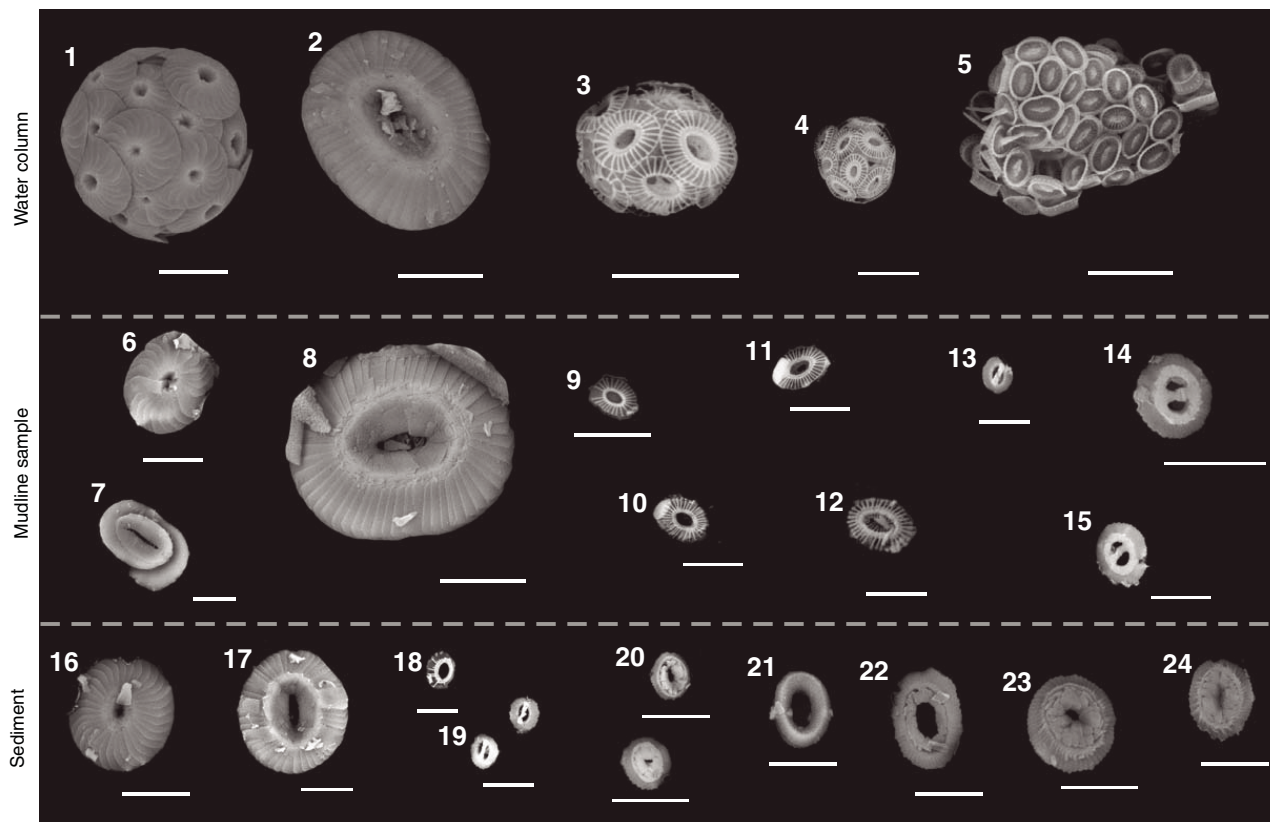
CC through 22H-1 (140.94–210.50 m CSF-A) were analyzed to include depths not recovered in Hole U1540A. *G. puncticulata puncticuloides* is relatively abundant in all analyzed samples, suggesting ages older than 0.7 Ma for this interval (Hornibrook, 1981; Hornibrook and Jenkins, 1994; Scott et al., 2007). *T. ronda* is found frequently in Samples 383-U1540D-13H-CC through 21H-CC, indicating that this interval comprises the upper Quaternary (~0.6 Ma) to mid-lower Pliocene (Bylinskaya, 2004). *G. woodi* was observed in Sample 17H-CC, indicating an age older than 2.3 Ma, but it was absent in other samples from Hole U1540D, which suggests that it occurs only sporadically in the higher latitudes, so its FO at Site U1540 might not match the global LAD. *G. puncticulata* is present in Sections 19H-CC through 22H-1 (197.99–210.50 m CSF-A), indicating ages older than 2.35 Ma for this interval. We also found sporadic and poorly preserved specimens of *H. margaritae* in the same interval, which indicates that the interval is older than 3.85 Ma. In Section 22H-1, we found *T. truncatulinoides* mixed with species that indicate older zones (i.e., *G. puncticulata*). It is therefore possible that some material from the upper part of the core was mixed with material from the bottom during coring, resulting in this mixed assemblage in the sample. Planktonic foraminiferal age estimates are consistent with radiolarian, diatom, and nannofossil ages.

Preservation state was generally moderate in Holes U1540A, U1540B, and U1540D; Samples 383-U1540D-18H-CC and 22H-CC in particular exhibit poor preservation and high fragmentation (Table **T8**). Preservation was better in Samples 383-U1540A-1H-CC, 4H-CC, and 383-U1540B-1H-CC. Many encrusted forms of *N. pachyderma*, *G. inflata*, *G. puncticulata puncticuloides*, and *T. crassaformis* were found, which may influence stable isotope or trace element analyses (Jonkers et al., 2012; Steinhardt et al., 2015).

Benthic foraminifers

Benthic foraminifers were examined in core catcher samples from Holes U1540A (16 samples), U1540B (2 samples), and U1540D (10 samples). Samples with an average volume of ~20 cm³ were processed from all core catchers to obtain quantitative estimates of benthic foraminiferal distribution patterns downhole. The mudline sample from Hole U1540B was also examined, although systematic assemblage data were not collected. To assess assemblage composition and variability in core catcher samples, ~100 specimens from the >125 µm fraction were picked and transferred to slides for identification and counting. The presence and distribution of benthic foraminifers was additionally checked in the 125–63 µm fraction to ensure that assemblages in the >125 µm fraction were representative and that small species such as phytodetritus feeders or small infaunal taxa were not overlooked.

The abundance of benthic foraminifers is generally very low except in a few samples. Benthic foraminifers are moderately pre-

Figure F24. Calcareous nannofossils, Holes U1540A and U1540D. Light microscope. Scale bar = 5 µm. 1, 2. *Emiliania huxleyi* (Hole U1540D mudline). 3, 4. *Pseudoemiliania lacunosa* (3) 383-U1540A-9H-CC, (4) 4H-CC. 5. *Gephyrocapsa* small (<4 µm) (383-U1540A-4H-3, 28 cm). 6, 7. *Helicosphaera sellii*, (6) 383-U1540A-13H-4, 112 cm, (7) 8H-CC. 8. *Gephyrocapsa* large (>5.5 µm) (383-U1540A-8H-CC). 9. *Calcidiscus macintyrei* (383-U1540A-12H-6, 112 cm). 10. *Reticulofenestra minutula* (383-U1540D-16H-CC). 11. *Reticulofenestra* small (<3 µm) (383-U1540D-17H-CC). 12. *Reticulofenestra pseudoumbilica* (383-U1540D-19H-CC). 13, 14. *Amaurolithus primus*, (13) 383-U1540D-20H-6, 68 cm, (14) 20H-4, 86 cm. 15. *Discoaster brouweri* (383-U1540D-20H-2, 115 cm). 16. *Discoaster variabilis/decorus* (383-U1540D-20H-2, 44 cm). 17, 18. *Scyphosphaera* spp. (383-U1540D-19H-6, 29 cm).
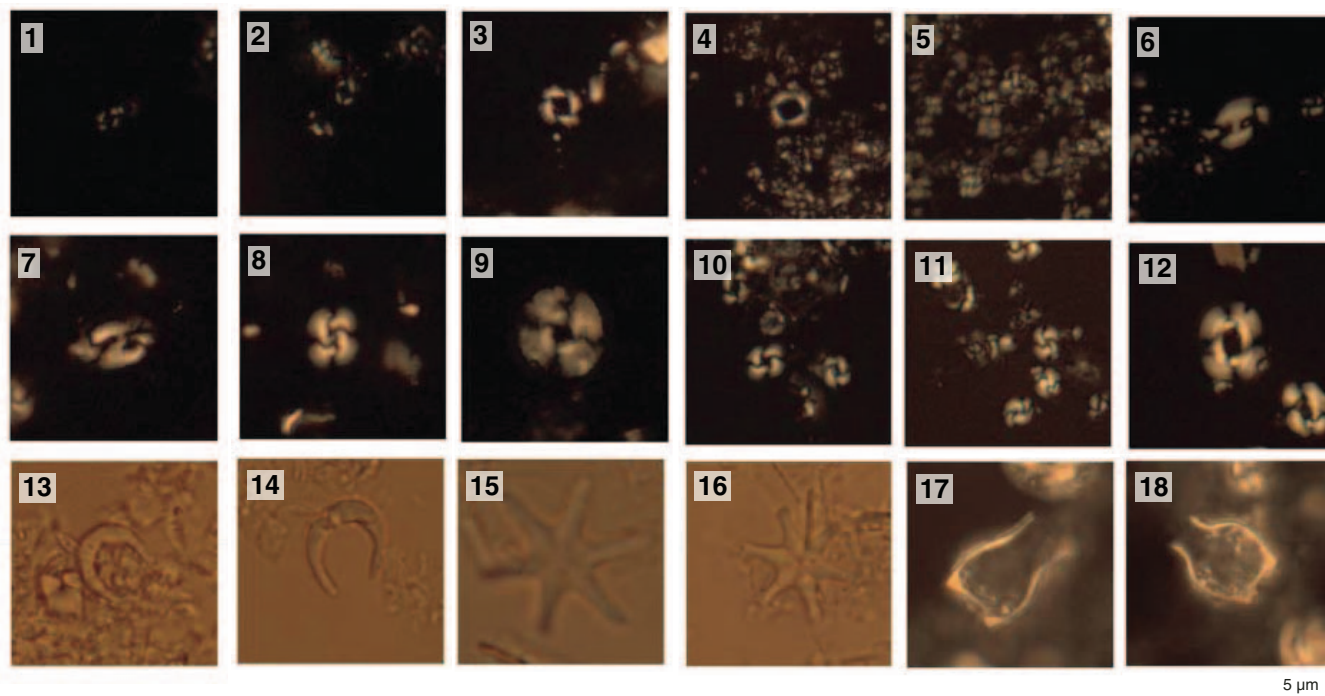

Table T7. Distribution chart of calcareous nannofossils, Holes U1540A, U1540B, U1540D, and U1540E. **Download table in CSV format.**

Table T8. Distribution chart of planktonic foraminifers, Holes U1540A, U1540B, and U1540D. **Download table in CSV format.**

served in Hole U1540A (upper part of sequence) and very poorly preserved in Hole U1540D (lower part of the sequence) (Figures **F19**, **F20**; Table **T9**). Samples 383-U1540A-8H-CC (74.50–74.55 m CSF-A), 383-U1540D-21H-CC (210.35-210.40 m CSF-A), and 22H-1 (210.45–210.50 m CSF-A) contain very few benthic foraminifers (Figures **F19**, **F20**).

A total of 76 benthic foraminiferal taxa were identified at this site. Table **T9** summarizes the downcore distribution of benthic foraminifers in core catcher samples from Holes U1540A, U1540B, and U1540D. Figure **F26** presents characteristic taxa found at this site, which are also illustrated in Figures **F27** and **F28**.

The overall composition of assemblages indicates abyssal depth throughout the early Pliocene to Holocene, and that the site remained above the carbonate compensation depth throughout this time. Species commonly recorded through the succession include the calcareous species *Epistominella exigua*, *Globocassidulina subglobosa*, *Melonis barleeanum*, *N. umbonifera*, *Oridorsalis umbonatus*, and *Pullenia bulloides* and the agglutinated species *Martinottiella communis*. These taxa assemblages suggest varying oxygen conditions, low to intermediate carbon flux, cold deep water with occasionally strongly pulsed food supply and oligotrophic conditions (Gupta et al., 2004; Singh and Gupta, 2004, 2010; Singh et al., 2012; Verma et al., 2013) above ~170 m CSF-A and warm, corrosive, low-oxygen bottom water conditions below that depth. The genus *Uvigerina* is abundant only in Samples 383-U1540A-1H-CC and 2H-CC, which also have high species diversity and may belong to the warm inter-

glacial intervals of the late Pleistocene. Abundant *Uvigerina* species are generally observed in areas of high surface productivity where organic carbon–rich sediments are deposited (Das et al., 2018; Schönfeld, 2006; Singh and Gupta, 2004), suggesting higher surface productivity at Site U1540 during these warm intervals. *Cibicidoides mundulus*, an abundant species at previous sites that suggests strongly pulsed cold water with low to intermediate organic flux, is abundant only in Samples 7H-CC and 8H-CC. *O. umbonatus*, *E. exigua*, *G. subglobosa*, and *P. bulloides* show episodic increases in abundance above ~170 m CSF-A.

Below ~170 m CSF-A, the diversity of benthic foraminifers increases and remains high except in the lowermost two samples (Sample 383-U1540D-21H-CC and the sample from Section 22H-1). None of the species discussed above are dominant, and *Uvigerina* has a sporadic presence. *N. umbonifera*, a species indicative of corrosive bottom water (Singh and Gupta, 2010; Bremer and Lohmann, 1982), is abundant. These conditions indicate the presence of warm corrosive bottom water at Site U1540 below ~170 m CSF-A. The number of species of agglutinated foraminifers also increases, and *M. communis* peaks in abundance. A higher number of fish teeth were also noticed in Samples 17H-CC through 21H-CC. Overall, the preservation of benthic foraminifers is very poor at this site, but even greater dissolution and secondary calcification were observed in Samples 17H-CC through 21H-CC.

The mudline samples from Holes U1540A and U1540B were soaked in rose bengal and ethanol solution and gently washed to

Figure F25. Common planktonic foraminifers, Site U1540. Scale bars = 100 µm. A. *Globigerina bulloides*. B. *Globigerinita glutinata*. C. *Globigerina woodi*. D–F. *Globoconella puncticulata puncticuloides* in (D) side, (E) umbilical, and (F) spiral view. G, H. *Globoconella puncticulata* in (G) umbilical and (H) side view. I. *Truncorotalia crassaformis ronda*. J–L. *T. crassaformis hessi* in (J) umbilical, (K) side, and (L) spiral view. M–O. *T. crassaformis imbricata* in (M) umbilical, (N) spiral, and (O) side view. P–R. *T. crassaformis* in (P) umbilical, (Q) side, and (R) spiral view. S, T. *Globoconella inflata* in (S) umbilical and (T) spiral view. U, V. *Neogloboquadrina pachyderma*. W. *Neogloboquadrina incompta*. X. *Hirsutella scitula*.
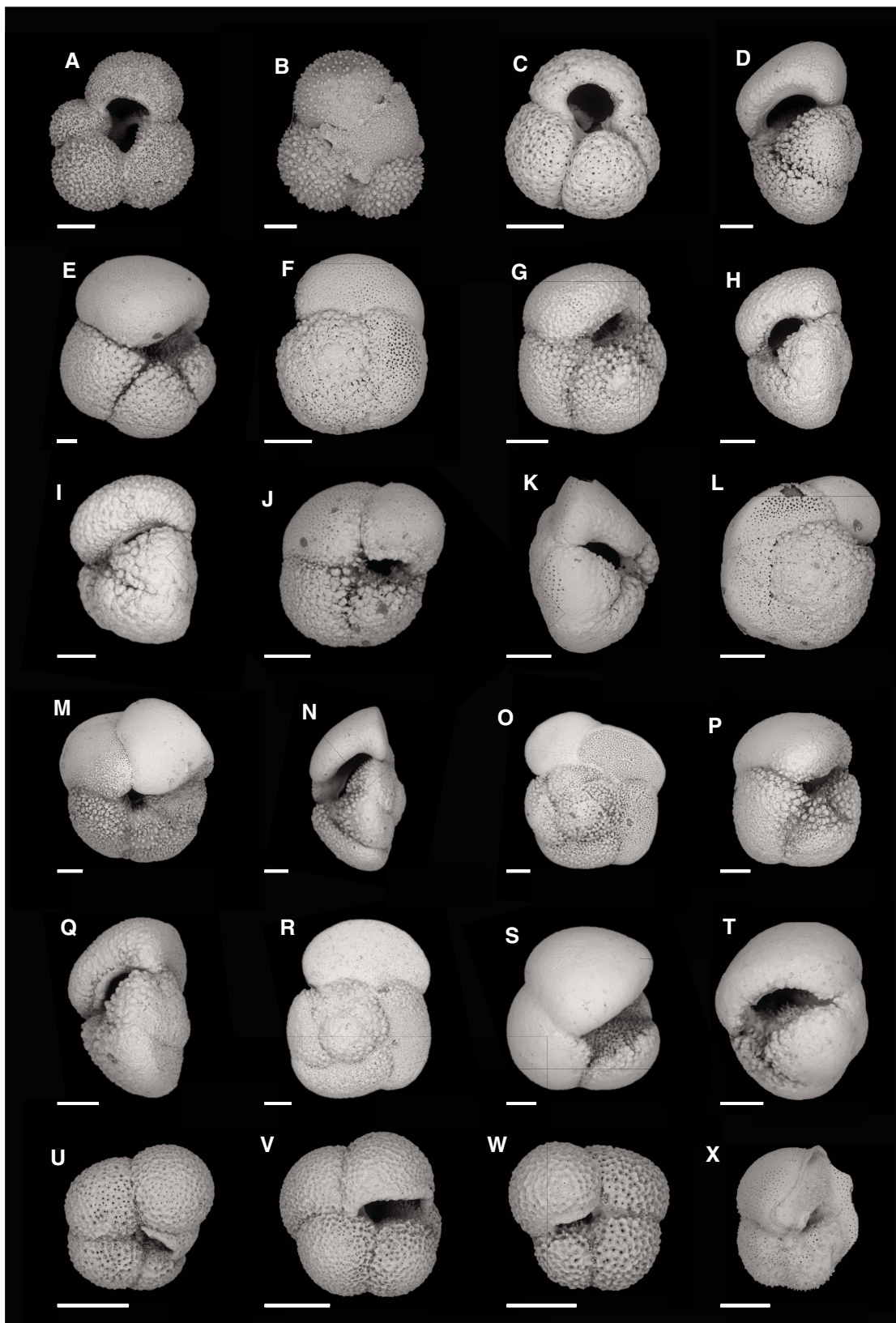
Table T9. Distribution chart of benthic foraminifers, Holes U1540A, U1540B, and U1540D. **Download table in CSV format.**

Figure F26. Species diversity index (H) and abundance of dominant species *Epistominella exigua, Globocassidulina subglobosa, Martinotiella communis, Melonis barleeanum, Pullenia bulloides*, and *Oridorsalis umbonatus*, Holes U1540A and U1540D. Gray field denotes an interval potentially influenced by warm corrosive bottom water.
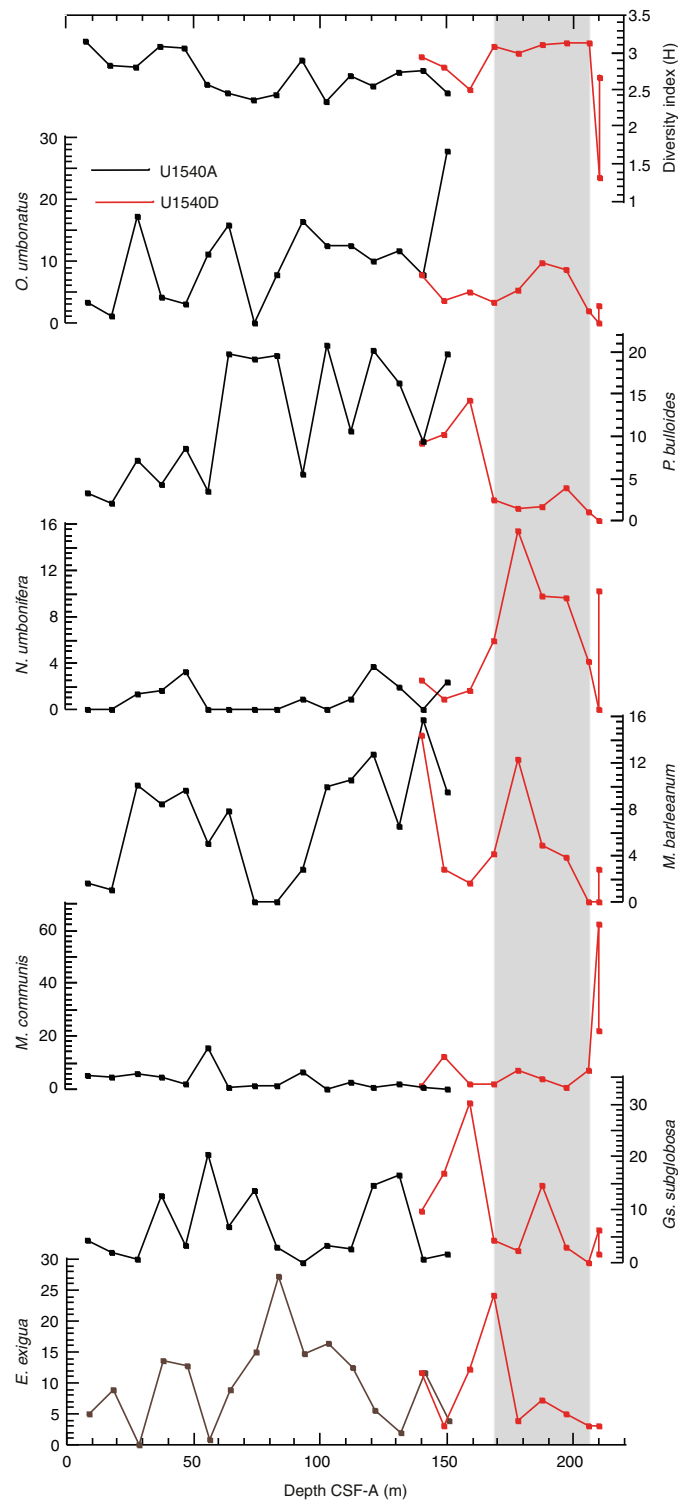
preserve fragile, agglutinated foraminifer specimens with extremely low fossilization potential. The mudline sample from Hole U1540B contains stained agglutinated and calcareous benthic foraminifers, whereas the mudline sample from Hole U1540A has no stained benthic foraminifers. This suggests that recent seafloor sediments were collected in the mudline sample from Hole U1540B but not in the mudline sample from Hole U1540A. The mudline sample from Hole U1540B is much more diverse in than the one from Hole U1539A, and it contains stained specimens of common and rare agglutinated species such as *Cribrostomoides subglobosus, Monalysidium politum, Astrorhiza* spp., *Rhabdammina* spp., *Reophax* sp., *Marsipella* sp., *Relosina* sp., *Rhizammina* sp., *Paratrochammina challengeri*, and *Ammobaculites* sp. The calcareous taxa are also very diverse and include *Astrononion stelligerum, C. mundulus, Dentalina* spp., *Eggerella bradyi, E. exigua, Fursenkoina complanata, Fissurina* spp., *Gyroidinoides* sp., *G. subglobosa, Lenticulina convergens, M. barleeanum, Pullenia quinqueloba, O. umbonatus, Quinqueloculina venusta, Quinqueloculina oblonga*, and *Triculina tricarinata*. A few additional species were found unstained. In both holes, the mudline samples are dominated by unstained planktonic foraminifers and radiolarians. Some mudline benthic foraminifer specimens are shown in Figures **F29** and **F30**.

Ostracods

Core catcher samples from Holes U1540A (383-U1540A-1H-CC through 16H-CC), U1540B (383-U1540B-1H-CC and 19H-CC), and U1540D (383-U1540B-13H-CC through 22H-CC) were scanned for the presence of ostracods during shipboard examination of benthic foraminifers. Ostracods occur in very low abundance at this site (≤14 valves per ~20 cm^3 sample), and about half of the samples were barren. Their preservation varies from good to very good. The highest ostracod abundance was observed in Samples 383-U1540A-1H-CC and 383-U1540B-1H-CC. The most common genus is *Henryhowella*, followed by *Krithe, Legitimocythere, Pennyella, Bradleya*, and *Poseidonamicus* as minor assemblage components. The assemblage comprises typical abyssal genera previously observed in the Pacific Ocean (Alvarez Zarikian, 2015; Stepanova and Lyle, 2014; Whatley et al., 1986; Yasuhara et al., 2013). Table **T10** summarizes the downcore distribution of ostracods present in core catcher samples from Holes U1540A, U1540B, and U1540D. Figures **F31** and **F32** show characteristic taxa found at this site. Figure **F31** also includes a single specimen of *Krithe* sp. B (plate C) found at Site U1539.

Figure F27. Benthic foraminifers, Holes U1540A, U1540B, and U1540D. Scale bars = 100 µm. 1, 2. *Fissurina striolata* (383-U1540A-1H-CC). 3. *Parafissurina* sp. (383-U1540A-2H-CC). 4–6, 21. 383-U1540A-4H-CC. (4) *Lagena* sp. (5, 6) *Lagena multilatera*. 7, 10, 13, 16, 18, 20. 383-U1540B-1H-CC. (7) *Fissurina formosa*. 8. *Lagena trigonomarginata* (383-U1540D-15H-CC). 9, 12. 383-U1540A-5H-CC. (9) *Lagena nebulosa*. (10) *Lagena sulcata*. 11. *Pyrulina cylindroides* (383-U1540A-2H-CC). (12) *Pyrulina angusta*. (13) *Uvigerina* sp. 14, 15, 16. 383-U1540A-1H-CC. (14, 16) *Uvigerina hispidocostata*. (15) *Uvigerina hispida*. 17. *Pyrgo* sp. (383-U1540D-20H-CC). (18) *Pyrgo murrhina*. (19) *Quinqueloculina oblonga*. (20) *Quinqueloculina venusta*. (21) *Ehrenbergina carinata*. 22. *Dentalina* sp. (383-U1540B-15H-CC). 23–25. 383-U1540D-18H-CC. (23, 24) *Cibicidoides bradyi*. (25) *Cibicides lobatulus*. 26. *Cibicidoides pachyderma* (383-U1540D-17H-CC). 27. *Glandulina ovula* (383-U1540B-19H-CC).
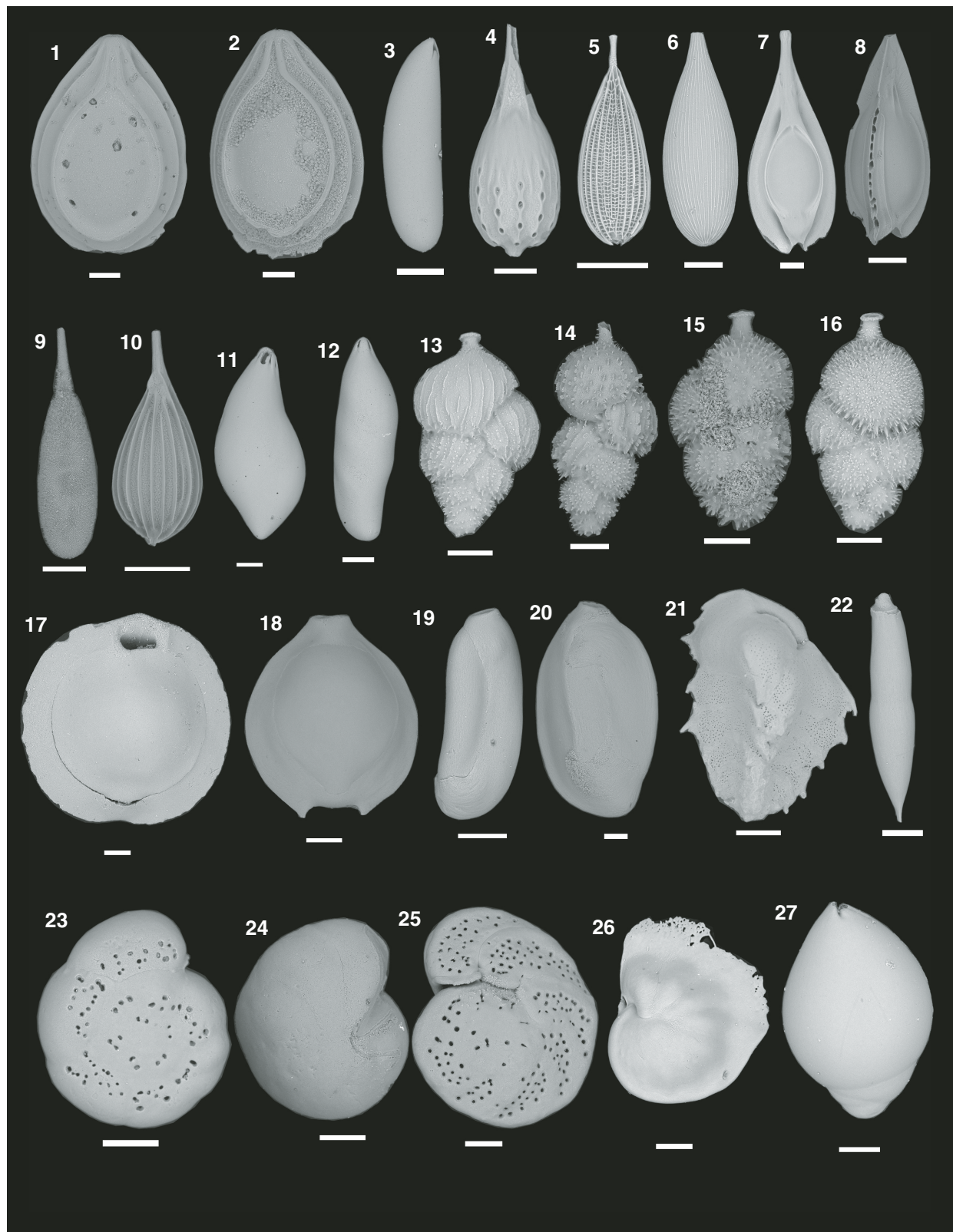
Figure F28. Benthic foraminifers, Holes U1540A, U1540B, and U1540D. Scale bars = 100 µm. (1) *Dentalina* sp. (383-U1540B-1H-CC). 2, 3. *Fursenkoina texturata* (383-U1540B-1H-CC). (4) *Stilostomella lepidula* (383-U1540B-1H-CC). 5. *Stilostomella abyssorum* (383-U1540D-17H-CC). 6, 7. *Orthomorphina* sp., (6) 383-U1540D-19H-CC, (7) 383-U1540D-16H-CC. 8. *Francuscia extensa* (383-U1540D-16H-CC). 9. *Pleurostomella* sp. (383-U1540D-17H-CC). 10. *Pyrulina angusta* (383-U1540B-1H-CC). 11–13. *Cyclammina* sp., (11) 383-U1540D-22H-CC, (12) 383-U1540D-19H-CC, (13) 383-U1540D-20H-CC. 14. *Haplophragmium* sp. (383-U1540D-22H-CC). 15. *Reophax* sp. (383-U1540D-22H-CC). 16. *Karreriella* sp. (383-U1540A-4H-CC). 17. *Haplophragmoides* sp. (383-U1540B-1H-CC). 18. *Discammina* sp. (383-U1540B-1H-CC). 19. *Discammina compressa* (383-U1540B-1H-CC). 20. *Siphotextularia* sp. (383-U1540A-15H-CC). 21. *Bolivina decussata* (383-U1540D-15H-CC). 22. *Amphicoryna hirsuta* (383-U1540B-1H-CC). 23 *Spirosigmoilina tenuis* (383-U1540D-19H-CC). 24 *Bolivina* sp. (383-U1540A-4H-CC).
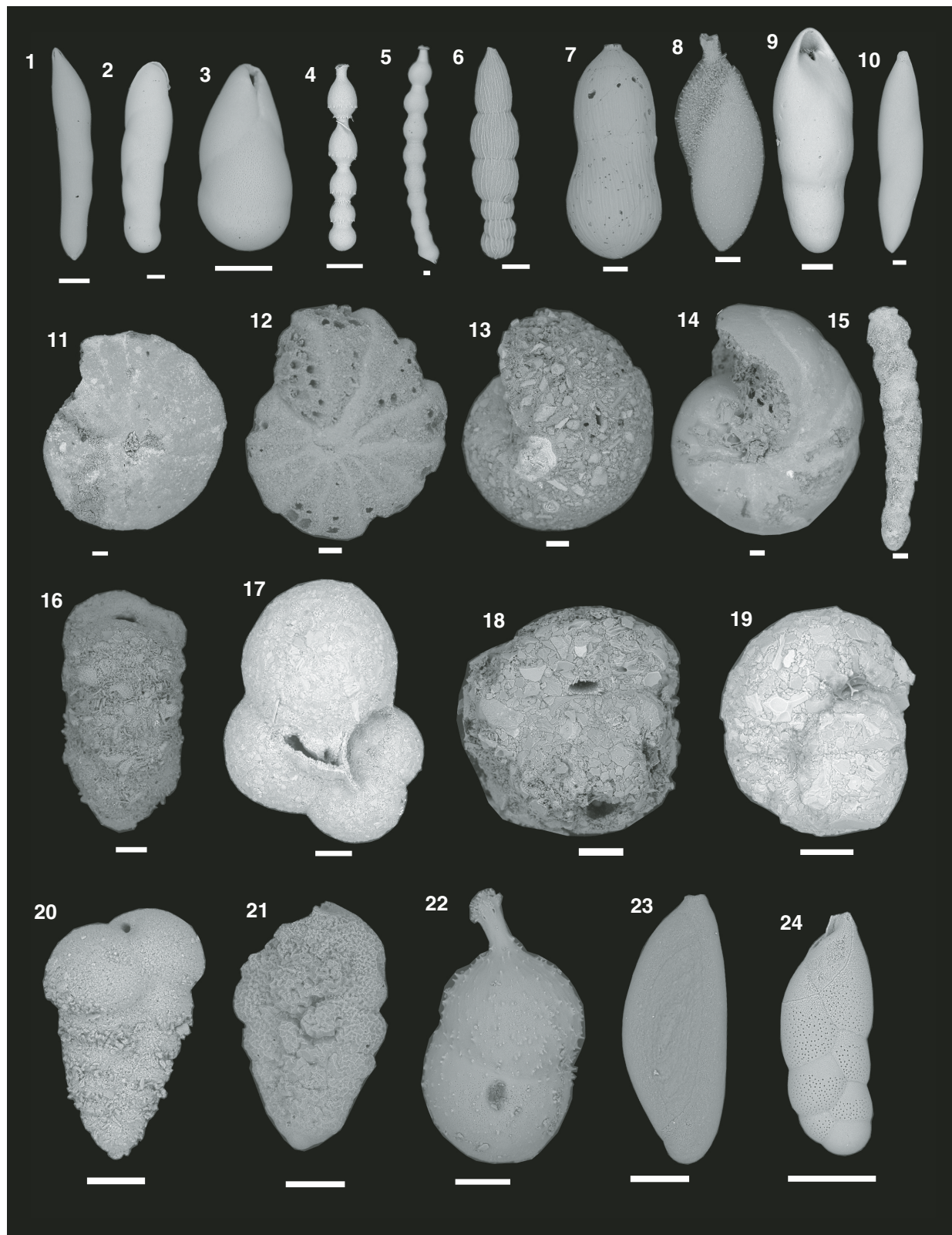
Figure F29. Benthic foraminifers in the mudline sample from Hole U1540B. A. *Rhabdammina* sp. that uses planktonic foraminifers of a single species (*Globoconella inflata*) in its construction. B. Stained calcareous benthic foraminifers. C. *Rhabdammina* sp. that uses planktonic small benthic and planktonic foraminifers species in its construction. D. *Rhabdammina* sp. that uses multiple planktonic foraminifers species in its construction. E. *Reophax* sp. F, G. Stained and unstained agglutinated benthic foraminifers. H. Unstained calcareous benthic foraminifers.
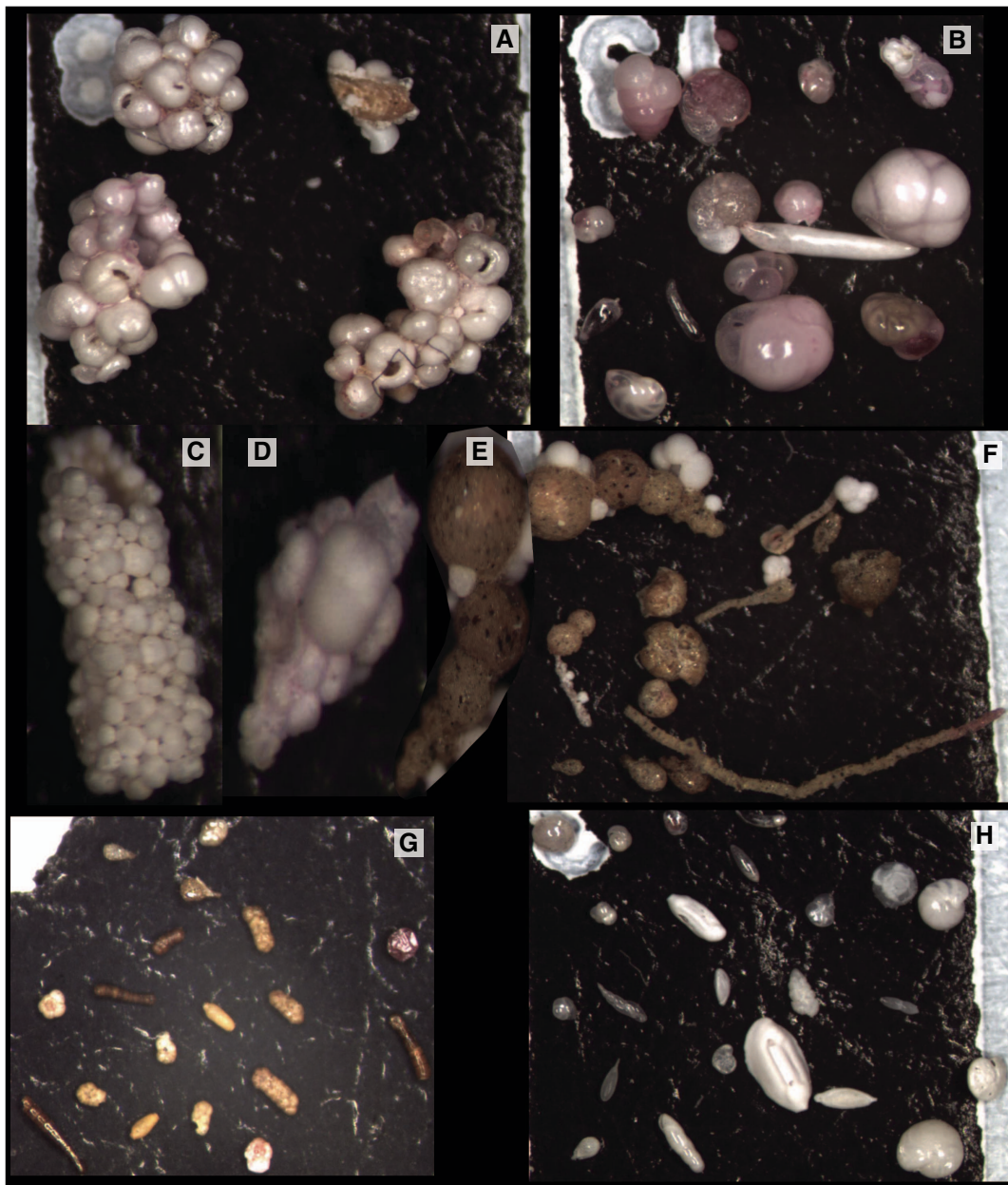
Figure F30. Agglutinated benthic foraminifers in mudline samples, Site U1540. Scale bars = 100 µm. 1. *Rhabdammina* sp. with planktonic foraminifers. 2. *Astrorhiza* sp. 3. *Hormosina globulifera*. 4. *Spiroplectammina biformis*. 5. *Reophax* sp. with planktonic foraminifer. 6. *Ammobaculites* sp. 7, 8. *Paratrochammina challengeri*. 9. *Cribrostomoides subglobosus*. 10. *Lagenammina* sp. 11. *Ammobaculites* sp. 12. *Cribrostomoides subglobosus* within *Ammobaculites* sp. 13. *Rhabdammina* sp. built up using smaller benthic and planktonic foraminifers of almost same size. 14. *Rhabdammina* sp. built up using smaller benthic and planktonic foraminifers of different sizes. 15. *Ammobaculites* sp. 16. *Rhabdammina* sp., built up using only *G. inflata* species test.
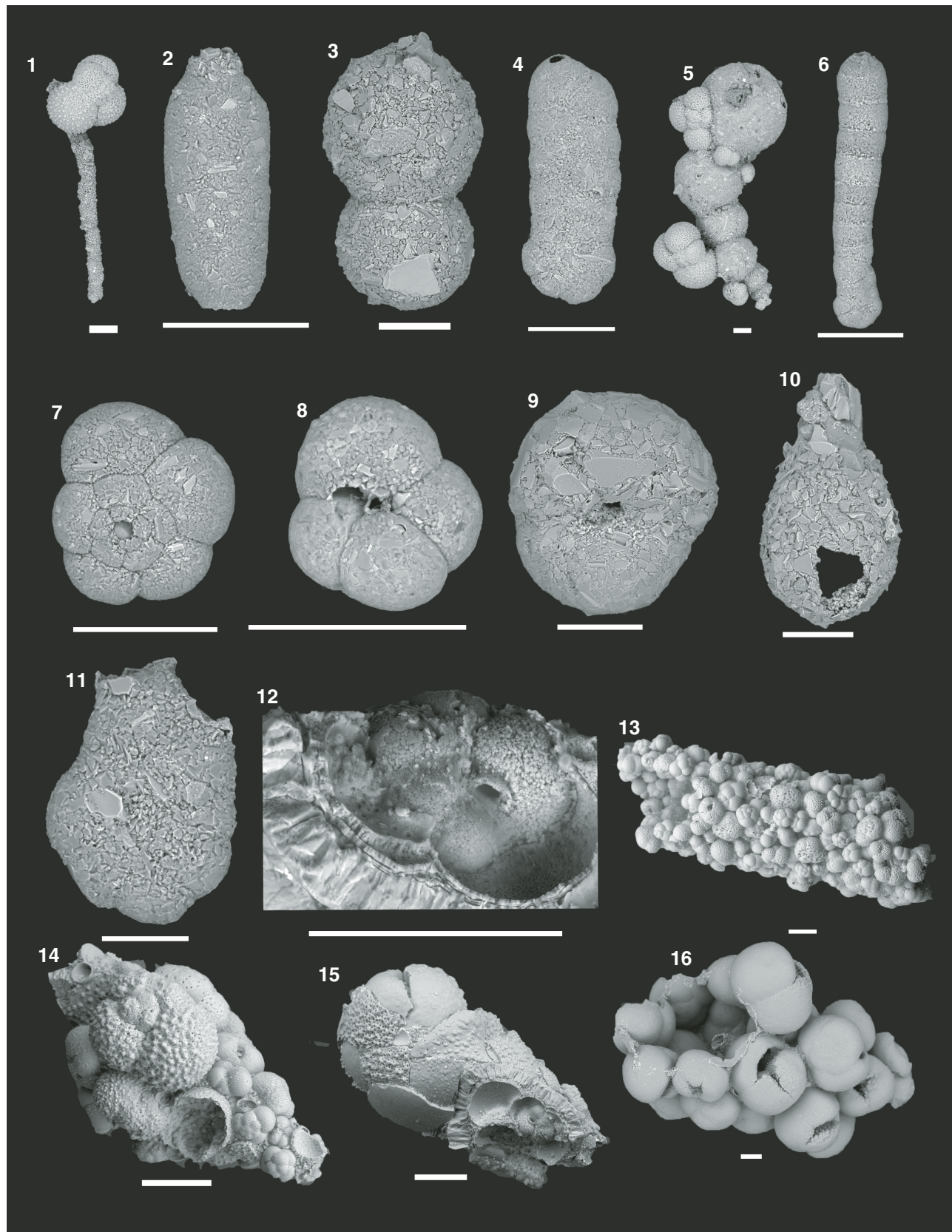
Table T10. Distribution chart of ostracods, Holes U1540A, U1540B, and U1540D. **Download table in CSV format.**

Figure F31. Scanning electron microscope images, Holes U1539C and U1540B. lv = left valve, rv = right valve. A, J. 383-U1540B-4H-CC. (A) *Krithe* sp. A (lv). B, D–I. 383-U1540B-1H-CC. (B) *Krithe* sp. B (lv). C. *Krithe* sp. B (rv; 383-U1539C-7H-CC). (D) *Pelecocythere* sp. (lv). (E) *Pennyella* sp. (lv). (F) *Legitimocythere* sp. A (rv). (G, H) *Legitimocythere acanthoderma* Brady, 1880 (lv; G: adult, H: juvenile). (I) *Arcacythere* sp. (rv). (J) *Bradleya* sp. (lv).
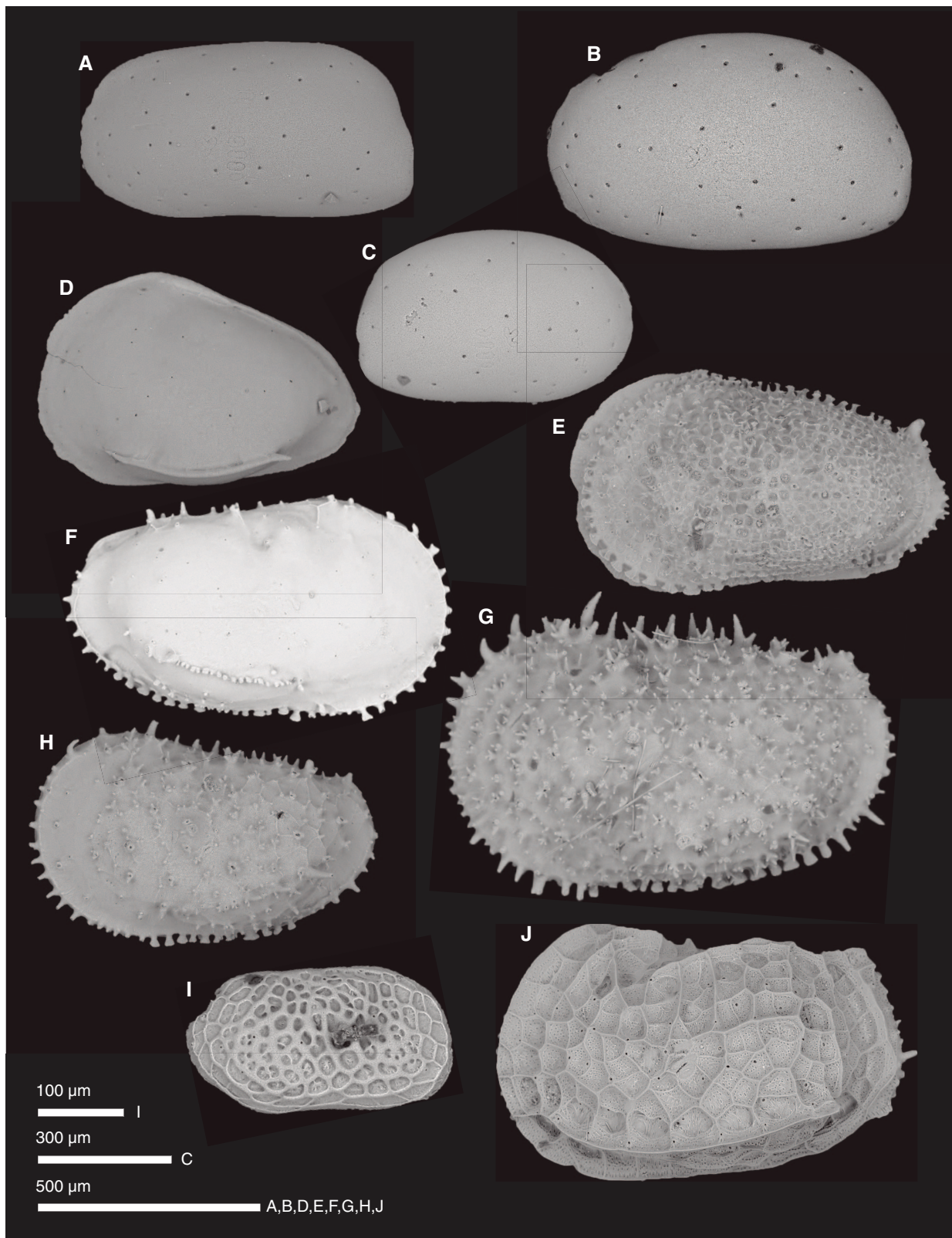
Figure F32. Ostracod scanning electron microscope images of (A–E) *Henryhowella* sp. and (F–H) *Poseidonamicus*, Holes U1540A and U1540B. A. Adult (rv; 383-U1540B-2H-CC). B, C. 383-U1540B-1H-CC. (B) Instar (lv). (C) Instar (rv). D, F. 383-U1540B-7H-CC. (D) Instar (lv). E. Instar (rv; 383-U1540B-19H-CC). (F) *Poseidonamicus* cf. *P. major* Benson, 1972 (A-1 juvenile; lv). G, H. *Poseidonamicus* aff. *P. ocularis* Whatley et al., 1986 (adult; G: lv, H: rv) (383-U1540B-1H-CC).

Paleomagnetism

The natural remanent magnetization (NRM) of archive-half core sections from Site U1540 was measured and remeasured after alternating field (AF) demagnetization at 2 cm increments using the fast 10 Hz data filtering, 250 ms settling time available from the Instrument Measurement Properties, Version 10.2 software controlling the superconducting rock magnetometer (SRM) (see **Paleomagnetism** in the Expedition 383 Methods chapter [Winckler et al., 2021a]). Peak AFs were restricted to a maximum of 15 mT for most sections recovered using the APC/half-length APC (HLAPC) system with standard full and half-length nonmagnetic and steel core barrels (see **Operations**). To further investigate the NRM, an extra peak AF step of 20 mT was applied for Hole U1540D and U1540E cores from below 180 m core composite depth below seafloor, Method A (CCSF-A). In general, the number of demagnetization steps and the peak AF used reflect the demagnetization characteristics of the sediments, the severity of the drill string and/or other magnetic overprints, the desire to use low peak fields to preserve the magnetization for future shore-based studies, and the need to maintain core flow through the laboratory. See Table **T11** for a list of AF demagnetization steps employed for each section. Sections completely affected by drilling disturbance, as noted by the lithostratigraphy and/or paleomagnetism groups, were not measured. Data associated with intervals affected by obvious drilling deformation were culled during data processing.

The NRM of cores recovered from Holes U1540A, U1540B, U1540D, and U1540E exhibit intensities that extend over six orders of magnitude, from 10^{-1} to 10^{-6} A/m (Figure **F33**). After demagnetization at a peak AF of 15 mT, intensities are more constrained and except for a few intervals are lower than 10^{-2} A/m. In general, minor differences in NRM intensities between 10 and 15 mT suggest that the drill string overprint is removed from much of the record. However, the paleomagnetic record in intervals of diatom oozes in the upper 80 m CCSF-A (see **Sedimentology**) and in the sediment below 180 m CCSF-A are characterized by very low signal to noise ratios and/or unremoved overprints, respectively, and are difficult to interpret.

Downhole NRM intensity records from the four holes are comparable (Figure **F33**). NRM intensities of upper sediments are relatively high (10^{-2} to ~10^{-3} A/m) but decrease by about an order of magnitude in the upper 20 m CCSF-A; this decrease is largely attributed to redox conditions because there is no major lithologic transition (see **Sedimentology**) and sulfate rapidly decreases (see **Geochemistry**). Below 20 m CCSF-A, intensities remain low, averaging around 10^{-4} A/m and fluctuating between 10^{-6} and 10^{-3} A/m to ~80 m CCSF-A. Below 80 m CCSF-A, intensities recover and are generally in the 10^{-3} A/m range with a few dips into the 10^{-4} A/m range. Below approximately 160 m CCSF-A, intensities are slightly lower and more variable. Overall, downhole variation of NRM generally follows physical properties such as MS and, aside from redox and possibly other diagenetic changes, lithostratigraphic variability (see **Sedimentology**), suggesting that NRM is largely controlled by lithology.

Polarity changes are best illustrated by downhole inclination. Figure **F34** shows inclination for Holes U1540A, U1540B, U1540D, and U1540E cores before and after AF demagnetization at 15 mT. Prior to demagnetization, inclinations in the uppermost 40 m CCSF-A are dominantly positive, the opposite of the expected inclination during the normal polarity Brunhes Chron. After 15 mT peak AF demagnetization, inclinations become steeply negative and

Table T11. Alternating field (AF) demagnetization steps, Site U1540. **Download table in CSV format.**

Hole	AF demagnetization steps	Cores
U1540A	0, 5, 10, 15	4H, 5H
U1540A	0, 10, 15	All other cores in Hole U1540A
U1540B	0, 5, 10, 15	1H, 2H
U1540B	0, 10, 15	All other cores in Hole U1540B
U1540D	0, 15	1H–9H, 11H–17H
U1540D	0, 5, 10, 15,	10H, 15H, 16H
U1540D	0, 5, 10, 15, 20	21H, 22H
U1540D	0, 15, 20	17H–20H
U1540E	0, 10, 15	2H–5H
U1540E	0, 10, 15, 20	6H–10H

largely consistent with values expected for a geocentric axial dipole (±69°) at the site's latitude. Positive inclinations associated with the reversed polarity of Matuyama Chron (C1r.1r) are observed in Holes U1540A, U1540B, and U1540D; however, the Matuyama/Brunhes polarity transition is not definitively captured in any core, other than possibly at the base of Core 383-U1540B-5H. Three normal polarity subchrons within the Matuyama Chronozone are observed and most easily seen in the inclination splice record (Figure **F35**). The upper polarity transition of the Jaramillo Subchron (C1r.1n) is observed at the base of Core 383-U1540D-8H and somewhat more noisily in Core 383-U1540A-6H, and the lower Jaramillo polarity transition from the Matuyama Chron is observed in Cores 383-U1540B-10H and 383-U1540D-10H. Although there are intervals of mixed polarity below the Jaramillo Subchron, the Cobb Mountain (C1r.2n) Subchron (Figures **F34**, **F35**) is not clearly identified and may be masked by a diatom ooze interval with low NRM signal to noise ratios between 72 and 85 m CCSF-A (see **Sedimentology**). The upper polarity transition from the Olduvai Subchron (C2n) is observed in Core 383-U1540B-15H and somewhat more noisily in Core 383-U1540A-12H. The lower polarity transition from the Matuyama Chron (C2r.1r) is observed in Core 383-U1540B-16H and possibly the upper part of Core 383-U1540A-13H. The normal polarity Reunion Subchron (2r.1n) is recognized in Holes U1540A, U1540B, U1540D, and U1540E with varying fidelity. The boundaries that define each polarity reversal when well constrained within or between cores are listed in Table **T12**.

Below approximately 180 m CCSF-A, polarity becomes more difficult to interpret because well-defined intervals of both polarities are observed on a decimeter scale. For example, there are eleven apparent reversals in Core 383-U1540D-17H alone (Figures **F34**, **F35**). Given biostratigraphic constraints on age and sedimentation rates, these apparent reversals are unlikely to be geomagnetic. Although thorough postcruise study is required to fully characterize this interval, SRM demagnetization behavior provides information useful for the identification of intervals more likely to preserve a primary magnetization and therefore provide polarity information. We developed a parameter to provide an initial assessment:

$$\Delta = \frac{NRM_{10mT} - NRM_{20mT}}{NRM_{20mT}},$$

where NRM_{10mT} and NRM_{20mT} are the NRM intensities after demagnetization at 10 mT and 20 mT, respectively. This equation provides information on the difference between NRM intensities at two AF demagnetization steps (relative to the intensity at the higher demag-

Figure F33. Natural remanent magnetization (NRM) intensity before and after 15 mT peak alternating field demagnetization, Holes U1540A, U1540B, U1540D, and U1540E.
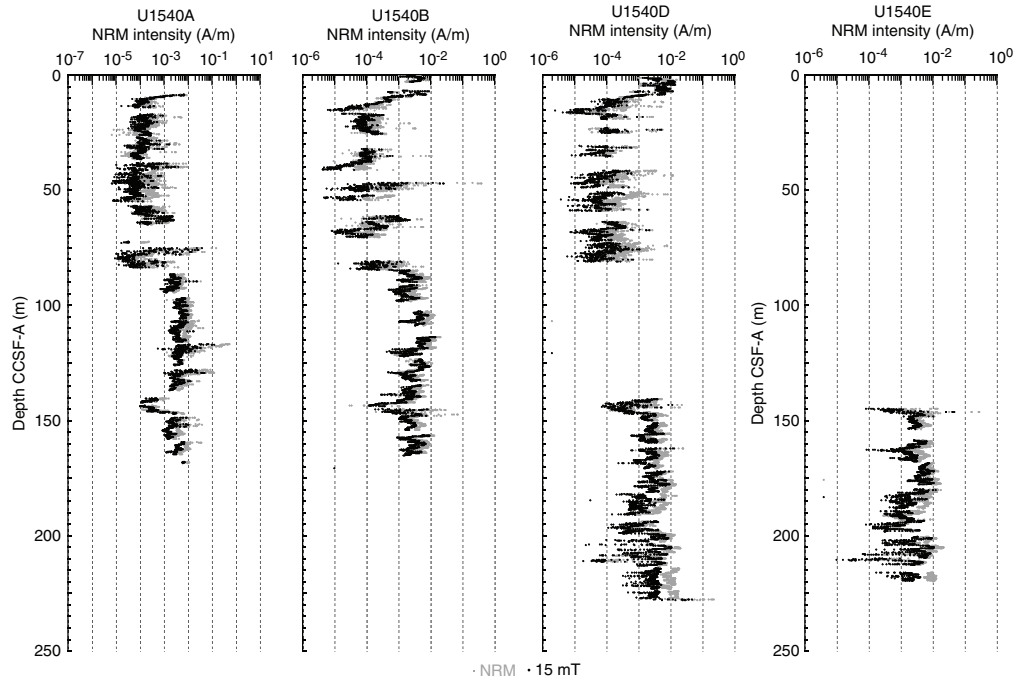

Figure F34. Inclination before and after 15 and 20 mT peak alternating field demagnetization, Holes U1540A, U1540B, U1540D, and U1540E.
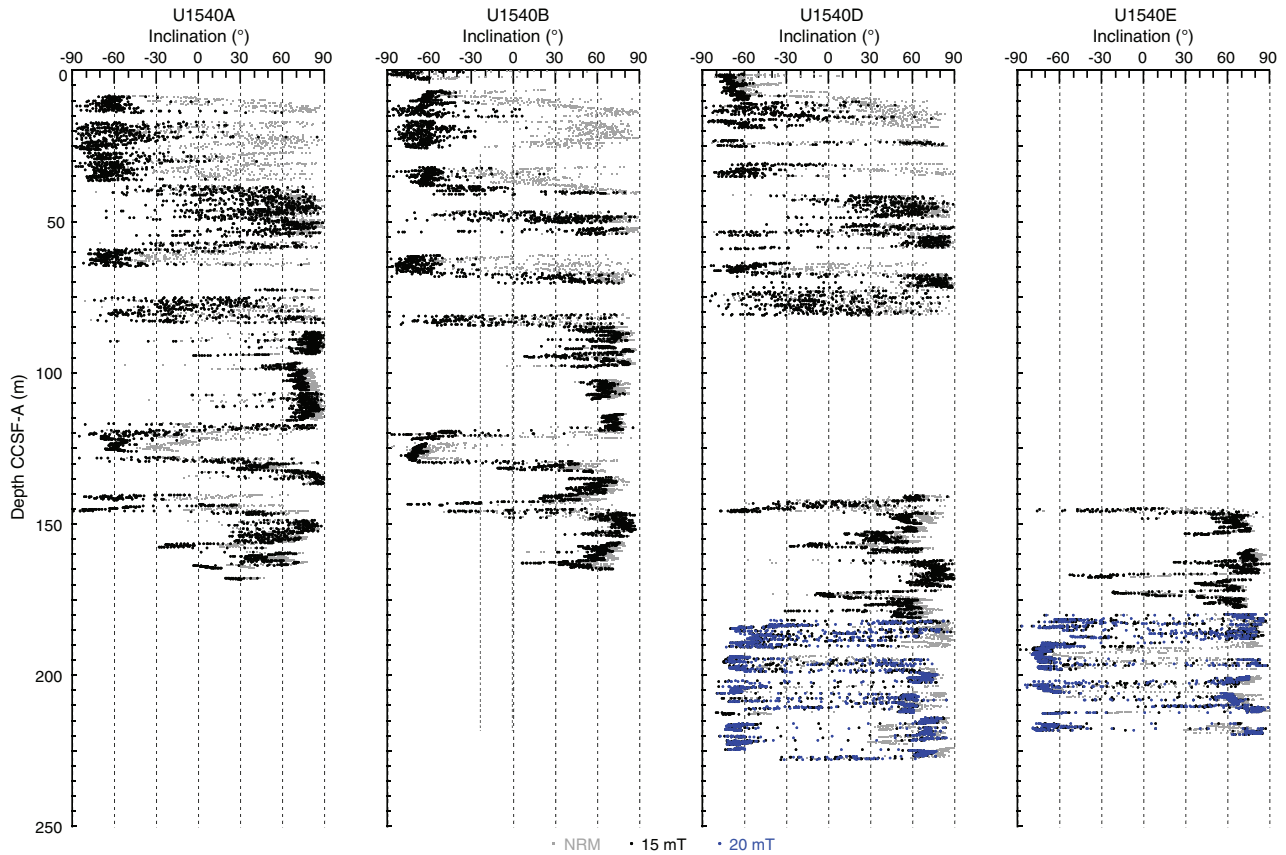
Figure F35. Natural remanent magnetization (NRM) intensity and inclination after 15 mT peak alternating field demagnetization, Site U1540. Polarity interpretation and correlation to geologic timescale (GTS) of Hilgen et al. (2012; GTS2012) are discussed in Paleomagnetism. GPTS = geomagnetic polarity timescale.
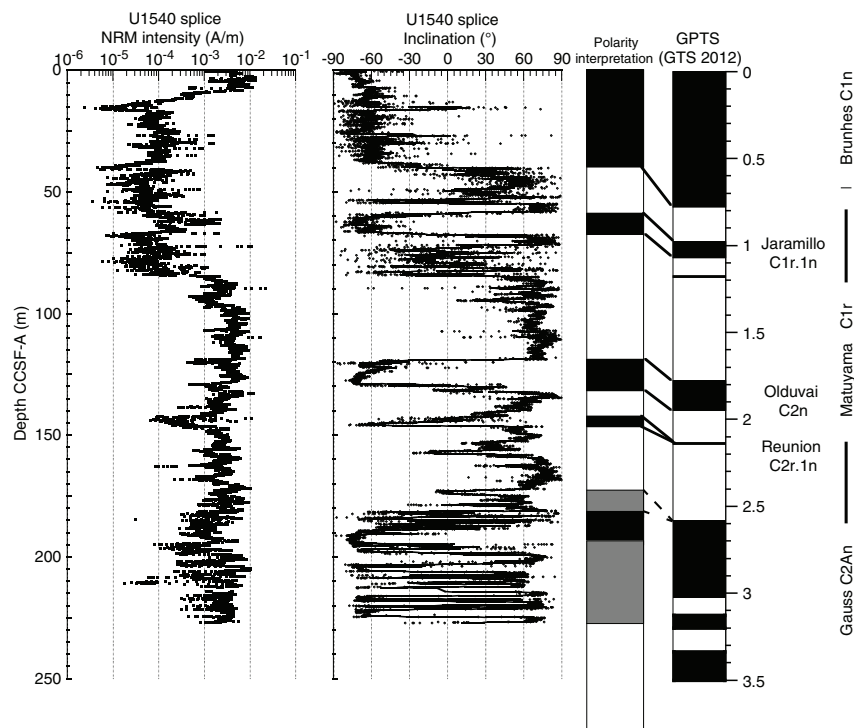

Table T12. Position of identified polarity transitions, Site U1540. GTS2012 = geomagnetic timescale of Gradstein et al. (2012), M/B = Matuyama/Brunhes. t = top. **Download table in CSV format.**

Polarity chron boundary interpretation	Subchron	GTS 2012 age (Ma)	Top core, section	Bottom core, section	Top depth CSF-A (CCSF-A) (m ± m)	Bottom depth CSF-A (CCSF-A) (m ± m)	Top core, section	Bottom core, section	Top depth CSF-A (CCSF-A) (m ± m)	Bottom depth CSF-A (CCSF-A) (m ± m)
			383-U1540A-				383-U1540B-			
C1r.1r (t)	M/B	0.781	3H-7	4H-2	28.00 (36.09) ± 0.5	30.25 (39.71) ± 0.75	5H-5	6H-3	34.40 (38.24) ± 0.75	40.75 (48.67) ± 0.75
C1r.1n (t)	Jaramillo	0.988	6H-2	6H-3	49.25 (58.20) ± 0.75	50.75 (59.70) ± 0.75	8H-6	10H-1	53.00 (53.89) ± 0.40	55.75 (61.25) ± 0.75
C1r.2r (t)		1.072					10H-4	10H-6	60.25 (65.75) ± 0.75	63.25 (68.75) ± 0.75
C2n (t)	Olduvai	1.778	12H-1	12H-4	103.50 (117.06) ± 0.75	108.00 (121.56) ± 0.75	15H-4	15H-6	107.75 (118.25) ± 0.75	110.75 (121.25) ± 0.75
C2r.1r (t)		1.945	12H-6	13H-4	110.00 (123.56) ± 0.75	117.50 (132.52) ± 0.75	16H-4	17H-2	117.50 (128.43) ± 0.75	123.75 (136.28) ± 0.75
C2r.1n (t)	Reunion	2.128					17H-5	17H-7	128.25 (140.78) ± 0.75	130.80 (143.33) ± 0.40
C2r.2r (t)		2.148	14H-6	15H-1	130.00 (145.36) ± 0.75	133.00 (150.01) ± 0.75	17H-7	18H-3	130.80 (143.33) ± 0.40	134.75 (148.07) ± 0.75

Polarity chron boundary interpretation	Subchron	GTS 2012 age (Ma)	Top core, section	Bottom core, section	Top depth CSF-A (CCSF-A) (m ± m)	Bottom depth CSF-A (CCSF-A) (m ± m)	Top core, section	Bottom core, section	Top depth CSF-A (CCSF-A) (m ± m)	Bottom depth CSF-A (CCSF-A) (m ± m)
			383-U1540D-				383-U1540E-			
C1r.1r (t)	M/B	0.781	6H-5	7H-2	36 (34.87) ± 0.4	41.5 (42.06) ± 0.75				
C1r.1n (t)	Jaramillo	0.988	8H-6	8H-7	57.75 (58.49) ± 0.75	58 (58.74) ± 0.3				
C1r.2r (t)		1.072	10H-3	10H-5	64 (66.13) ± 0.75	67 (69.13) ± 0.75				
C2n (t)	Olduvai	1.778								
C2r.1r (t)		1.945								
C2r.1n (t)	Reunion	2.128	13H-1	13H-4	131.70 (140.79) ± 0.75	136.25 (145.34) ± 0.75				
C2r.2r (t)		2.148	13H-4	13H-6	136.25 (145.34) ± 0.75	139.25 (148.34) ± 0.75	2H-1	2H-3	135.75 (144.60) ± 0.75	138.75 (147.60) ± 0.75

netization step) and is sensitive to three particular conditions. The first is that the primary magnetization is superimposed by a secondary magnetic component with an opposing polarity. When AF demagnetization preferentially removes the secondary component, the overall intensity may increase instead of decrease. In such a case, Δ is negative. This does not necessarily imply a problem with the magnetization, but it does indicate that the overprint may have a higher coercivity that has not been completely removed by 10 mT peak AF. The second condition occurs when a significant amount of remanence is lost between 10 and 20 mT, indicating a soft, very low coercivity magnetization that could be susceptible to remagnetization either within the sediment or during coring. Empirically, we set $\Delta = 1$ as the threshold to indicate potentially unstable components (when NRM_{20mT} is only half of NRM_{10mT}). As a result, records within

the range of Δ = [0–1] are considered more likely to preserve a primary magnetization. Third, normalizing by the NRM intensity after 20 mT AF provides an additional criterion because weakly magnetized samples with low signal-to-noise ratios give rise to higher values that would fall out of range. Results are shown in Figure **F36**. Most of the record from 180 to ~190 m CCSF-A, where frequent polarity alternations are observed, have a Δ > 1 and therefore are likely to have been overprinted. After demagnetization at 20 mT peak AF, the inclinations tend to decrease with respect to the incli-

Figure F36. Natural remanent magnetization (NRM) intensity in sediment cores deeper than 180 m CCSF-A with unstable magnetic components highlighted based on the Δ parameter, Site U1540. Left: NRM intensity after demagnetization at 15 and 20 mT. Middle: variation of NRM intensity. Gray vertical lines = thresholds for NRM records that are mixed with antipodal components (Δ < 0) and that contain soft components or poorly defined magnetization (Δ > 1). Right: inclination after demagnetization at 20 mT with comparison of inclination at 15 mT for intervals with Δ < 0 and Δ > 1. For intervals with Δ < 0, inclination after 20 mT peak AF (black triangles) and after 15 mT peak AF (green crosses). For intervals with Δ > 1, inclination after 20 mT peak AF (red triangles) and after 15 mT peak AF (gray crosses). Comparisons are used to reveal how secondary magnetization may influence the inclination data. Inclination data at 20 mT is preferred over that at 15 mT.
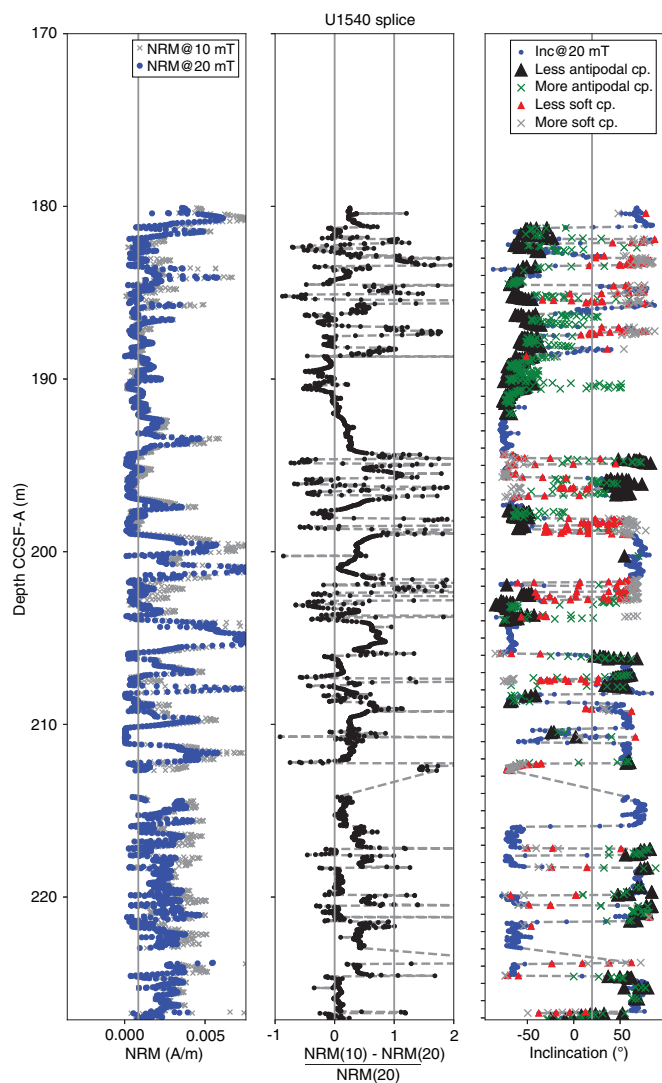
nation at 15 mT, suggesting that higher AFs are likely needed to resolve the primary remanence. The alternating polarity may therefore be a result of an artifact induced by variations in coercivity controlling the likelihood that the sediment is overprinted. Biostratigraphy suggests that these sediments were deposited near the time of the Gauss/Matuyama polarity transition and before, so the actual polarity transition is likely obscured by these variations. Comprehensive rock magnetic experiments that could not be performed onboard are required for a more complete understanding. As a result, a magnetostratigraphic interpretation was not attempted below the Reunion Subchron (Table **T12**) but may be possible during postcruise studies.

Geochemistry
Sediment gas sampling

As part of IODP's routine environmental protection and safety monitoring program, we measured headspace gas concentrations in Cores 383-U1540A-1H through 16H, 383-U1540B-2H, and 383-U1540D-5H through 21H at a resolution of one sample per core between 6.02 and 209.59 m CSF-A (see **Geochemistry** in the Expedition 383 methods chapter [Winckler et al., 2021a]). Near the bottom of Hole U1540D at 209.59 m CSF-A, we collected hard rock samples in a 5 cm³ airtight glass vial in lieu of available core sediment and tested for headspace hydrocarbon content. Methane (CH_4) concentrations are low throughout sediments at Site U1540, with values never exceeding 6.44 ppmv (Figure **F37**; see U1540-T1.xlsx in GEOCHEM in **Supplementary material**). Concentrations of ethene (C_2H_4), ethane (C_2H_6), propene (C_3H_6) and propane (C_3H_8) remain below detection limit.

Interstitial water chemistry

At Site U1540, we collected 56 whole rounds for interstitial water (IW) samples from Holes U1540A (44 samples; 0–148.3 m CSF-A), U1540B (6 samples; 6.05–21.59 m CSF-A), and U1540D (6 samples; 157.42–204.82 m CSF-A) at a resolution of three per core from 0 to 120 m CSF-A, two per core from 120 to 150 m CSF-A, and one per core from 150 m CSF-A to the bottom of the hole (see U1540-T2.xlsx in GEOCHEM in **Supplementary material**). We collected a mudline sample from Hole U1540B and allowed it to settle for several hours before filtering it through a 0.45 μm syringe-tip filter. Filtered mudline water underwent all standard shipboard chemistry. We squeezed whole rounds and subsampled for IW according to the methods described in **Geochemistry** in the Expedition 383 methods chapter (Winckler et al., 2021a).

Alkalinity and pH

Above 134.27 m CSF-A, alkalinity and pH show no obvious trends, varying around averages of 3.4 ± 0.5 mM (±1σ) and 7.96 ± 0.07, respectively (Figure **F38**). Below this depth, alkalinity and pH exhibit almost identical behavior, first increasing to a local peak at 157.42 m CSF-A and then decreasing steadily to the bottom of the core.

Salinity, chlorinity, sodium, and magnesium

Salinity for all IW samples is constant at 35 throughout the core. Chlorinity exhibits a slight increase from ~557 mM at the seafloor to ~562 mM at ~40 m CSF-A, below which depth it remains roughly constant at an average of 565 ± 5 mM (Figure **F39**). Sodium (Na) and magnesium (Mg) are constant with depth at 463 ± 4 mM and 51 ± 0.5 mM, respectively (Figure **F39**).

Iron, manganese, and lithium

Above 70.75 m CSF-A, dissolved iron (Fe) concentrations are below detection limit in the IW (Figure F40). Between 73.78 and 176.39 m CSF-A, Fe is present in the IW, and it reaches a maximum of 12.83 at 118.24 m CSF-A. Below 176.39 m CSF-A, dissolved Fe decreases rapidly in the IW, possibly due to scavenging, to below detection limit. This may be caused by the presence of abundant Fe oxides at the bottom of the core. Manganese (Mn) concentrations increase sharply from below detection limit in the mudline sample to a local maximum of 28 µM at 6.05 m CSF-A (Figure F40), indicating anaerobic, reductive dissolution of Mn oxides in the uppermost 6 m of sediment. Mn concentrations drop again to 10.9 µM at 15.57 m CSF-A before beginning a slow rise at 77.24 m CSF-A, where they remain roughly constant at 32.6 ± 3.1 µM to 185.76 m CSF-A. At this depth, Mn is depleted from the IW to 0.3 µM in the bottommost sample, similar to the behavior of Fe in this interval. Dissolved lithium (Li) displays a constant IW concentration of 18.6 ± 0.4 µM down to 185.76 m CSF-A (Figure F40). Interestingly, below this depth Li

concentrations increase to 22.7 µM in the bottom sample. Increases in Li could be due to influence of hydrothermal fluid or alteration.

Calcium, strontium, and bromide

Calcium (Ca) concentrations show a decreasing trend in the uppermost 30.97 m and reach 7.9 mM, after which they remain fairly constant to ~148 m CSF-A (Figure F41). Increases in Ca concentrations are apparent below 176.39 m CSF-A, and maximum values reach ~9.8 mM in the bottommost sample (Figure F41). This increase in Ca concentration is concurrent with scavenging of IW Fe and Mn. Hydrothermal fluids are considered to be a net source of Ca^{2+} (German and Von Damm, 2003). Given the proximity of Site U1540 to a ridge axis, the influence of hydrothermal fluid as a potential explanation for the increase in Ca concentration cannot be ruled out.

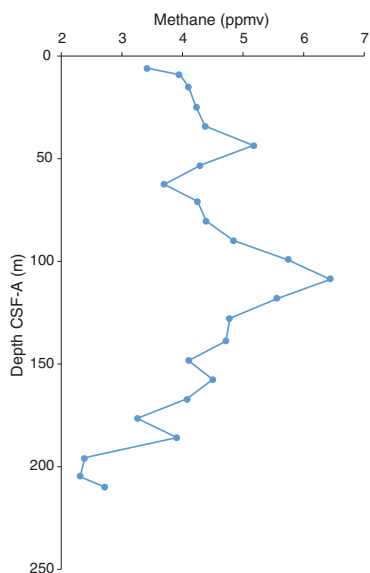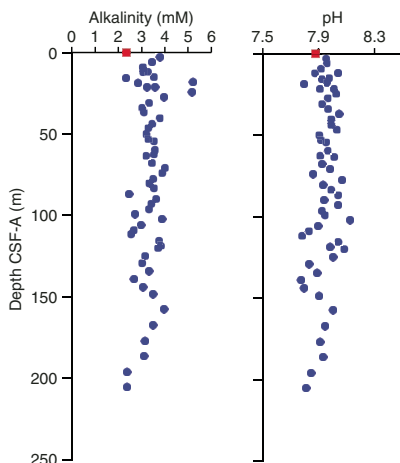Figure F37. Headspace methane concentrations, Site U1540.

Figure F39. Interstitial water chloride, sodium, and magnesium, Site U1540. Chloride data points = mean of triple measurements. A few chloride measurements were discarded (hence not plotted) due to possible error at the time of measurements. Red square = overlying seawater sample.

Figure F38. Interstitial water alkalinity and pH, Site U1540. Red square = overlying seawater sample.
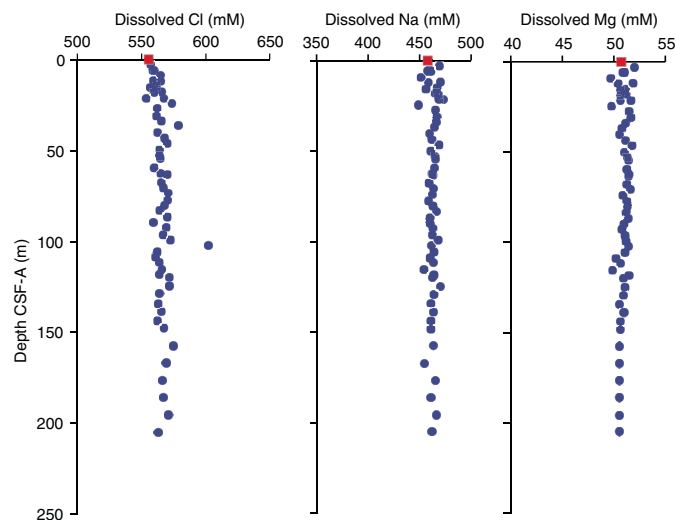

Figure F40. Interstitial water iron, manganese, and lithium, Site U1540. Red square = overlying seawater sample.
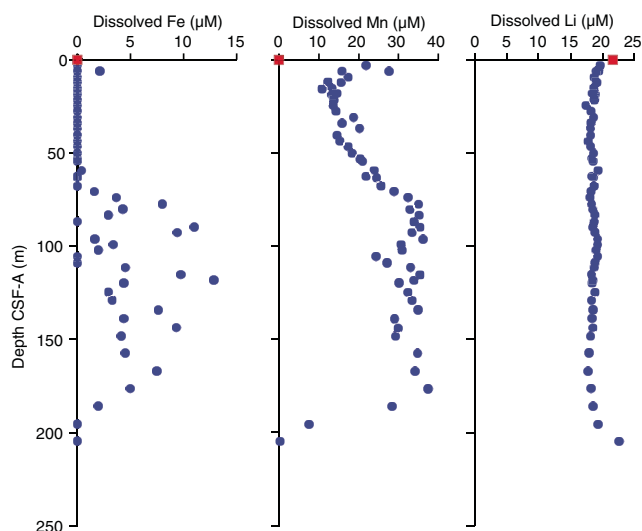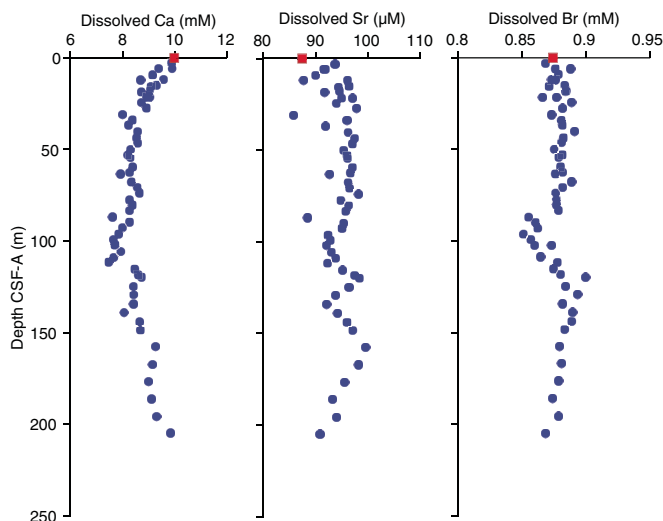
Figure F41. Interstitial water calcium, strontium, and bromide, Site U1540. Red square = overlying seawater sample.

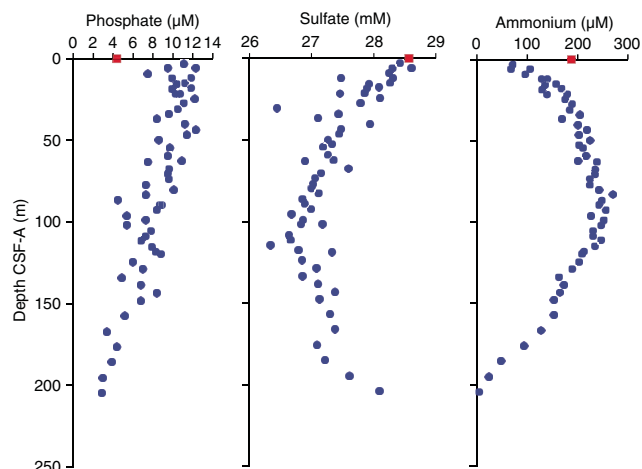Figure F42. Interstitial water phosphate, sulfate, and ammonium, Site U1540. Red square = overlying seawater sample.

Figure F43. Interstitial water potassium, silicon, boron, and barium, Site U1540. Red square = overlying seawater sample.

Strontium (Sr) concentrations down to ~34 m CSF-A show a scattered pattern with an average value of 94.3 ± 3.5 µM (Figure **F41**). Between 33.98 and 134.27 m CSF-A, Sr concentrations are relatively constant with an average value of 94.9 ± 2.3 µM and a local high of 97.4 µM at 118.24 m CSF-A. Below 134.27 m CSF-A, Sr concentrations decrease consistently to the bottom of the hole, reaching 90.7 µM at 204.82 m CSF-A.

Bromide concentrations at Site U1540 remain fairly constant around an average of 0.88 ± 0.1 mM with a local minimum around ~100 m CSF-A (Figure **F41**).

Phosphate, sulfate, and ammonium

Phosphate (PO_4^{3-}) concentrations decrease gradually with depth from 11.1 µM near the seafloor to 2.9 µM at 20.82 m CSF-A (Figure **F42**). The uppermost PO_4^{3-} value (11.1 µM) is substantially higher than the mudline PO_4^{3-} value (4.4 µM). Concentrations of PO_4^{3-} show some variability but exhibit a broad decreasing trend downhole (Figure **F42**).

Sulfate (SO_4^{2-}) concentrations exhibit a prominent decrease from 28.6 mM at the top of the core to 26.6 mM at 108.72 m CSF-A (Figure **F42**). Below this depth, SO_4^{2-} concentrations start to increase, reaching 28.1 mM at 204.82 m CSF-A.

Ammonium (NH_4^+) concentrations at the top of the record (70.2 µM) are lower than the mudline sample (187 µM) (Figure **F42**). However, subsequent downhole samples show a gradual increase to 251 µM at 99.21 m CSF-A, below which depth concentrations decrease, reaching 4.5 µM at 204.82 m CSF-A. Gradual increase in NH_4^+ in the top part of the record could be related to NH_4^+ accumulation in IW due to organic matter remineralization. The decreasing trend in the lower part of the record might suggest the presence of anaerobic oxidation of ammonium or adsorption onto clay minerals.

Potassium, silicon, boron, and barium

Potassium (K) concentration in the IW at the top of the record is similar to the surface value of 10.3 mM (Figure **F43**). The rest of the downhole K record is constant and has an average value of 10.8 ± 0.3 mM. Two small excursions to higher values occur at ~105 and ~135 m CSF-A.
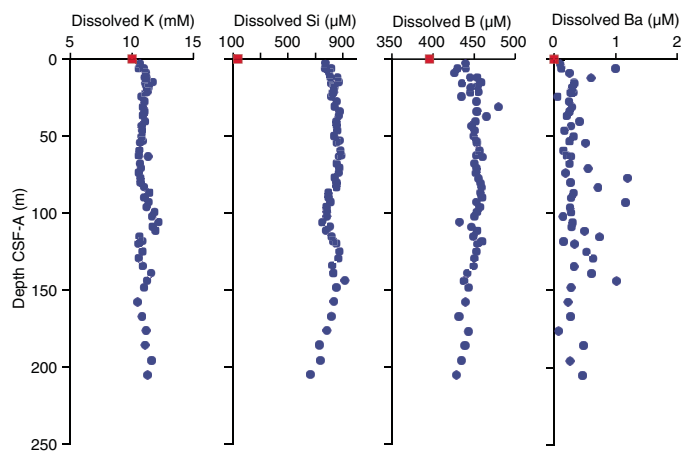
The mudline silica (Si) concentration of 134 µM is much lower than that of the uppermost IW sample, which has a Si concentration of 774 µM (Figure **F43**). A gradual increase in Si concentrations is tracked in the uppermost 15 m, below which depth concentrations remain constant at 857 ± 19 µM to 83.12 m CSF-A. Prominent Si scavenging is observed from 148.3 m CSF-A to the bottom of the hole.

Boron (B) concentrations show scatter in the uppermost ~40 m (Figure **F43**). Below this depth, B concentrations hover around an average of 448 ± 12 µM. Starting at ~176 m CSF-A, similar to Si, boron seems to be scavenged away from the IW.

Overall barium (Ba) concentrations are low throughout the record, and the majority of the values range between 0.1 and 0.3 µM (Figure **F43**). There is much scatter in the Ba, which may have resulted from measuring difficulties for such low concentration samples.

Bulk sediment

Calcium carbonate

A total of 64 $CaCO_3$ concentration measurements from Holes U1540A, U1540B, and U1540D were collected at a resolution of two to three samples per core (Figure **F44**; see U1540-T3.xlsx in GEO-

Figure F44. Solid phase geochemistry of (A) CaCO₃, (B) total organic carbon (TOC)/total nitrogen (TN), (C) TN, and (D) TOC. Gray bar = sample overlap between Holes U1540A (open circle) and Hole U1540B (square). No sample overlap occurs between Hole U1540A and Hole U1540D (open triangle).
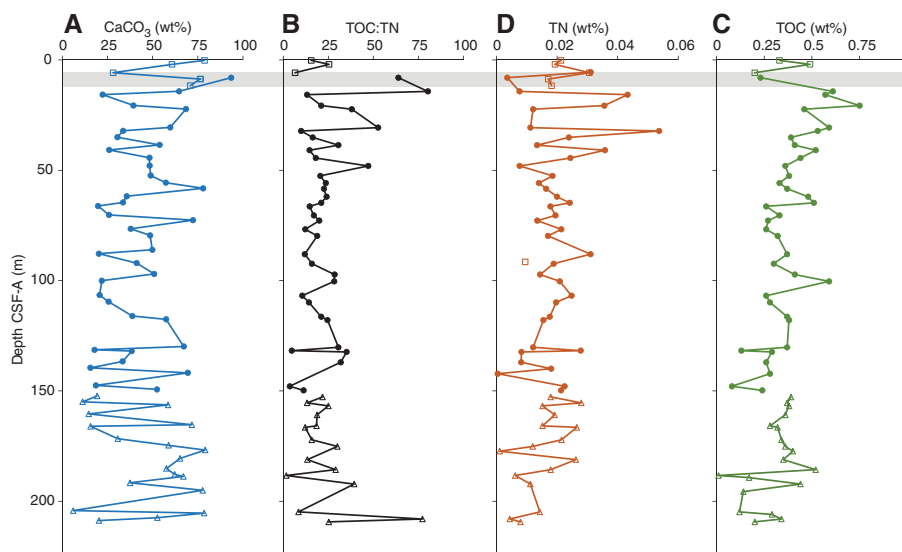
CHEM in **Supplementary material**). The composite CaCO₃ record has a mean value of 46.3 ± 21.9 wt% across the entire study interval. CaCO₃ concentrations range from a minimum of 6.0 wt% at 204.24 m CSF-A in Hole U1540D to a maximum of 93.5 wt% at 8.03 m CSF-A in Hole U1540A (Figure **F44**), and the latter value corresponds to MIS 11. However, MIS 11 CaCO₃ results obtained at a similar depth of 11.66 m CSF-A in Hole U1540B, show a CaCO₃ content of 70.8%. Drilling disturbance was reported in Hole U1540A between approximately 6.5 and 9 m CSF-A, which might explain the CaCO₃ discrepancy between the two MIS 11 intervals in the two holes. CaCO₃ measurements show a good correlation with red, green, blue (RGB) blue and color reflectance L* measurements (see **Sedimentology**).

Major and trace elements

A total of 25 samples taken for CaCO₃ analyses from Holes U1540A–U1540C were also analyzed for major and minor element concentrations using inductively coupled plasma–atomic emission spectroscopy (ICP-AES) (Figure **F45**; see U1540-T4.xlsx in GEO-CHEM in **Supplementary material**). Elemental oxides (MgO, K₂O, Fe₂O₃, and TiO₂) show a strong positive correlation with aluminum oxides (Figure **F45**). This correlation could indicate the presence of micaceous/clay minerals. SiO₂ and CaO do not exhibit any well-defined pattern when plotted against Al₂O₃ (Figure **F45**), possibly because of dilution of lithogenic material by calcareous and siliceous biogenic material. Samples from below 150 m CSF-A potentially contain hydrothermally altered material (Figure **F45**). These deep samples are enriched in almost all analyzed elements, suggesting a higher content of clays and/or other minerals at depth. Above 150 m CSF-A, ratios of MnO and P₂O₅ show no discernible relationship to aluminum oxides, but below this depth they show a positive correlation (Figure **F45**). This may indicate that above 150 m CSF-A these elements are controlled by redox changes and authigenic mineral precipitation, whereas below this depth these elements are present in a constant ratio with aluminum (i.e., in clays).

The bulk sediment below 150 m CSF-A contains higher contents of Al, Mg, Ba, K, Mn, Fe, titanium (Ti), zinc (Zn), and zircon (Zr) relative to the shallower sediments (Figure **F46**). Similar en-

richment in Mn concentration occurs deeper in the sediment column at ~200 m CSF-A. Sr and Ca show a strong correlation and slight decrease with depth, suggesting the dissolution of Sr-rich CaCO₃ samples. Bulk sediment Ca primarily represents biogenic CaCO₃; hence, covariation of Sr and Ca can be attributed to incorporation of Sr in biogenic CaCO₃. Contents of Si decrease slightly below 150 m CSF-A, likely because of dilution of siliceous material with clays or other lithogenic materials.

Organic carbon

A total of 64 CaCO₃ samples were subsampled for total carbon (TC) analysis. Total organic carbon (TOC) estimates were obtained by measuring the TC and subtracting the contribution of inorganic CaCO₃ (see **Sedimentary inorganic and organic carbon, nitrogen, and carbonate content** in the Expedition 383 methods chapter [Winckler et al., 2021a]). TOC results obtained from Holes U1540A, U1540B, and U1540D are shown in Figure **F44** (see U1540-T3.xlsx in GEOCHEM in **Supplementary material**). TOC concentrations have a mean value of 0.35 ± 0.14 wt% across the entire study interval. In the upper portion of the core, TOC values increase from 0.2 wt% at 8.03 m CSF-A to 0.75 wt% at 20.63 m CSF-A. Another peak in TOC of 0.59 wt% is observed farther downhole at 100.06 m CSF-A, and a TOC minimum of 0.01 wt% occurs at 187.81 m CSF-A. The TOC record shows no correlation to the CaCO₃ record ($r^2 = 0$) downcore.

Total nitrogen

A total of 64 samples were measured for total nitrogen (TN) simultaneously with TC. It was assumed that all the nitrogen detected in the sediment was organic in origin. TN values obtained from Holes U1540A, U1540B, and U1540D are shown in Figure **F44** (see U1540-T3.xlsx in GEOCHEM in **Supplementary material**). TN has a mean value of 0.019 ± 0.0095 wt% across the entire study interval. A maximum TN concentration of 0.054 wt% occurs at 32.11 m CSF-A, and a minimum concentration of 0.0036 wt% occurs at 8.03 m CSF-A. In the upper portion of the core between 0.2 and 47.9 m CSF-A, TN values are more variable and have a mean value of 0.023 ± 0.015 wt%. Farther downcore between 52.39 and 208.75 m CSF-A,

Figure F45. Bulk sediment elemental (Na, K, Si, P, Mg, Ca, Ti, Mn, and Fe) oxides vs. aluminum oxide, Site U1540. Red crosses indicate samples below 150 m CSF-A, within the region of potential hydrothermal alteration.
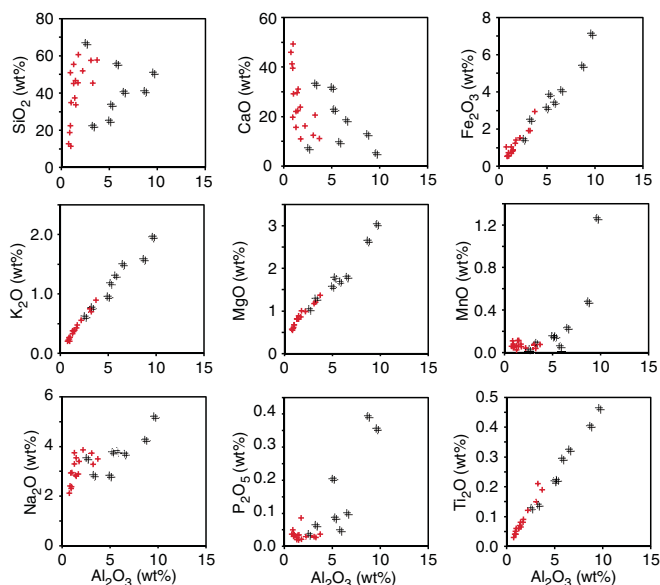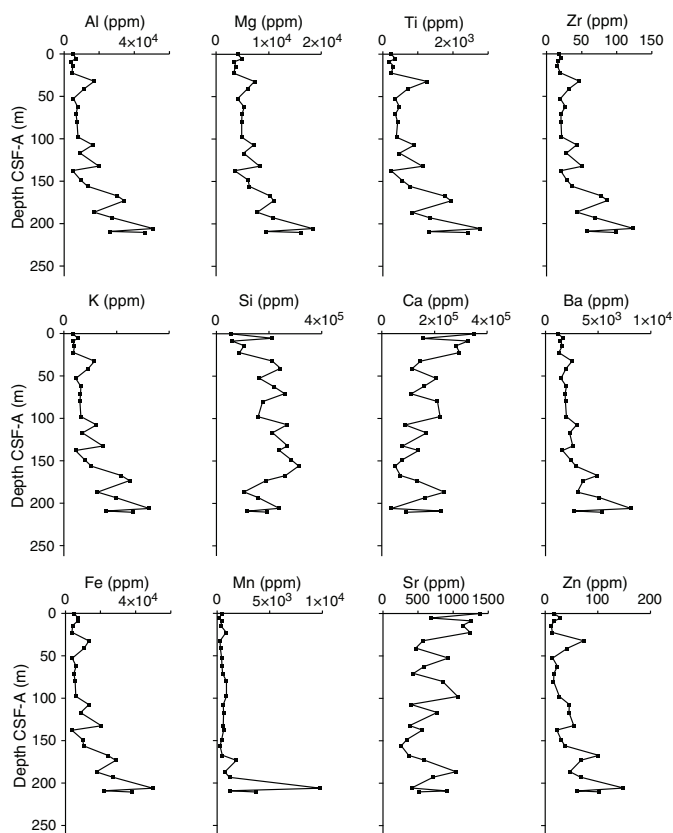

Figure F46. Bulk sediment major and minor element concentrations, Site U1540.

variability decreases slightly relative to the upper portion of the record with a mean value of 0.018 ± 0.006 wt%. A total of 28 duplicate samples were run, and overall repeatability of TN measurements was very low throughout Site U1540. At least 12 samples fell below detection limits of the elemental analyzer; therefore, shipboard TN results must be repeated postcruise to obtain repeatable results.

Organic carbon to organic nitrogen ratios

The relative abundance of TOC and TN is plotted as a ratio (TOC:TN) in Figure **F44** (see U1540-T3.xlsx in GEOCHEM in **Supplementary material**). Mean TOC:TN at Site U1540 is 23.49 ± 16.07 wt% across the entire study interval. A maximum TOC:TN value of 80.3 occurs at 14.22 m CSF-A, and a minimum value of 1.61 occurs at 187.81 m CSF-A. The upper portion of the core between 0.2 and 47.9 m CSF-A displays a higher and more variable TOC:TN record with a mean value of 30.20 ± 21.83. Farther downhole between 52.39 and 204.24 m CSF-A, TOC:TN values are lower and less variable with a mean value of 19.27 ± 8.79. At 207.44 m, TOC:TN increases again to a peak value of 77.27. This maximum TOC:TN value corresponds to the depth of observed potential hydrothermal alteration at Site U1540. Values between 4 and 10 indicate algal-derived organic matter, and values greater than 20 indicate terrestrial C_3/C_4 plant-derived organic matter (Meyers, 1994, 1997). High mean TOC:TN values of 23.49 at Site U1540 suggest that organic matter derives primarily from terrestrial plant material, rather than algae throughout the record. However, TN values are overall very low and the derived TOC:TN values have to be regarded with caution.

Summary

Overall, the inorganic geochemistry of the IW and bulk sediments show evidence of hydrothermal alteration of the sediment below ~200 m CSF-A and possibly as shallow as 150 m CSF-A. In cores from the lower half of the hole (below ~150 m CSF-A), we observe decreases in pH and alkalinity, increases in dissolved Ca and Li concentrations, and rapid removal of dissolved Fe and Mn from the IW, most likely through scavenging. This profile (low pH/alkalinity and high Ca and Li) is characteristic of hydrothermal fluids (German and Von Damm, 2003) and suggests influence of hydrothermal fluid through the porous basement basalt below the sediment. We also observe a removal of NH_4^+ and supply of SO_4^{2-} to the IW below ~100 m CSF-A, which may be the result of microbially driven oxidative processes (sulfide oxidation and anaerobic ammonium oxidation) occurring in the underlying basalt or in the deep sediments (Bach and Edwards, 2003; Hu et al., 2011). NH_4^+ is also known to adsorb strongly to clays (Robinson et al., 2012); therefore, the removal of IW NH_4^+ may be caused partially or fully by adsorption due to the higher clay content in the deeper sediment.

$CaCO_3$ is generally very high, has an average content of 46.3 wt%, and shows a good correlation with RGB blue data.

Organic carbon contributes a maximum of 0.75 wt% to the TC pool throughout this site and has no correlation to $CaCO_3$ content. TN never exceeds 0.054 wt%, and low concentrations yield poor reproducibility of samples due to instrumental detection limits. The mean value of TOC:TN at Site U1540 is 23.49, which suggests that organic material at this site is primarily terrestrially derived. A peak

TOC:TN value at 207.44 m CSF-A aligns with an interval of possible hydrothermal alteration at Site U1540, which may explain elevated values. However, the TOC:TN data should be interpreted with caution given the low TN concentrations and reproducibility at this site.

The bulk sediment elemental composition indicates that, based on correlations with Al_2O_3, clay content is a controlling factor for the content of some elements (Mg, K, Fe, and Ti), whereas other elements are controlled by biogenic materials and potentially authigenic mineral formation (Si, Ca, and P). Many of the analyzed elements are enriched in the bulk sediment below 150 m CSF-A, which provides further evidence for possible hydrothermal alteration and/or input in this interval because hydrothermally influenced material is known to be highly enriched in major and minor elements, including Fe, Mn, and Zn (German and Von Damm, 2003).

Physical properties

The shipboard physical properties measured at Site U1540 comprise nondestructive whole-round measurements of GRA bulk density, MS, and P-wave velocity using the Whole-Round Multisensor Logger (WRMSL) and NGR measurements on all core sections from Holes U1540A–U1540E. Additional physical property data include thermal conductivity on whole-round core sections from all holes. Thermal conductivity measurements were made using a needle probe on whole rounds from Holes U1540A–U1540E. To support stratigraphic correlation and optimize overlaps to cover coring gaps, GRA and MS data were acquired for all holes before temperature equilibration using the Special Task Multisensor Logger (STMSL) at a 3 cm resolution with a 1 s GRA acquisition time and one MS measurement. These data were stored in the IODP Laboratory Information Management System (LIMS) but are not further evaluated and reported; further use is discouraged because WRMSL and Section Half Multisensor Logger (SHMSL) data from all core sections are available in LIMS. Measurements were carried out on all recovered sections, including sections with incompletely filled liners or partially water-filled sections but excluding core catchers.

After splitting the core sections, discrete samples were taken from the working halves with representative lithostratigraphic units for moisture and density (MAD) measurements to determine porosity, bulk, dry, and grain density values from Holes U1540A and U1540E. Discrete compressional wave velocity measurements (two to three) were conducted on at least one working-half section of each core using the P-wave caliper (PWC) contact probe system on the Section Half Measurement Gantry (SHMG). Archive halves were measured with the SHMSL for MS and color reflectance.

Physical property data were used for hole-to-hole stratigraphic correlation and splicing (see **Stratigraphic correlation**). In line with the lithology at Site U1540, multiple physical property parameters display changes and variability throughout the recovered strata. They generally correlate well with the alternating lithologies at Site U1540 over both short and longer timescales (Figure **F15**).

Discrete thermal conductivity measurements were carried out on one section per core on average and on two sections per core in Holes U1540C and U1540D. In total, 107 samples with three measurements each were taken, including multiple samplings with different heating power adjustments. Because of the soft and water-rich nature of the upper sections, a number of measurements did not yield sufficient results to be usable. In total, about 70 sample intervals yielded one or more thermal conductivity values that are undergoing further quality control.

Magnetic susceptibility

Both whole-round measurements on the WRMSL and discrete point measurements on the SHMSL were used to characterize MS at Site U1540 (Figures **F47**, **F48**). Both methods yielded a similar range of values and similar downhole variability. Values range from −2 to 70 instrument units (IU) for both the WRMSL and SHMSL (see **Physical properties** in the Expedition 383 methods chapter [Winckler et al., 2021a] for details on instrument units [~10^{-5} SI]). In the upper 75 m of Site U1540, MS values are very low (between −2 and 5), often leading to negative instrument readings on both the WRMSL and the SHMSL logging banks. These low values lead to

Figure F47. Magnetic susceptibility (MS) loop and MS point sensor data, Holes U1540A and U1540E. Light blue = Hole U1540A MS loop sensor, dark blue = Hole U1540E MS loop sensor, orange = Hole U1540A MS point sensor, red = Hole U1540E point sensor.
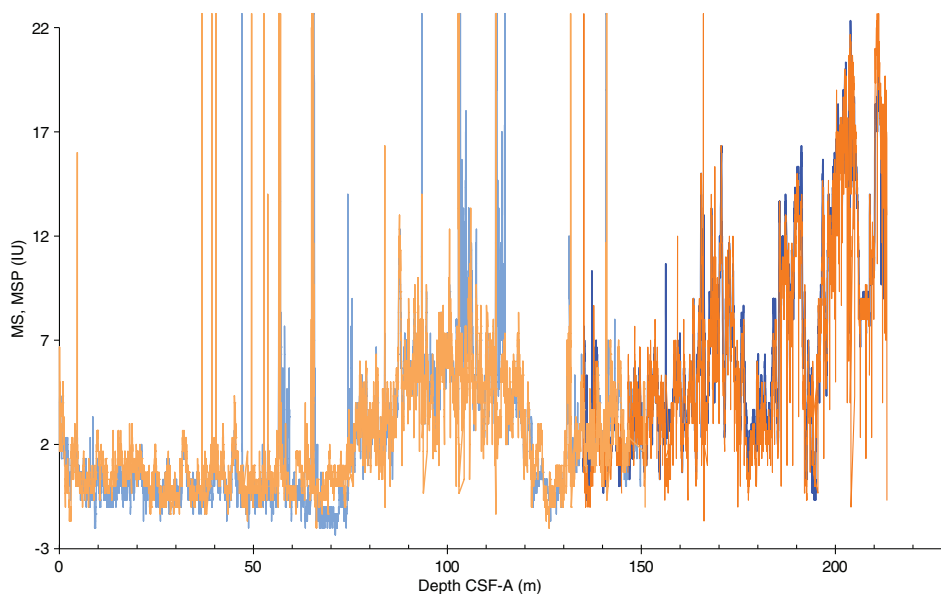
low signal-to-noise ratios and a high influence of secondary factors on the primary sedimentary signal, mostly through APC-related artifacts like water or air bubbles or voids in the core liners. Below 75 m CSF-A, MS values increase toward the bottom of the site and reach 20 IU, with minima at 125 m CSF-A in Hole U1540A and 195 and 207 m CSF-A in Hole U1540E. Relatively high values of >5 IU are attributed to outsized clasts or dropstones and are not representative of the overall sediment composition. In the upper sections of some cores (e.g., 383-U1540A-6H, 7H, 9H, 11H–13H, and 16H), high MS values are associated with identified dropstones that we believe fell into the drill hole and accumulated at the top of the core during the coring process (Figure **F47**) (see **Sedimentology**). In the first 190 m of core, and possibly to 210 m CSF-A, the higher MS intervals correspond to higher dropstone presence. The presence of ice-transported coarse material might also be responsible for the higher baseline values from 80 to 140 m CCSF-A and from 145 to 210 m CCSF-A as well as the higher clay content of the sediment. Similarly, the MS minima at 143, 192, and 210 m CCSF-A are likely linked to low terrigenous content (Figure **F48**). From 170 m CCSF-A to the bottom of the site, the increase in MS is also linked to the change in lithology from mainly diatom ooze above 170 m CCSF-A to clayey nannofossil ooze below (see **Sedimentology**).

Figure F48. Mass-normalized natural gamma radiation (NGR*) and Whole-Round Multisensor Logger magnetic susceptibility (smoothed), Site U1540. cps = counts per second.
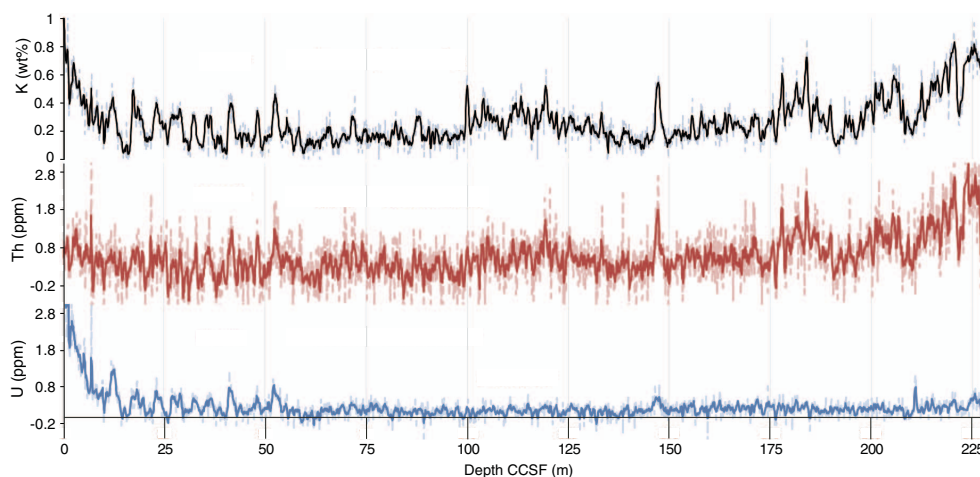
Natural gamma radiation

Mass-normalized NGR data (see **Physical properties** in the Expedition 383 methods chapter [Winckler et al., 2021a]) are presented in Figure **F48**. NGR data are normalized to mass to help reduce biases that may reflect variability in parameters such as sediment compaction, porosity, and missing sediment at some depth in or throughout all of a section liner (Walczak et al., 2015). Mass-normalized NGR data are calculated using the GRA density data. To align the GRA density data with the resolution of NGR measurements, the density record is smoothed with a Gaussian window spanning 20 cm to either side of the NGR measurement position. Normalized NGR data show downhole variations between 0 and 25 cps/g/cm^3, and variations in range and amplitude are principally similar among all holes. Holes U1540A–U1540D show a superimposed exponential downward trend of counts with increasing core depth in the upper parts (<8 m CCSF-A). The NGR and susceptibility records show similar short- and long-term variations along the record, suggesting the same origin of mainly terrigenous components (Figure **F48**).

In addition to total NGR counts, we deconvolved the record into low-resolution (semi)quantitative concentrations for the elements potassium (K), uranium (U), and thorium (Th) (Figure **F49**) following the methods of De Vleeschouwer et al. (2017), which use the whole-round NGR spectra and GRA measurements. Values in all three records decrease downcore from the surface sediments, where they are probably not in secular equilibrium. The ^{238}U concentration is inferred from the area under the spectral peak of ^{214}Bi (bismuth), a daughter product of ^{238}U. Uranium in the seawater, as well as the sediments, decays to ^{230}Th, which is easily adsorbed onto particles and scavenged to the sediments below. In younger sediments, the ^{214}Bi peak is a result of both ^{238}U decaying within the sediment and the scavenged ^{230}Th that originated from seawater U. As a result, this method overestimates the U concentration of the younger sediments. The K, Th, and U records generally correlate with high-amplitude oscillations from 10 to 55 m CCSF-A, below which depth U follows a different pattern than K and Th. The U record continues with low-amplitude oscillations of about 0.3 ppm to the bottom of the record, and K and Th correlate in a pattern similar to that of NGR/GRA and MS (Figure **F48**).
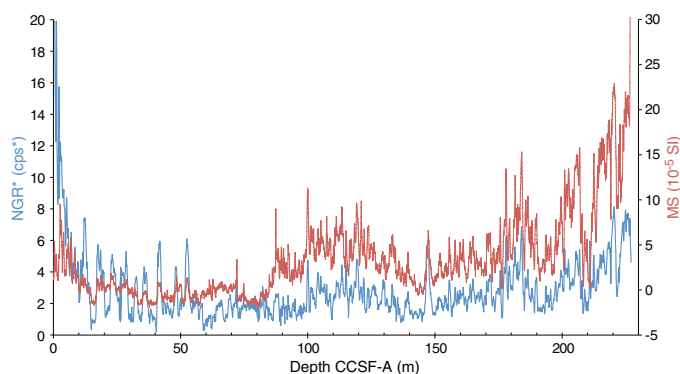
Figure F49. K (black), Th (red), and U (blue) deconvolved from NGR and GRA bulk density measurements on whole-round cores, Site U1540. Thin stippled lines = original data, thick lines = 5 point running averages.

Bulk density, grain density, and porosity

Two methods were used to evaluate bulk density at Site U1540. GRA bulk density values in Holes U1540A and U1540C vary from 1.16 to ~1.65 g/cm³ (Figure **F50**). Bulk density values calculated from discrete MAD samples are similar in absolute values to GRA measurements and display similar trends downhole in Holes U1540A, U1540B, and U1540D, leading to an excellent correlation coefficient between both methods of $r^2 = 0.953$ across all encountered lithofacies (Figure **F51**). We excluded one outlier that corresponds to an error in the MAD measurement procedure. A small long-term increase in mean bulk density of 0.05 g/cm³ is observed downcore along the record, probably linked to compaction but also correlated with the lithology change from 170 m CCSF-A to the bottom of the site. GRA bulk density values remain highly variable throughout the holes, indicating short- and long-term variability (a few meters and tens of meters, respectively). Changes in GRA bulk density at both timescales mostly correspond with identified major modifier components of the main lithofacies units (see **Sedimentology**). Short timescales are mostly related to changes in the relative proportions of calcareous versus biosiliceous oozes in the

sedimentary facies, leading to a reliable linear relationship between GRA and the carbonate content of the cores with a correlation coefficient of $r^2 = 0.513$. A good correlation with color reflectance L* and RGB blue records (extracted from images) is also observed in high-amplitude variations over 1–3 m. Some smaller amplitude peaks in GRA are linked to the presence of dropstones/ice-rafted debris (IRD), as indicated by the lithology and a comparison with mass-normalized NGR data, in which peaks are linked to the presence of IRD (Figure **F50**). Long-term GRA variations are characterized by two broad maxima in baseline density values from 85 to 172 m CCSF-A and from 172 m CCSF-A to the bottom of the record. These long-term variations are not linked to the presence of IRD, unlike long-term trends in MS and NGR (see **Sedimentology** (Figure **F50**). The relationship between MS and GRA changes in the uppermost 185 m CCSF-A due to the multicomponent composition (diatom ooze, clay, nannofossil ooze, and IRD), and anticorrelation during large GRA peaks is linked to carbonate facies and correlation for smaller peaks linked to the presence of dropstones/IRD (Figure **F52**). For the deepest part of the record, from 185 to 225 m CCSF-A, higher bulk density values are observed, accompanied by a pronounced anticorrelation between GRA and MS (Figure **F52**). The amount of siliceous material (diatom and/or radiolarian) is reduced in the lower part of the core, and the facies changes from dominantly nannofossil to clay content. This part of the core does not contain significant amounts of ice-transported components. Thus, peaks in GRA and low susceptibility correspond to higher carbonate content, and higher clay content leads to lower GRA (due to higher pore waters associated with clay [cf. MAD results]; Figure **F51**) and higher MS values (e.g., at 205 and 220 m CCSF-A). Moreover, larger changes in MS are linked to clay content changes, whereas in the upper part of the core only a low amount of terrigenous material is associated with diatom content, leading to rather low variations in MS. For this deeper part of the core (185–228 m CCSF-A), GRA and NGR records are similar to Site U1541 characteristics, indicating a much lower sedimentation rate than in the upper part. However, the clay content (see **Sedimentology**) and the NGR values are higher than at the westerly Site U1541 for similar sedimentation rates and GRA values, indicating a higher input of

Figure F50. Mass-normalized NGR (NGR/gamma ray attenuation [GRA], blue) and GRA bulk density (smoothed, green), Site U1540.
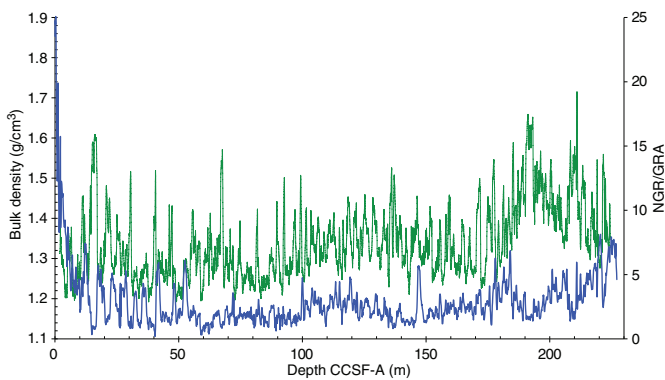

Figure F51. Comparison of whole-round gamma ray attenuation and moisture and density bulk density values, Holes U1540A, U1540B, and U1540D. Dashed lines = raw GRA measurements, solid lines = processed data. Diamonds = MAD analyses. Small square graph = correlation for MAD and GRA analyses from the same depth from different holes (no data below insert).
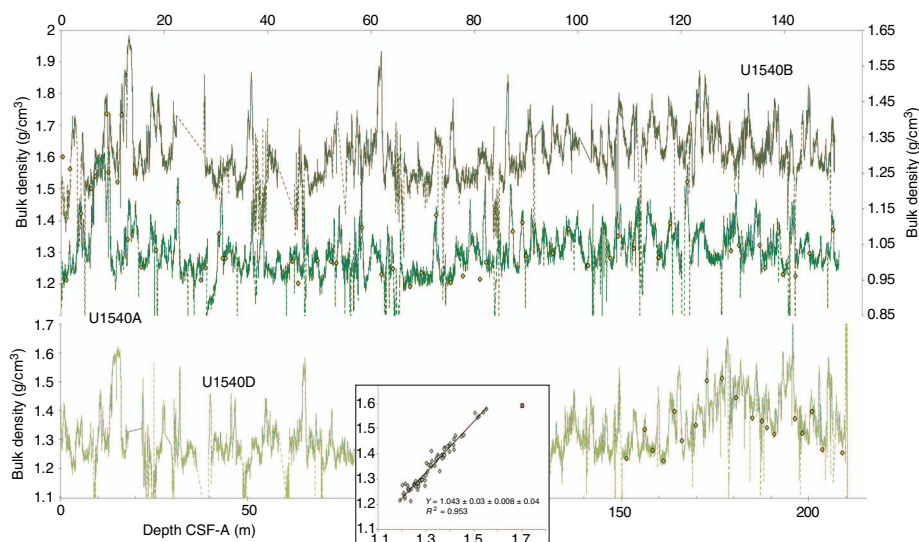
Figure F52. Whole-Round Multisensor Logger magnetic susceptibility (smoothed, red) and gamma ray attenuation bulk density (smoothed, green), Site U1540. Note different depths on panels.
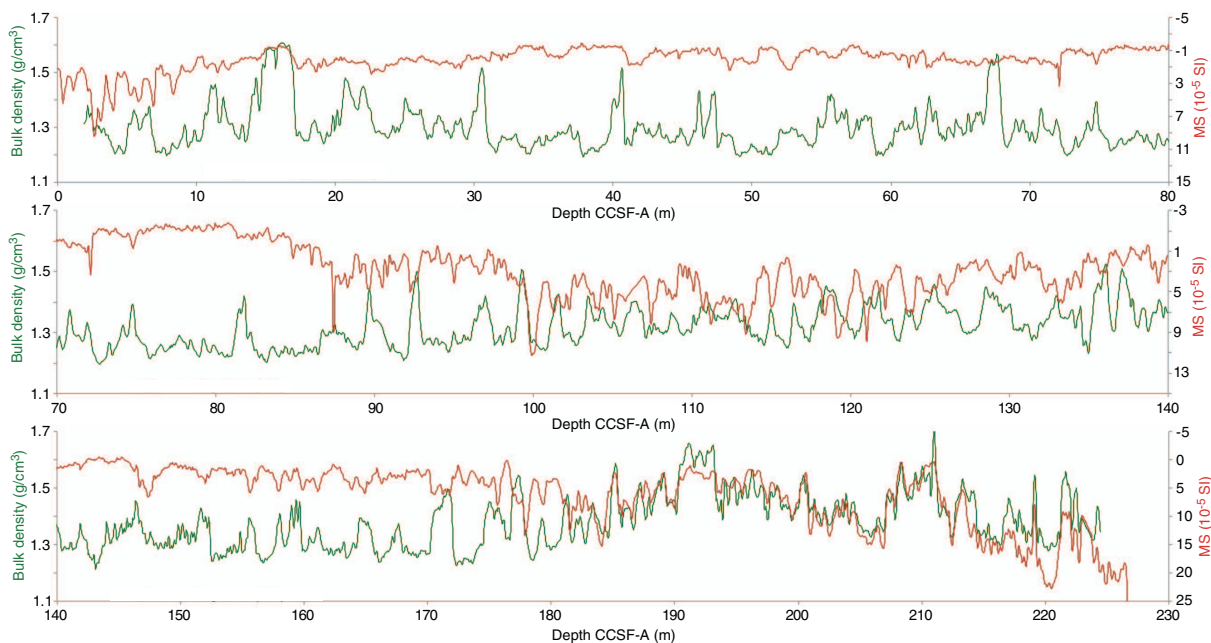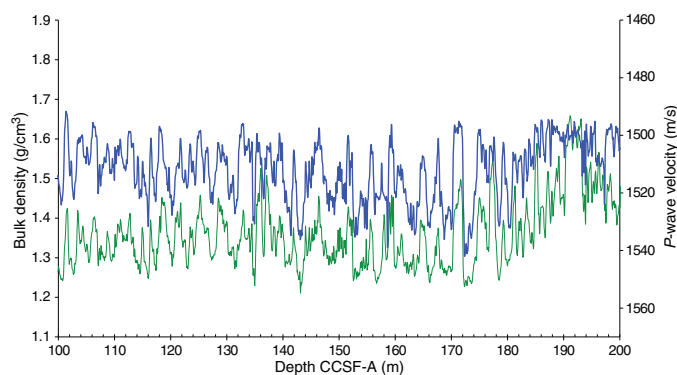

Figure F53. GRA bulk density (smoothed, green) and *P*-wave velocity (smoothed, blue), Site U1540.

terrestrial material in the eastern part of the EPR that is potentially linked to deepwater transport from AABW.

In addition to bulk density, the MAD measurements provide calculations of dry density, grain density, porosity, moisture content, void ratio, and several other properties, all of which co-vary downhole. In general, bulk density and porosity are anticorrelated. Intervals of high porosity and low grain density correspond to diatom-rich oozes. Intervals of low porosity and high density correspond to carbonate-bearing to carbonate-dominated lithologies. High clay content is linked to higher water content and lower density values than nannofossil/carbonate-dominated lithologies.

Compressional *P*-wave velocity

P-wave measurements from the WRMSL indicate moderate variations from 1490 to 1540 m/s (Figure F53). Measurements carried out using the PWC on working halves vary from 1495 to 1565 m/s and show a higher range of variation compared to the WRMSL data. However, a linear relationship is observed between these two analyses with a correlation coefficient r^2 of 0.43. Although these variations are within the range of the reproducibility, clear oscillations are ob-

served in the five holes, and cycles similar to those occurring in GRA are associated with lithology changes (Figure F53). Lower velocity values are associated with higher carbonate content, corresponding to higher GRA, indicating that those carbonates correspond mainly to smaller grain size (i.e., nannofossils). The highest maxima in *P*-wave velocity values (as high as 1540 m/s) occur in lithofacies with diatom mats. The correlation with GRA is weaker in the bottom part of the hole from 185 to 225 m CCSF-A, where low velocity and lower variability are associated with the nannofossil ooze (see **Sedimentology**). In the deepest part of the core, the velocity increases are possibly associated with the increasing clay content.

Thermal conductivity

Thermal conductivity was measured in all cores from Holes U1540A–U1540D with mostly two measurements, sometimes one, per retrieved core (Figure F54). Measurements were carried out using the needle probe on the whole-round sections; however, a number of measurements in the upper sections of Holes U1540A, U1540C, and U1540D failed due to low thermal conductivity, which was possibly due to the high water content in these sections. In the lower parts of the holes, thermal conductivity measurements were partially compromised by frequent coring disturbances, evident by cracks in the sediment and partially filled liners (see the Site U1540 VCDs in **Core descriptions**). The quality of the thermal conductivity measurements was checked by evaluating two parameters: the number of solutions acquired and the shape of the curve formed on the temperature versus time plot of these points. A valid measurement should have a sufficient number of solutions to form an exponential curve. If strictly assessed, about 30%–50% of the thermal conductivity measurements should be excluded from further evaluation. Nonetheless, measurements with a relatively low number of solutions and/or a bad repartition of these values on the temperature versus time plot (i.e., forming two curves or no curve) were kept for this reporting, subject to future quality assurance/quality control (QA/QC) exclusion.

Throughout all Site U1540 holes, thermal conductivity ranges from ~0.42 to 1.18 W/(m·K) with a mean value of 0.831 W/(m·K)

Figure F54. Thermal conductivity data from needle probe measurements, Site U1540. 0.3–0.5 W heating power over 80 s. Red line = mean values of three measurements, error bars = standard deviation, red circles = individual measurements.
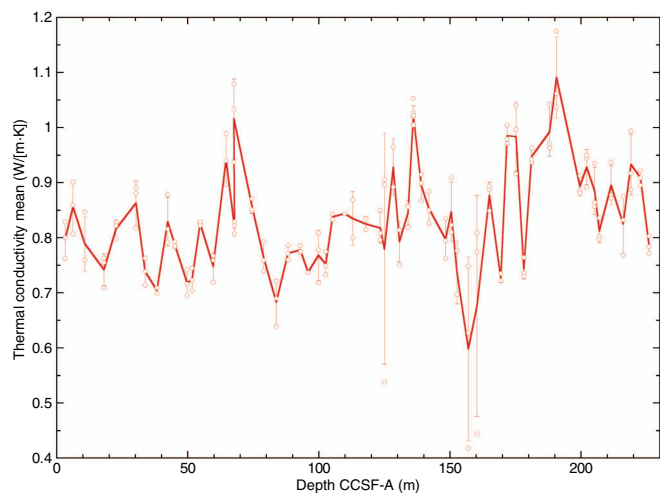
and generally corresponds to downhole changes in GRA (Figure **F53**). In general, diatom-rich oozes (Lithostratigraphic Units I and II) are characterized by very low thermal conductivity and diatom oozes with higher carbonate contents or carbonate facies (Units III and IV) are characterized by higher thermal conductivity. Generally, the thermal conductivity in Site U1540 is very low, especially when taking into account that unusually low instrumental heating values for the needle probes (0.3–0.7 W) had to be used regularly to obtain meaningful readings, possibly compromising more in-depth use of the data (e.g., for heat flow calculations).

Despite their low resolution and scatter, thermal conductivity mean values may indicate that they follow a long-time cyclic pattern with recurring peaks on a ~65–75 m scale across the Site U1540 splice occurring at approximately 64–73, 135–138, and 187–195 m CCSF (Figure **F54**). Although this pattern might correspond to orbital-scale variations in lithology at this site, such an assumption remains to be tested once a final age model is available.

Summary

Data acquired from whole-round measurements for Site U1540 are generally in good agreement with those from split-core measurements and discrete samples (Figures **F47**, **F51**). In particular, discrete MAD samples and GRA-derived density values correlate well, and GRA is also well correlated to discrete carbonate measurements from the different holes.

Major bulk density peaks, associated with the lowest P-wave velocity values, correspond to high carbonate nannofossil content, whereas smaller peaks observed simultaneously in GRA, NGR, and MS are linked to dropstone/IRD content. Low GRA density values reflect the more biosiliceous facies and correspond to higher P-wave velocity and high porosity. The older part of the site, from 185 m CCSF to the bottom, shows a clear anticorrelation of MS and GRA density values that is linked to larger amplitude variations in MS. In these oldest sediments, mainly two components are changing, carbonate nannofossils and clay; higher clay content corresponds to higher MS and lower bulk density (higher water content than the nannofossil ooze).

NGR data also imply that total counts and the derived percent potassium (K%) can be used as low-resolution proxy for the abundance of terrigenous material delivered by dust, currents, and iceberg transport. From 185 m CCSF-A to the bottom of the site, NGR values and clay

content are higher than those for Site U1541, located on the western side of the EPR, which indicates that this terrigenous material probably is transported through the AABW current branch from the Ross Sea.

Downhole changes in physical property characteristics overall are in good agreement with the defined lithostratigraphic units based on sedimentologic characteristics (Figure **F15**). Comparison of the different physical properties allows highlighting periods of two principal components changing from periods corresponding to three to four components and could help provide a more quantitative determination of the sediment composition at this site.

Downhole measurements
In situ temperature and heat flow

At Site U1540, we carried out five downhole formation temperature measurements in Hole U1540A using the APCT-3 tool, supplemented by one measurement in Hole U1540D and two in Hole U1540E to increase the depth range covered (Table **T13**). The single measurement in Hole U1540D at 210.5 m CSF-A yielded a significantly lower temperature with various TP-Fit software procedures that resembled temperatures in the upper sedimentary sequence in Holes U1540A and U1540E. The observed temperature difference is most likely due to disturbance induced by movements through uncompensated heave. The measured temperature is interpreted to be an outlier, was discarded from further interpretation, and is not shown on Figure **F55**. The two additional measurements carried out in Hole U1540E principally fell within the range of Hole U1540A values and were integrated into a spliced downhole in situ temperature record. The resulting calculated in situ formation temperatures increase with depth from 2.33°C at 37.6 mbsf (Core 383-U1540A-4H) to a maximum of 4.76°C at 184.5 mbsf (Core 383-U1540E-8H) (Figure **F55**). Some scatter is observed in the data. The average bottom water temperature across all holes was calculated as 1.197°C, and the average minimum temperature was 1.156°C (Table **T13**). Differences in average and minimum mudline bottom water temperature between the two holes were calculated to be <0.02°C, and thus have no effect on the calculation of downhole temperatures. These values were derived from recording temperatures with the APCT-3 tool stopped at the mudline for about 5 min while the pumps switched off before lowering the tool to target depth. The temperatures thus represent the average of all APCT-3 measurements for a given hole or site and should be only regarded as approximations of bottom water temperatures. Bottom water temperature values are well in line with data from previous Site U1539 and within the expected temperatures based on previous instrumental and World Ocean Atlas data (Gersonde, 2011; Locarnini et al., 2010) from locations proximal to Site U1540.

Thermal conductivity under in situ conditions was estimated from laboratory-determined thermal conductivity using established methods (Pribnow et al., 2000; Hyndman et al., 1974) (see **Physical properties** in the Expedition 383 methods chapter [Winckler et al., 2021a]). Thermal resistance was calculated by cumulatively adding the inverse of the in situ thermal conductivity values over depth intervals downhole (Figure **F55**). A heat flow of 18 mW/m² for the combined data from both holes was calculated from the slope of the linear fit between in situ temperature and thermal resistance (Pribnow et al., 2000), which is higher than the heat flow of 11 and 14 mW/m² obtained in Holes U1539A and U1539C, respectively. The geothermal gradient (dT/dz) is estimated for the site at ~18°C/km within the total measured depth interval based on a linear fit of temperature versus depth, in which T is temperature at depth z.

Table T13. Results from advanced piston corer temperature (APCT-3) tool profiles, Site U1540. **Download table in CSV format.**

Figure F55. Heat flow calculations, Holes U1540A and U1540E. The value from Hole U1540D is omitted here for comparison. A. In situ sediment temperatures from advanced piston corer temperature (APCT-3) tool measurements with average values for Cores 383-U1540A-4H, 7H, 10H, 13H, and 16H (diamonds) and 383-U1540E-5H, 18H, and 16H (circles) and linear fit. B. In situ thermal conductivity data (diamonds) with calculated thermal resistance (solid line). C. Bullard plot of heat flow calculated from a linear fit of temperature vs. thermal resistance data.
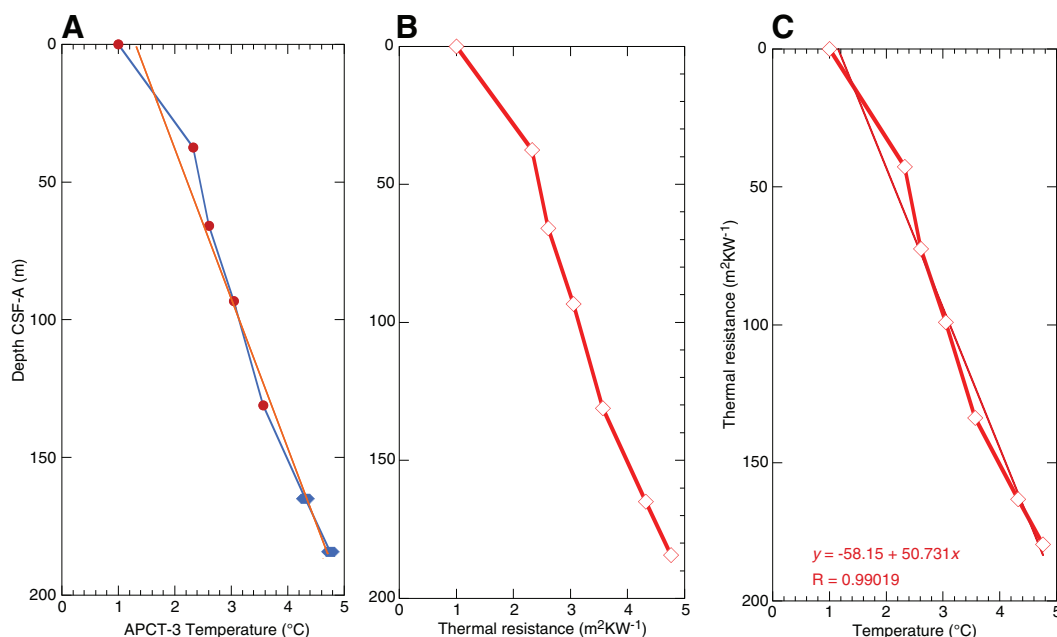
Stratigraphic correlation

Correlations between holes at Site U1540 were accomplished using Correlator software (version 3.0). Tie points were established mostly using RBG blue extracted from the images (Figure **F56**), but in many cases a combination of measurements was used (Table **T14**). We constructed a splice from 0 to 222.95 m CCSF-A using Holes U1540A, U1540B, U1540D and U1540E (Table **T15**; Figures **F56**, **F57**, **F58**). However, because of some misfired cores that were disturbed and could not be used, the splice contains two gaps. The deepest cores from Holes U1540D and U1540E (383-U1540D-22H, 383-U1540D-23X, and 383-U1540E-10H) were excluded from the spliced interval because of poor recovery and high levels of drilling disturbance. In the absence of reliable stratigraphic markers in Core 383-U1540E-10H, Core 383-U1540D-21H was appended to the bottom of the splice, as discussed below.

The CCSF-A scale is anchored to the mudline of Core 383-U1540B-1H, which is assigned the depth of 0 m CCSF-A. From this anchor, we worked downhole using Correlator to establish a composite stratigraphy on a core-by-core basis. IW sampling and shipboard measurement sampling was done on Cores 383-U1540A-1H through 16H, 383-U1540B-1H through 3H, and 383-U1540D-15H through 20H; thus, our general approach was to avoid using material from these cores. However, because of poor recovery or coring disturbance in a few intervals, we had to piece together the splice using all four holes. From 0 to 142.5 m CCSF-A, we used Hole U1540B as the backbone of the splice. We filled gaps between cores and avoided any disturbed intervals by including cores from Holes U1540A and U1540D in the splice. Then, from 142.5 m to the bottom of the splice, we used Hole U1540D as the backbone of the

splice and filled gaps between cores and avoided disturbed intervals by including cores from Hole U1540E.

The splice is continuous with no gaps from 0 to 26.22 m CCSF-A. At that depth, Core 383-U1540A-3H was appended to the splice using an increasing cumulative affine offset of 0.5 m CCSF-A per core. Below this first gap, the splice is continuous from 26.59 m CCSF-A to the bottom of Core 383-U1540D-10H at 71.98 m CCSF-A. At that depth, Core 11H was appended to the splice, again by setting the affine offset with an increasing cumulative affine offset of 0.5 m CCSF-A per core. The splice is continuous from 72.23 to 222.95 CCSF-A, which is the bottom of Core 383-U1540D-20H. At that point, Core 21H was appended to the splice using an increasing cumulative offset of 0.5 m CCSF-A per core.

The cumulative offset between the CSF-A and CCSF-A depth scales is nearly linear for all Site U1540 holes (Figure **F59**). The growth factor is typically 7%–15%, which is expected from sediments that expand due to release of overburden but have minimal gas expansion due to low concentrations of methane and other gases (see **Geochemistry**). However, the range of growth factors varies from 0% to 84%, and this can be seen in large variations in cumulative offset with depth. This results from core disturbance due to bad weather conditions and misfired APC coring in a few instances in the upper 100 m of Holes U1540A, U1540B, and U1540D. The CSF-A depth for the top of each core is set to the drilling depth below seafloor (DSF), which is based on the position of the drill string below the seafloor, but the process of correlation moved each core top depth to a position on the CCSF-A scale that may not represent variable sediment compaction and expansion. Calculation of mass accumulation rates based on the CCSF-A scale should account for differential expansion by dividing apparent depth intervals by the appropriate growth factor.

Figure F56. Red-green-blue (RGB) blue data vs. composite depth, Holes U1540A–U1540E. Data are divided into 100 m intervals. Top: RGB blue splice constructed by combining data from all holes. (Continued on next page.)
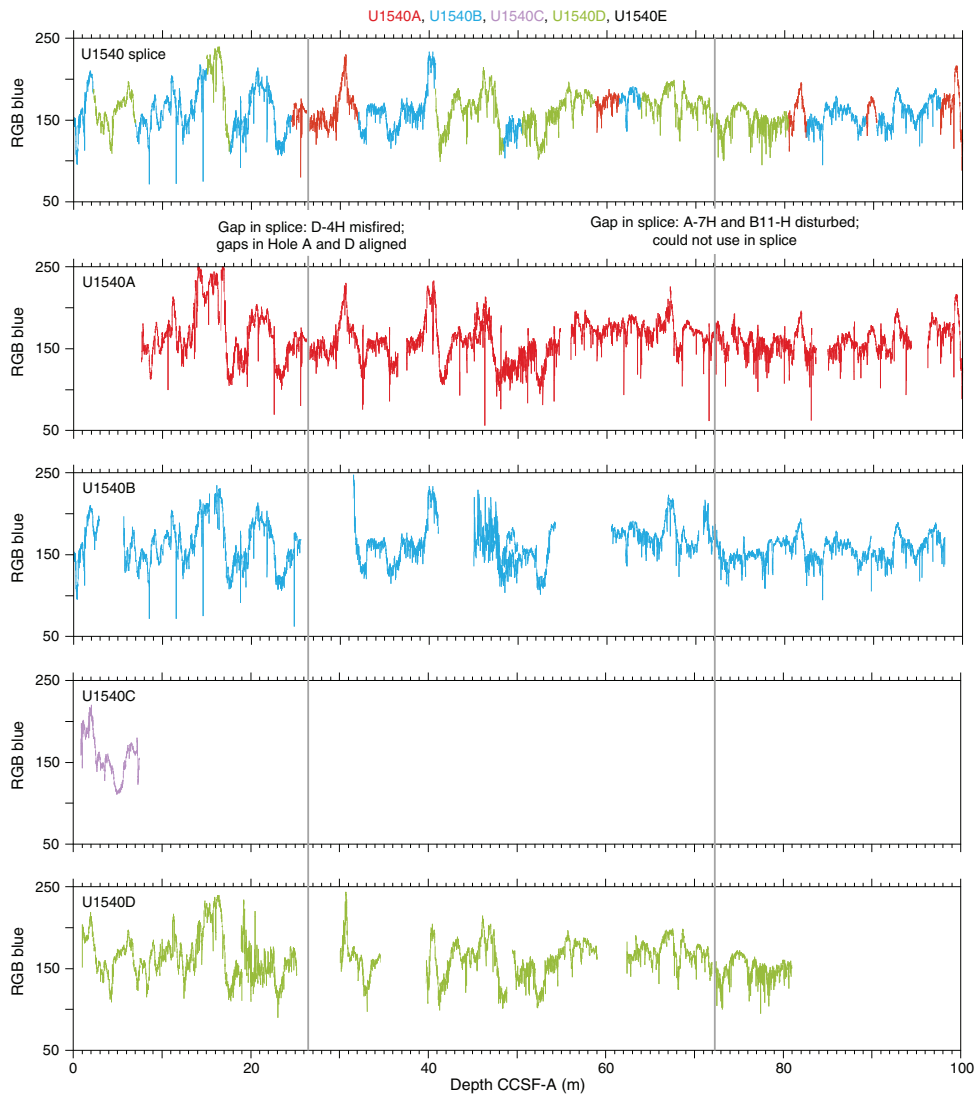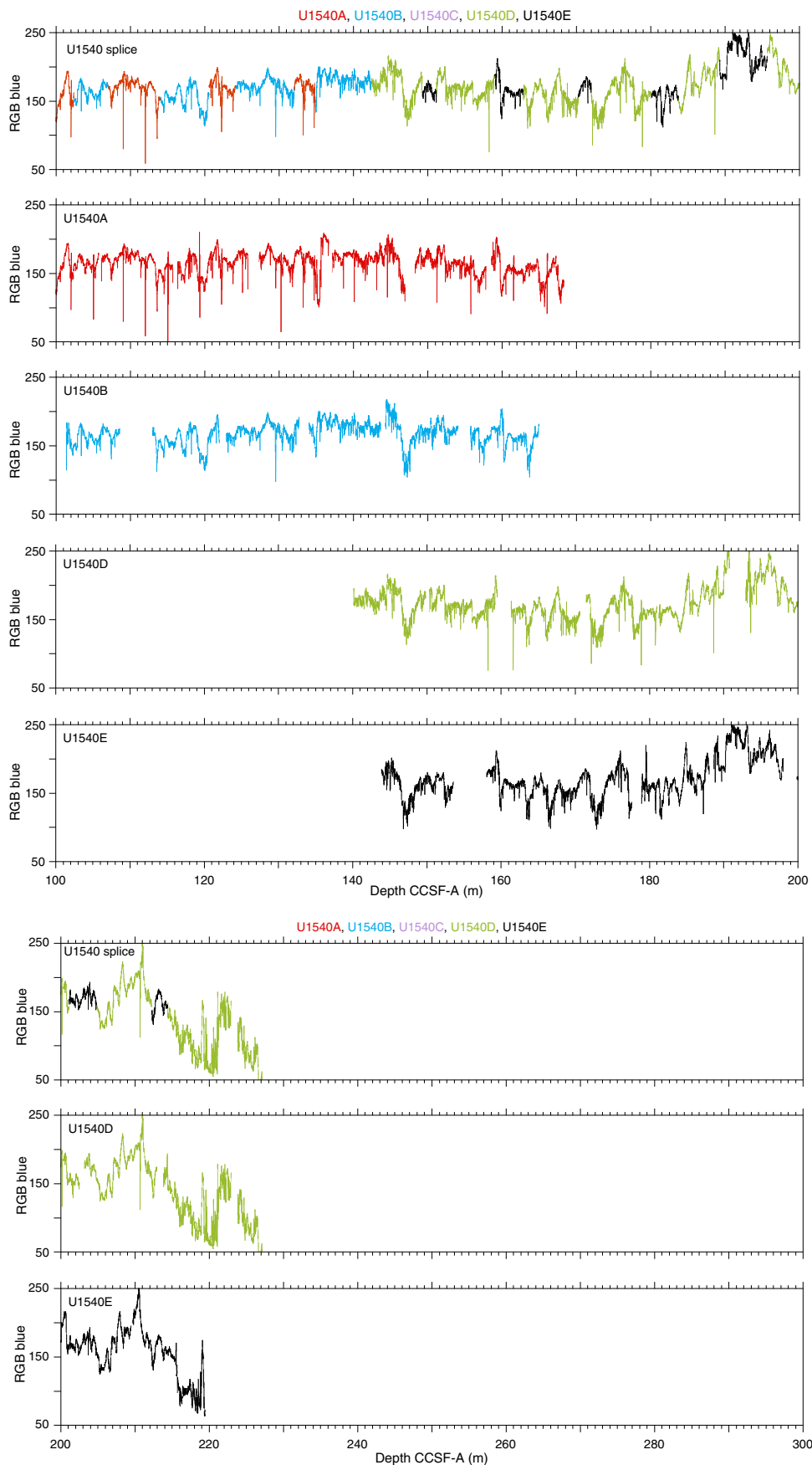
Figure F56 (continued).

Table T14. Affine table, Site U1540. RGB = red, green, blue. **Download table in CSV format.**

Core	Depth CSF-A (m)	Depth CCSF-A (m)	Offset (m)	CCSF of TIE point used to determine offset (m)	Type of shift	Data used	Reference core
383-U1540A-							
1H	0	7.657	7.657	14.993	TIED to	RGB blue	U1540B-2H
2H	9.0	16.592	7.592	24.482	TIED to	RGB blue	U1540B-3H
3H	18.5	26.592	8.092		SET to affine of Core 2H + 0.5 m		
4H	28.0	37.459	9.459	40.725	TIED to	RGB blue	U1540B-5H
5H	37.5	45.129	7.629	50.462	TIED to	RGB blue	U1540B-8H
6H	47.0	55.953	8.953	58.626	TIED to	RGB blue	U1540D-8H
7H	56.5	65.537	9.037	68.455	TIED to	RGB blue	U1540D-10H
8H	64.8	74.018	9.218	80.428	TIED to	RGB blue	U1540D-11H
9H	74.3	84.845	10.545	89.122	TIED to	RGB blue	U1540B-12H
10H	83.8	96.085	12.285	97.521	TIED to	RGB blue	U1540B-13H
11H	93.3	106.128	12.828	107.006	TIED to	RGB blue	U1540B-14H
12H	102.8	116.359	13.559	120.599	TIED to	RGB blue	U1540B-15H
13H	112.3	127.32	15.02	132.04	TIED to	RGB blue	U1540B-16H
14H	121.8	137.163	15.363	142.465	TIED to	RGB blue	U1540B-17H
15H	131.3	148.311	17.011	151.132	TIED to	RGB blue	U1540E-2H
16H	140.8	158.579	17.779	160.497	TIED to	RGB blue	U1540E-4H
383-U1540B-							
1H	0	0	0				Mudline
2H	3.1	5.608	2.508	6.997	TIED to	RGB blue	U1540D-1H
3H	12.6	15.831	3.231	17.547	TIED to	RGB blue	U1540D-2H
5H	27.6	31.44	3.84	32.039	TIED to	RGB blue	U1540A-3H
6H	37.1	45.022	7.922	48.342	TIED to	RGB blue	U1540D-7H
8H	45.1	45.986	0.886	50.462	TIED to	RGB blue	U1540D-7H
10H	55.0	60.496	5.496	61.396	TIED to	RGB blue	U1540A-6H
11H	64.5	70.802	6.302	71.763	TIED to	RGB blue	U1540D-10H
12H	74.0	79.947	5.947	82.492	TIED to	RGB blue	U1540A-8H
13H	83.5	89.75	6.25	90.363	TIED to	RGB blue	U1540A-9H
14H	93.0	101.388	8.388	102.422	TIED to	RGB blue	U1540A-10H
15H	102.5	112.995	10.495	114.052	TIED to	RGB blue	U1540A-11H
16H	112.0	122.933	10.933	124.256	TIED to	RGB blue	U1540A-12H
17H	121.5	134.028	12.528	134.901	TIED to	RGB blue	U1540A-13H
18H	131.0	144.315	13.315	151.157	TIED to	RGB blue	U1540E-2H
19H	140.5	155.74	15.24	162.806	TIED to	RGB blue	U1540E-4H
383-U1540C-							
1H	0	0.831	0.831	2.232	TIED to	RGB blue	U1540B-1H
383-U1540D-							
1H′	0	0.971	0.971	2.232	TIED to	RGB blue	U1540B-1H
2H	8.9	9.722	0.822	14.993	TIED to	RGB blue	U1540B-2H
4H	21.7	18.912	−2.788	22.30	TIED to	RGB blue	U1540B-3H
6H	29.7	28.569	−1.131	31.056	TIED to	RGB blue	U1540A-3H
7H	39.2	39.758	0.558	40.725	TIED to	RGB blue	U1540B-5H
8H	48.7	49.442	0.742	50.462	TIED to	RGB blue	U1540B-8H
10H	60.2	62.328	2.128	63.802	TIED to	RGB blue	U1540B-10H
11H	69.7	72.228	2.528		SET to affine of Core 10H + 0.5 m		
13H	131.0	140.09	9.09	142.465	TIED to	RGB blue	U1540B-17H
14H	140.5	150.318	9.818	151.157	TIED to	RGB blue	U1540E-2H
15H	150.0	161.345	11.345	162.806	TIED to	RGB blue	U1540E-4H
16H	159.5	171.445	11.945	171.981	TIED to	RGB blue	U1540E-5H
17H	169.0	181.247	12.247	183.719	TIED to	RGB blue	U1540E-6H
18H	178.5	192.938	14.438	195.668	TIED to	RGB blue	U1540E-7H
19H	188.0	203.167	15.167	204.809	TIED to	RGB blue	U1540E-8H
20H	197.5	213.80	16.30	214.40	TIED to	RGB blue	U1540E-9H
21H	207.0	223.80	16.80		SET to affine of Core 20H + 0.5 m		
22H	210.0	227.30	17.30		SET to affine of Core 21H + 0.5 m		
23X	210.5	228.30	17.80		SET to affine of Core 22X + 0.5 m		
383-U1540E-							
2H	135.0	143.85	8.85	149.274	TIED to	RGB blue	U1540D-13H
4H	146.5	158.048	11.548	159.031	TIED to	RGB blue	U1540D-14H
5H	156.0	167.845	11.845	170.244	TIED to	RGB blue	U1540D-15H
6H	165.5	178.906	13.406	180.069	TIED to	RGB blue	U1540D-16H
7H	175.0	188.633	13.633	189.256	TIED to	RGB blue	U1540D-17H
8H	184.5	199.845	15.345	201.11	TIED to	RGB blue	U1540D-18H
9H	194.0	209.672	15.672	212.259	TIED to	RGB blue	U1540D-19H
10H	203.5	219.172	16.172		SET to affine of Core 9H + 0.5 m		

Table T15. Splice interval table, Site U1540. RGB = red, green, blue. **Download table in CSV format.**

Hole	Top of splice interval				Bottom of splice interval				Splice type	Data used
	Core, section	Offset (cm)	Depth CSF-A (m)	Depth CCSF-A (m)	Core, section	Offset (cm)	Depth CSF-A (m)	Depth CCSF-A (m)		
U1540B	1H-1	0	0	0	1H-2	73.2	2.232	2.232	TIE	RGB blue
U1540D	1H-1	126.1	1.261	2.232	1H-5	0.6	6.026	6.997	TIE	RGB blue
U1540B	2H-1	138.9	4.489	6.997	2H-7	71	12.84	14.993	TIE	RGB blue
U1540D	2H-4	111.6	14.526	15.348	2H-6	30.5	16.725	17.547	TIE	RGB blue
U1540B	3H-2	20.6	14.316	17.547	3H-6	112.1	21.251	24.482	TIE	RGB blue
U1540A	2H-6	36	16.89	24.482	2H-7	60	18.63	26.222	APPEND	RGB blue
U1540A	3H-1	0	18.50	26.592	3H-4	97.7	23.947	32.039	TIE	RGB blue
U1540B	5H-1	59.9	28.199	32.039	5H-7	26.5	36.885	40.725	TIE	RGB blue
U1540D	7H-1	96.7	40.167	40.725	7H-6	105.4	47.784	48.342	TIE	RGB blue
U1540B	8H-2	85.6	47.456	48.342	8H-3	147.6	49.576	50.462	TIE	RGB blue
U1540D	8H-1	102	49.72	50.462	8H-7	17.4	57.884	58.626	TIE	RGB blue
U1540A	6H-2	117.3	49.673	58.626	6H-4	93.3	52.443	61.396	TIE	RGB blue
U1540B	10H-1	90	55.90	61.396	10H-3	30.6	58.306	63.802	TIE	RGB blue
U1540D	10H-1	147.4	61.674	63.802	10H-7	65	69.85	71.978	APPEND	RGB blue
U1540D	11H-1	0	69.70	72.228	11H-6	71	77.90	80.428	TIE	RGB blue
U1540A	8H-5	41	71.21	80.428	8H-6	97.4	73.274	82.492	TIE	RGB blue
U1540B	12H-2	104.5	76.545	82.492	12H-7	15.5	83.175	89.122	TIE	RGB blue
U1540A	9H-3	128.7	78.577	89.122	9H-4	102.8	79.818	90.363	TIE	RGB blue
U1540B	13H-1	61.3	84.113	90.363	13H-6	88.1	91.271	97.521	TIE	RGB blue
U1540A	10H-1	143.6	85.236	97.521	10H-5	32.7	90.137	102.422	TIE	RGB blue
U1540B	14H-1	103.4	94.034	102.422	14H-4	113.8	98.618	107.006	TIE	RGB blue
U1540A	11H-1	87.8	94.178	107.006	11H-6	46.4	101.224	114.052	TIE	RGB blue
U1540B	15H-1	105.7	103.557	114.052	15H-6	14.4	110.104	120.599	TIE	RGB blue
U1540A	12H-3	125	107.04	120.599	12H-6	42.7	110.697	124.256	TIE	RGB blue
U1540B	16H-1	132.3	113.323	124.256	16H-7	11.7	121.107	132.04	TIE	RGB blue
U1540A	13H-4	22	117.02	132.04	13H-6	10.1	119.881	134.901	TIE	RGB blue
U1540B	17H-1	87.3	122.373	134.901	17H-6	100.7	129.937	142.465	TIE	RGB blue
U1540D	13H-2	88.5	133.375	142.465	13H-7	22.4	140.184	149.274	TIE	RGB blue
U1540E	2H-4	98.4	140.424	149.274	2H-5	136.7	142.307	151.157	TIE	RGB blue
U1540D	14H-1	83.9	141.339	151.157	14H-7	13.3	149.213	159.031	TIE	RGB blue
U1540E	4H-1	98.3	147.483	159.031	4H-4	26.8	151.258	162.806	TIE	RGB blue
U1540D	15H-1	146.1	151.461	162.806	15H-7	20.9	158.899	170.244	TIE	RGB blue
U1540E	5H-2	89.9	158.399	170.244	5H-3	114.6	160.136	171.981	TIE	RGB blue
U1540D	16H-1	53.6	160.036	171.981	16H-6	114.4	168.124	180.069	TIE	RGB blue
U1540E	6H-1	116.3	166.663	180.069	6H-4	33.3	170.313	183.719	TIE	RGB blue
U1540D	17H-2	96.2	171.472	183.719	17H-6	56.9	177.009	189.256	TIE	RGB blue
U1540E	7H-1	62.3	175.623	189.256	7H-5	101.5	182.035	195.668	TIE	RGB blue
U1540D	18H-2	127	181.23	195.668	18H-6	86.2	186.672	201.11	TIE	RGB blue
U1540E	8H-1	126.5	185.765	201.11	8H-4	45.4	189.464	204.809	TIE	RGB blue
U1540D	19H-2	13.2	189.642	204.809	19H-6	151.2	197.092	212.259	TIE	RGB blue
U1540E	9H-2	108.7	196.587	212.259	9H-4	20.8	198.738	214.41	TIE	RGB blue
U1540D	20H-1	61	198.11	214.41	20H-7	62	206.65	222.95	APPEND	RGB blue
U1540D	21H-1	0	207.00	223.80	21H-3	40	210.33	227.13	APPEND	RGB blue

Figure F57. Spliced composite records of red-green-blue (RGB) blue, cleaned Whole-Round Multisensor Logger gamma ray attenuation (GRA) and magnetic susceptibility (MS), and natural gamma radiation (NGR), Site U1540. Data are divided into 50 m intervals. cps = counts per second. (Continued on next two pages.)
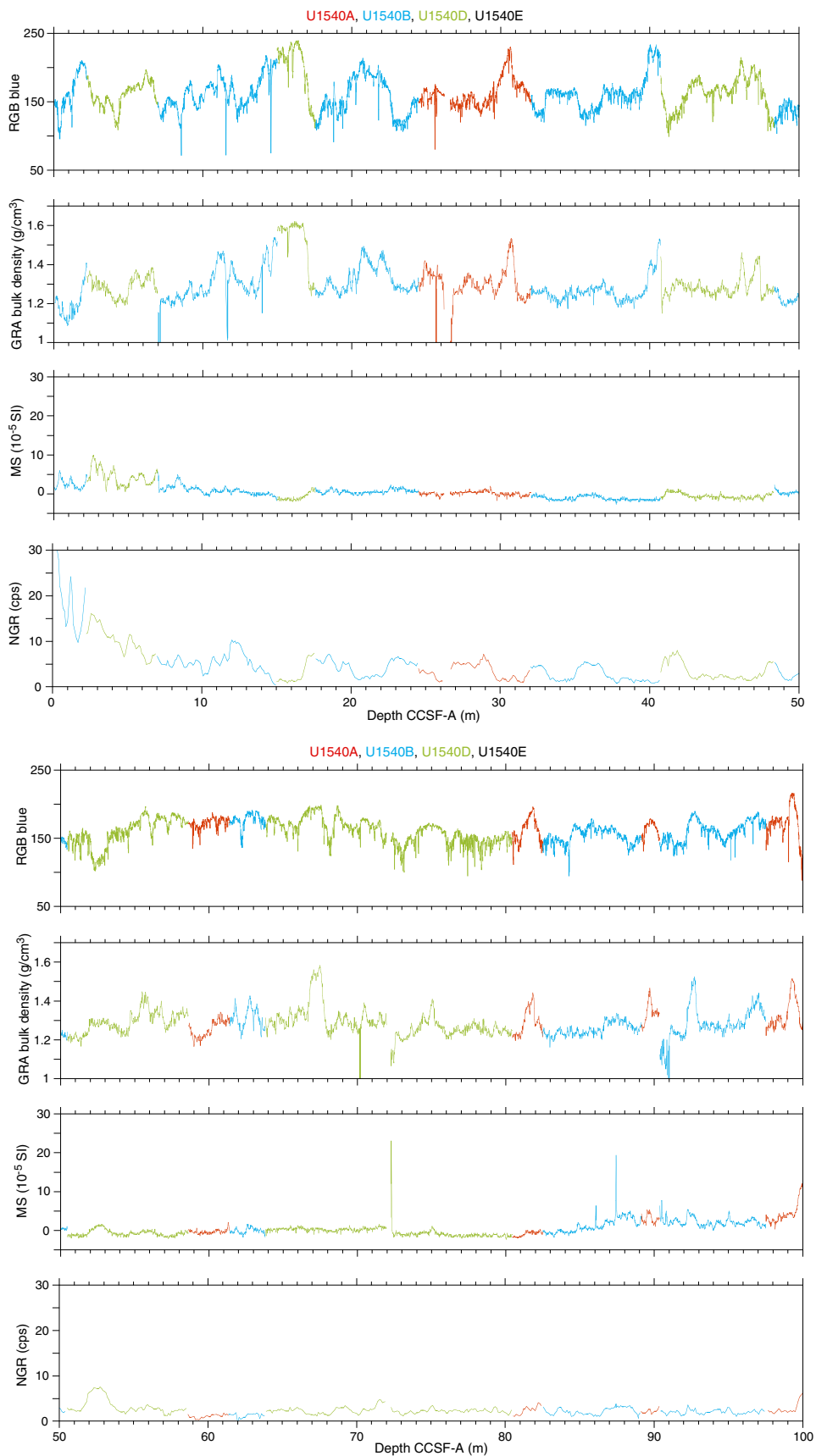
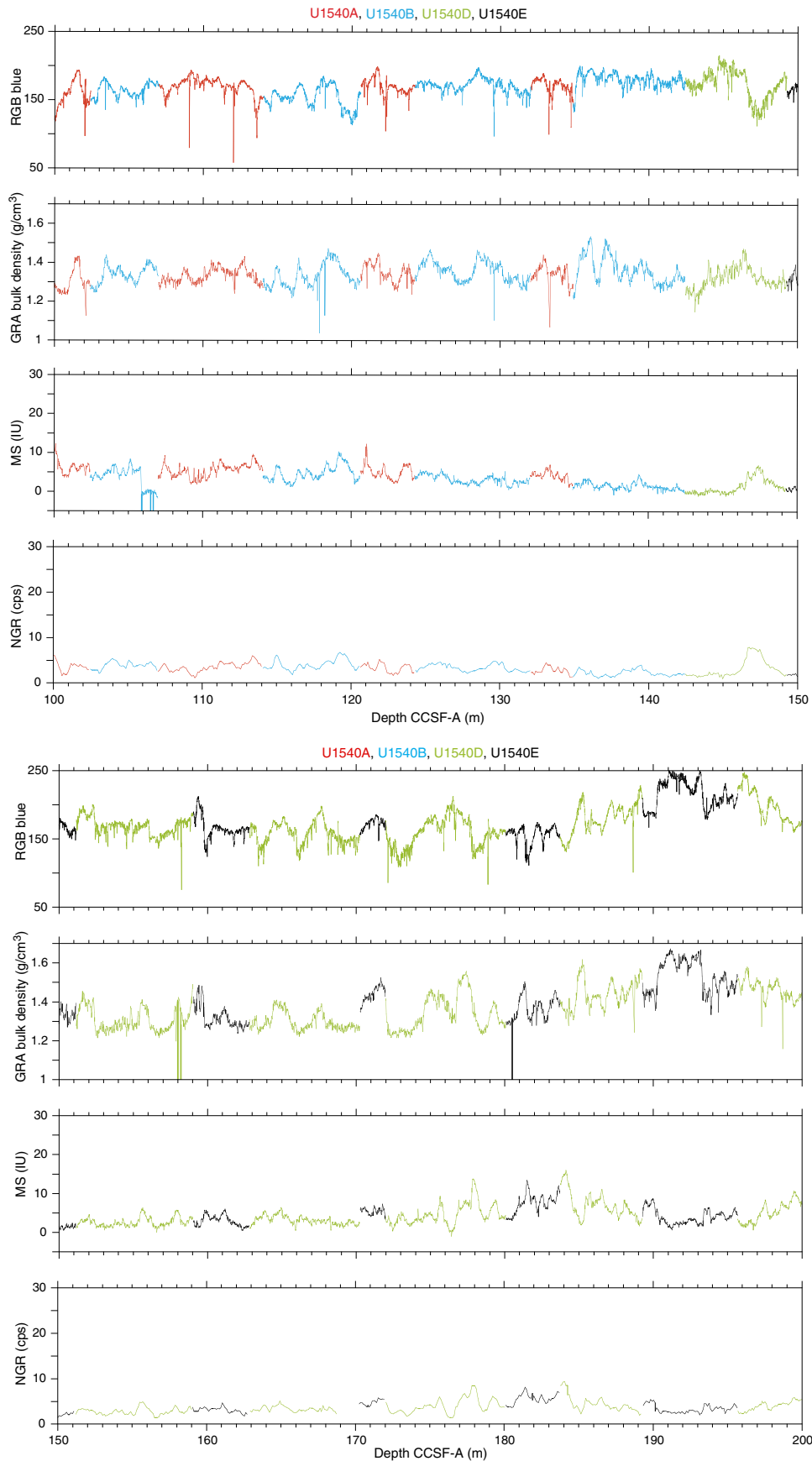Figure F57 (continued). (Continued on next page.)
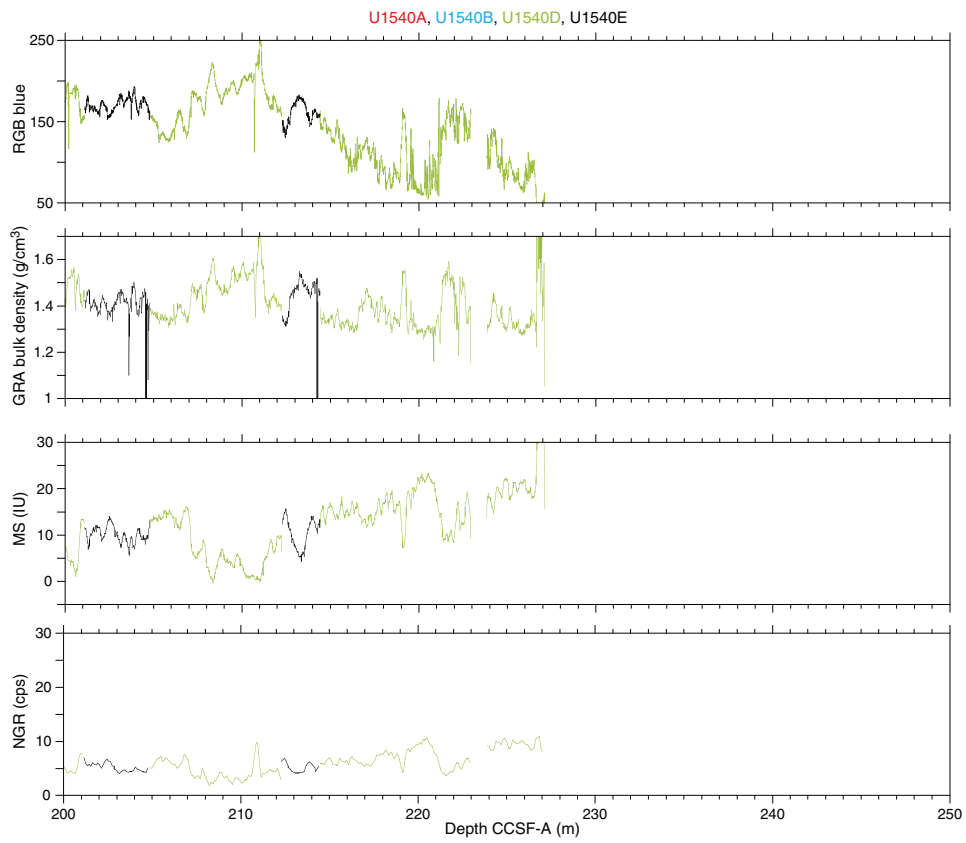
Figure F57 (continued).

Figure F58. Complete spliced composite records of cleaned red-green-blue (RGB) blue, Whole-Round Multisensor Logger gamma ray attenuation (GRA) and magnetic susceptibility (MS), and natural gamma radiation (NGR), Site U1540. cps = counts per second.
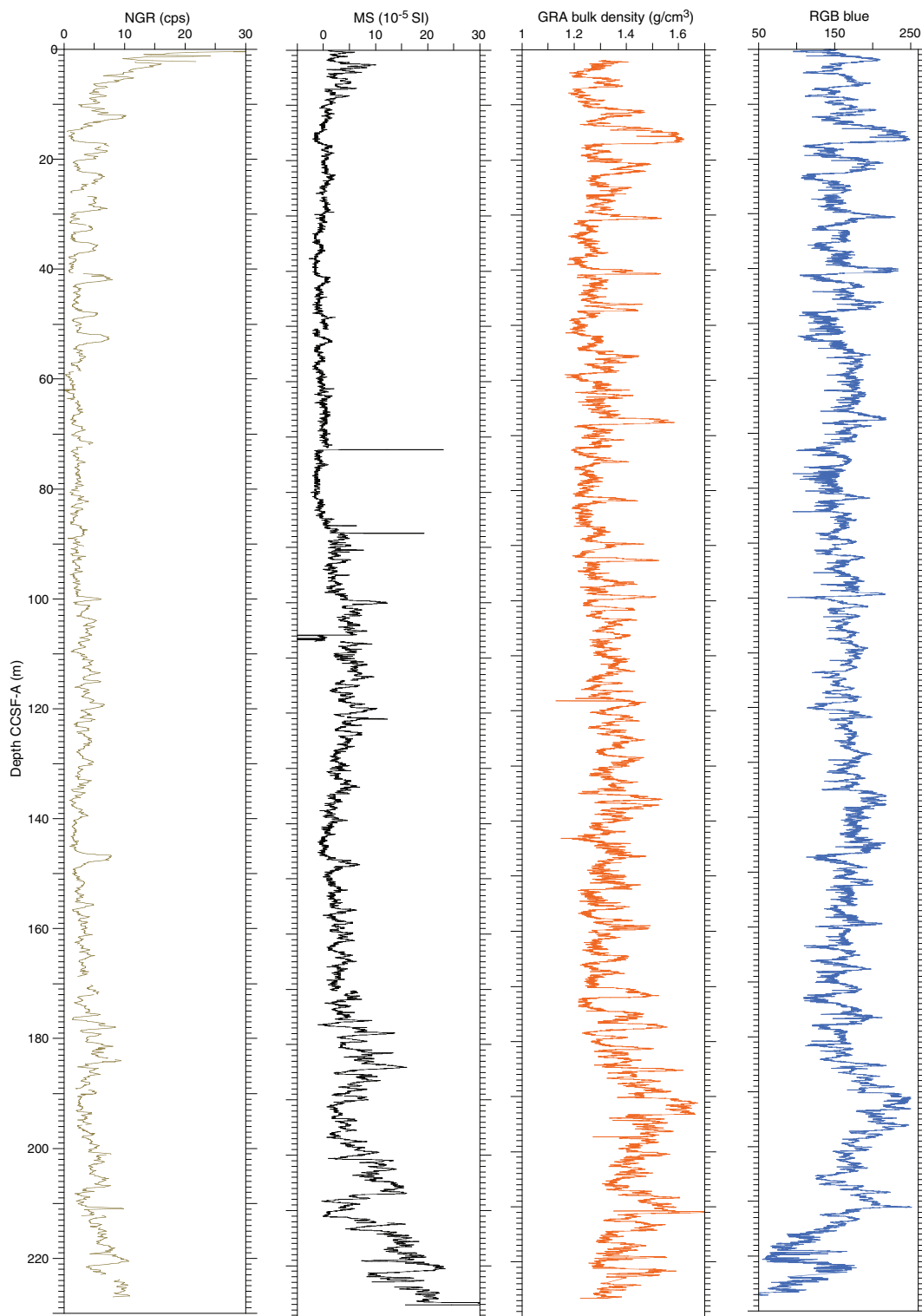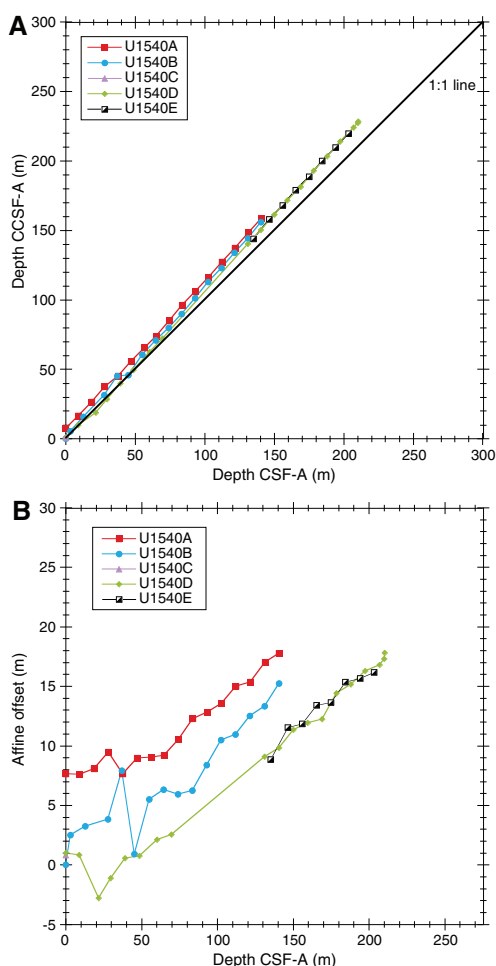
Figure F59. A. Comparison of core and composite depth scales in the Site U1540 splice. B. Comparison of the growth of cumulative depth offset and core depth.

References

Alvarez Zarikian, C.A., 2015. Cenozoic bathyal and abyssal ostracods beneath the South Pacific Gyre (IODP Expedition 329 Sites U1367, U1368 and U1370). *Palaeogeography, Palaeoclimatology, Palaeoecology,* 419:115–142. **https://doi.org/10.1016/j.palaeo.2014.07.024**

Bach, W., and Edwards, K.J., 2003. Iron and sulfide oxidation within the basaltic ocean crust: implications for chemolithoautotrophic microbial biomass production. *Geochimica et Cosmochimica Acta,* 67(20):3871–3887. **https://doi.org/10.1016/S0016-7037(03)00304-1**

Bremer, M.L., and Lohmann, G.P., 1982. Evidence for primary control of the distribution of certain Atlantic Ocean benthic foraminifera by degree of carbonate saturation. *Deep-Sea Research, Part A. Oceanographic Research Papers*, 29(8):987–998. **https://doi.org/10.1016/0198-0149(82)90022-X**

Burdige, D.J., 1993. The biogeochemistry of manganese and iron reduction in marine sediments. *Earth-Science Reviews,* 35(3):249–284. **https://doi.org/10.1016/0012-8252(93)90040-E**

Bylinskaya, M.E., 2004. Range and stratigraphic significance of the *Globorotalia crassaformis plexus. Journal of Iberian Geology*, 31(1):51–63.

Ciesielski, P.F., 1975. Biostratigraphy and paleoecology of Neogene and Oligocene silicoflagellates from cores recovered during Antarctic Leg 28, Deep Sea Drilling Project. *In* Hayes, D.E., Frakes, L.A., et al., *Initial Reports of the Deep Sea Drilling Project,* 28: Washington, DC (U.S. Government Printing Office), 625–691. **https://doi.org/10.2973/dsdp.proc.28.117.1975**

Ciesielski, P.F., 1983. The Neogene and Quaternary diatom biostratigraphy of subantarctic sediments, Deep Sea Drilling Project Leg 71. *In* Ludwig, W.J., Krasheninnikov, V.A., et al., *Initial Reports of the Deep Sea Drilling Project,* 71 (Part 2): Washington (U.S. Government Printing Office), 635–666. **https://doi.org/10.2973/dsdp.proc.71.125.1983**

Das, M., Singh, R.K., Vats, N., Holbourn, A., Mishra, S., Farooq, S.H., and Pandey, D.K., 2018. Changes in the distribution of Uvigernidae species over the past 775 kyr: implications for the paleoceanographic evolution of the Japan Sea. *Palaeogeography, Palaeoclimatology, Palaeoecology*, 507:201–213. **https://doi.org/10.1016/j.palaeo.2018.07.019**

De Vleeschouwer, D., Dunlea, A.G., Auer, G., Anderson, C.H., Brumsack, H., de Loach, A., Gurnis, M., et al., 2017. Quantifying K, U, and Th contents of marine sediments using shipboard natural gamma radiation spectra measured on DV *JOIDES Resolution. Geochemistry, Geophysics, Geosystems,* 18(3):1053–1064. **https://doi.org/10.1002/2016GC006715**

Eagles, G., 2006. Deviations from an ideal thermal subsidence surface in the southern Pacific Ocean. *Terra Antartica Reports,* 12:109–118.

Esper, O., and Gersonde, R., 2014. Quaternary surface water temperature estimations: new diatom transfer functions for the Southern Ocean. *Palaeogeography, Palaeoclimatology, Palaeoecology,* 414:1–19. **https://doi.org/10.1016/j.palaeo.2014.08.008**

Expedition 324 Scientists, 2010. Site U1348. *In* Sager, W.W., Sano, T., Geldmacher, J., and the Expedition 324 Scientists, *Proceedings of the Integrated Ocean Drilling Program,* 324: Tokyo (Integrated Ocean Drilling Program Management International, Inc.). **https://doi.org/10.2204/iodp.proc.324.105.2010**

Fagel, N., 2007. Clay minerals, deep circulation and climate. *In* Hillaire-Marcel, C., and De Vernal, A. (Eds.), *Developments in Marine Geology* (Volume 1): *Proxies in Late Cenozoic Paleoceanography:* Amsterdam (Elsevier), 139–184. **https://doi.org/10.1016/S1572-5480(07)01009-3**

German, C.R., and Von Damm, K.L., 2003. Hydrothermal processes. *Treatise on Geochemistry*, 6:181–222. **https://doi.org/10.1016/B0-08-043751-6/06109-0**

Gersonde, R., 2011. The Expedition of the Research Vessel "*Polarstern*" to the Polar South Pacific Sea in 2009/2010 (ANT-XXVI/2 - BIPOMAC). *Berichte zur Polar und Meeresforschung,* 632. **http://epic.awi.de/29941/**

Gersonde, R., and Bárcena, M.A., 1998. Revision of the upper Pliocene: Pleistocene diatom biostratigraphy for the northern belt of the Southern Ocean. *Micropaleontology,* 44(1):84–98. **https://doi.org/10.2307/1486086**

Gradstein, F.M., Ogg, J.G., Schmitz, M.D., and Ogg, G.M. (Eds.), 2012. *The Geological Time Scale 2012:* Amsterdam (Elsevier). **https://doi.org/10.1016/C2011-1-08249-8**

Gupta, A.K., Singh, R.K., Joseph, S., and Thomas, E., 2004. Indian Ocean high-productivity event (10–8 Ma): linked to global cooling or to the initiation of the Indian monsoons? *Geology,* 32(9):753–756. **https://doi.org/10.1130/G20662.1**

Hilgen, F.J., Lourens, L.J., and Van Dam, J.A., 2012. The Neogene period. With contributions by A.G. Beu, A.F. Boyes, R.A. Cooper, W. Krijgsman, J.G. Ogg, W.E. Piller, and D.S. Wilson. *In* Gradstein, F.M., Ogg, J.G., Schmitz, M.D., and Ogg, G.M. (Eds.), *The Geologic Time Scale:* Oxford, United Kingdom (Elsevier), 923–978. **https://doi.org/10.1016/B978-0-444-59425-9.00029-9**

Hornibrook, N.d.B., 1981. *Globorotalia* (planktic Foraminiferida) in the late Pliocene and early Pleistocene of New Zealand. *New Zealand Journal of Geology and Geophysics,* 24(2):263–292. **https://doi.org/10.1080/00288306.1981.10422717**

Hornibrook, N.d.B., and Jenkins, D.G., 1994. DSDP 594, Chatham Rise, New Zealand—late Neogene planktonic foraminiferal biostratigraphy revisited. *Journal of Micropalaeontology,* 13(2):93–101. **https://doi.org/10.1144/jm.13.2.93**

Hu, B., Shen, L., Xu, X., and Zheng, P., 2011. Anaerobic ammonium oxidation (anammox) in different natural ecosystems. *Biochemical Society Transactions*, 39(6):1811–1816. **https://doi.org/10.1042/BST20110711**

Hyndman, R.D., Erickson, A.J., and Von Herzen, R.P., 1974. Geothermal measurements on DSDP Leg 26. *In* Davies, T.A., Luyendyk, B.P., et al., *Initial Reports of the Deep Sea Drilling Project,* 26: Washington, DC (U.S. Govt.

Printing Office), 451–463.
https://doi.org/10.2973/dsdp.proc.26.113.1974

Jenkins, D.G., 1993. Cenozoic southern mid- and high-latitude biostratigraphy and chronostratigraphy based on planktonic foraminifera. *In* Kennett, J.P., and Warnke, D.A. (Eds.), *The Antarctic Paleoenvironment: A Perspective on Global Change: Part Two.* Antarctic Research Series, 60:125–144. https://agupubs.onlinelibrary.wiley.com/doi/abs/10.1002/9781118668061.ch7

Jonkers, L., De Nooijer, L.J., Reichart, G.-J., Zahn, R., and Brummer, G.-J.A., 2012. Encrustation and trace element composition of *Neogloboquadrina dutertrei* assessed from single chamber analyses - implications for paleotemperature estimates. *Biogeosciences*, 9(11):4851–4860. https://doi.org/10.5194/bg-9-4851-2012

Lamy, F., Winckler, G., Alvarez Zarikian, C.A., and the Expedition 383 Scientists, 2021. Supplementary material, https://doi.org/10.14379/iodp.proc.383supp.2021. *Supplement to* Lamy, F., Winckler, G., Alvarez Zarikian, C.A., and the Expedition 383 Scientists, *Dynamics of the Pacific Antarctic Circumpolar Current.* Proceedings of the International Ocean Discovery Program, 383: College Station, TX (International Ocean Discovery Program). https://doi.org/10.14379/iodp.proc.383.2021

Locarnini, R.A., Mishonov, A.V., Antonov, J.I., Boyer, T.P., Garcia, H.E., Baranova, O.K., Zweng, M.M., and Johnson, D.R., 2010. World Ocean Atlas 2009 (Volume 1): Temperature. *In* Levitus, S. (Ed.), *NOAA Atlas NESDIS 68:* Washington, DC (U.S. Government Printing Office). ftp://ftp.nodc.noaa.gov/pub/WOA09/DOC/woa09_vol1_text_figures.pdf

Meyers, P.A., 1994. Preservation of elemental and isotopic source identification of sedimentary organic matter. *Chemical Geology,* 114(3–4):289–302. https://doi.org/10.1016/0009-2541(94)90059-0

Meyers, P.A., 1997. Organic geochemical proxies of paleoceanographic, paleolimnologic, and paleoclimatic processes. *Organic Geochemistry,* 27(5–6):213–250. https://doi.org/10.1016/S0146-6380(97)00049-1

Pitman, W.C., and Heirtzler, J.R., 1966. Magnetic anomalies over the Pacific-Antarctic Ridge. *Science,* 154(3753):1164–1171. https://doi.org/10.1126/science.154.3753.1164

Pribnow, D., Kinoshita, M., and Stein, C., 2000. *Thermal Data Collection and Heat Flow Recalculations for Ocean Drilling Program Legs 101–180:* Hanover, Germany (Institute for Joint Geoscientific Research, Institut für Geowissenschaftliche Gemeinschaftsaufgaben [GGA]). http://www-odp.tamu.edu/publications/heatflow/ODPReprt.pdf

Robinson, R.S., Kienast, M., Albuquerque, A.L.S., Altabet, M., Contreras, S., De Pol-Holz, R., Dubois, N., et al., 2012. A review of nitrogen isotopic alteration in marine sediments. *Paleoceanography and Paleoclimatology*, 27(4):PA4203. https://doi.org/10.1029/2012PA002321

Schönfeld, J., 2006. Taxonomy and distribution of the *Uvigerina peregrina plexus* in the tropical to northeastern Atlantic. *Journal of Foraminiferal Research*, 36(4):355–367. https://doi.org/10.2113/gsjfr.36.4.355

Scott, G.H., Kennett, J.P., Wilson, K.J., and Hayward, B.W., 2007. *Globorotalia puncticulata*: population divergence, dispersal and extinction related to Pliocene–Quaternary water masses. *Marine Micropaleontology*, 62(4):235–253. https://doi.org/10.1016/j.marmicro.2006.08.007

Singh, R.K. and Gupta, A.K., 2004. Late Oligocene–Miocene paleoceanographic evolution of the southeastern Indian Ocean: evidence from deep-sea benthic foraminifera (ODP Site 757). *Marine Micropaleontology*, 51(1–2):153–170. https://doi.org/10.1016/j.marmicro.2003.10.003

Singh, R.K., and Gupta, A.K., 2010. Deep-sea benthic foraminiferal changes in the eastern Indian Ocean (ODP Hole 757B): their links to deep Indonesian (Pacific) flow and high latitude glaciation during the Neogene. *Episodes*, 33(2):74–82.

Singh, R.K., Gupta, A.K., and Das M., 2012. Paleoceanographic significance of deep-sea benthic foraminiferal species diversity at southeastern Indian Ocean Hole 752A during the Neogene. *Palaeogeography, Palaeoclimatology, Palaeoecology*, 361–362:94–103. https://doi.org/10.1016/j.palaeo.2012.08.008

Steinhardt, J., de Nooijer, L.L., Brummer, G.-J., and Reichart, G.-J., 2015. Profiling planktonic foraminiferal crust formation. *Geochemistry, Geophysics, Geosystems*, 16(7):2409–2430. https://doi.org/10.1002/2015GC005752

Stepanova, A., and Lyle, M., 2014. Deep-sea ostracoda from the eastern equatorial Pacific (ODP Site 1238) over the last 460 ka. *Marine Micropaleontology*, 111:100–107. https://doi.org/10.1016/j.marmicro.2014.06.003

Takahashi, K., and Anderson, O.R., 2002. Class Phaeodaria. *In* Lee, J.J., Leedale, G.F, and Bradbury, P., (Eds.), *Illustrated Guide to the Protozoa* (2nd edition): Hoboken, NJ (Wiley-Blackwell), 981–994.

Tsutsui, H., Takahashi, K., Nishida, N., and Nishiwaki, S., 2009. Intraspecific morphological variation with biometry of *Distephanus speculum* (Silicoflagellata). *Marine Micropaleontology*, 72(3–4):239–250. https://doi.org/10.1016/j.marmicro.2009.06.003

Verma, S., Gupta, A.K., and Singh, R.K., 2013. Variations in deep-sea benthic foraminifera at ODP Hole 756B, southeastern Indian Ocean: evidence for changes in deep ocean circulation. *Palaeogeography, Palaeoclimatology, Palaeoecology*, 376:172–183. https://doi.org/10.1016/j.palaeo.2013.02.034

Walczak, M.H., Mix, A.C., Willse, T., Slagle, A., Stoner, J.S., Jaeger, J., Gulick, S., LeVay, L., Kioka, A., and the IODP Expedition 341 Scientific Party, 2015. Correction of non-intrusive drill core physical properties data for variability in recovered sediment volume. *Geophysical Journal International*, 202(2):1317–1323. https://doi.org/10.1093/gji/ggv204

Wei, K.-Y., 1994. Stratophenetic tracing of phylogeny using SIMCA pattern recognition technique: a case study of the late Neogene planktonic foraminifera *Globoconella* clade. *Paleobiology*, 20(1):52–65. https://doi.org/10.1017/S0094837300011131

Wetzel, A., and Uchman, A., 2012. Hemipelagic and pelagic basin plains. *In* Knaust, D., and Bromley, R.G. (Eds.), *Developments in Sedimentology* (Volume 64): *Trace Fossils as Indicators of Sedimentary Environments:* Amsterdam (Elsevier), 673–701. https://doi.org/10.1016/B978-0-444-53813-0.00022-8

Whatley, R.C., Downing, S.E., Kesler, K., and Harlow, C.J., 1986. The ostracod genus *Poseidonamicus* from the Cainozoic of D.S.D.P. sites in the S.W. Pacific. *Revista Española de Micropaleontología*, 18:387–400.

Winckler, G., Lamy, F., Alvarez Zarikian, C.A., Arz, H.W., Basak, C., Brombacher, A., Esper, O.M., Farmer, J.R., Gottschalk, J., Herbert, L.C., Iwasaki, S., Lawson, V.J., Lembke-Jene, L., Lo, L., Malinverno, E., Michel, E., Middleton, J.L., Moretti, S., Moy, C.M., Ravelo, A.C., Riesselman, C.R., Saavedra-Pellitero, M., Seo, I., Singh, R.K., Smith, R.A., Souza, A.L., Stoner, J.S., Venancio, I.M., Wan, S., Zhao, X., and Foucher McColl, N., 2021a. Expedition 383 methods. *In* Lamy, F., Winckler, G., Alvarez Zarikian, C.A., and the Expedition 383 Scientists, *Dynamics of the Pacific Antarctic Circumpolar Current.* Proceedings of the International Ocean Discovery Program, 383: College Station, TX (International Ocean Discovery Program). https://doi.org/10.14379/iodp.proc.383.102.2021

Winckler, G., Lamy, F., Alvarez Zarikian, C.A., Arz, H.W., Basak, C., Brombacher, A., Esper, O.M., Farmer, J.R., Gottschalk, J., Herbert, L.C., Iwasaki, S., Lawson, V.J., Lembke-Jene, L., Lo, L., Malinverno, E., Michel, E., Middleton, J.L., Moretti, S., Moy, C.M., Ravelo, A.C., Riesselman, C.R., Saavedra-Pellitero, M., Seo, I., Singh, R.K., Smith, R.A., Souza, A.L., Stoner, J.S., Venancio, I.M., Wan, S., Zhao, X., and Foucher McColl, N., 2021b. Expedition 383 summary. *In* Lamy, F., Winckler, G., Alvarez Zarikian, C.A., and the Expedition 383 Scientists, *Dynamics of the Pacific Antarctic Circumpolar Current.* Proceedings of the International Ocean Discovery Program, 383: College Station, TX (International Ocean Discovery Program). https://doi.org/10.14379/iodp.proc.383.101.2021

Yasuhara, M., Hunt, G., Okahashi, H., and Brandão, S.N., 2013. The 'Oxycythereis' problem: taxonomy and paleobiogeography of deep-sea ostracod genera *Pennyella* and *Rugocythereis*. *Palaeontology*, 56(5):1045–1080. https://doi.org/10.1111/pala.12035

Zielinski, U., and Gersonde, R., 2002. Plio–Pleistocene diatom biostratigraphy from ODP Leg 177, Atlantic sector of the Southern Ocean. *Marine Micropaleontology*, 45(3–4):225–268. https://doi.org/10.1016/S0377-8398(02)00031-2